The Pennsylvania State University

The Graduate School

Department of Physics

PROGRESS TOWARD A MEASUREMENT OF THE ELECTRON ELECTRICAL DIPOLE MOMENT USING ULTRA-COLD ATOMS

A Thesis in

Physics

by

Fang Fang

Submitted in Partial Fulfillment
of the Requirements
for the Degree of

Doctor of Philosophy

December 2007

The thesis of Fang Fang was reviewed and approved* by the following:

Professor David S. Weiss
Professor of Physics
Thesis Advisor
Chair of Committee

Professor Kurt Gibble
Associate Professor of Physics

Professor A.W. Castleman, Jr.
Evan Pugh Professor, Eberly distinguished chair in science

Professor Karl T. Mueller
Professor of Chemistry

Professor Jayanth R. Banavar
Distinguished Professor of Physics
Head of the Department of Physics

*Signatures are on file in the Graduate School

ABSTRACT

In this thesis, the basic principles of the C, P, T symmetries are introduced and the experiments to measure the electric dipole moment (EDM) are summarized. We propose an experiment to search for the electric dipole moment of the electron using Cs and Rb atoms in 1D optical lattice traps. Our projected sensitivity is 3×10^{-30} e-cm with an integration time of 12 hours, which is a 500-fold improvement over the current limit. The potential sources of noise and systematic errors in our designed experiment are analyzed. The preliminary test results for charging small ITO coated electric field plates are given, and the designs of a magnetic shielding system and cancellation coils are also described. We trapped the Cs and Rb atoms in the MOT, and launched Cs atoms up 90 cm from the MOT to the center of the measurement chamber while guided by a resonator enhanced 1D optical lattice trap with transport efficiency up to 50%. The 1064 nm wavelength optical lattice is made in a 2 m long build-up cavity of light, and provides a transverse guide depth of up to 250 μK. Before they reach the top of their trajectory, the atoms are stopped and cooled by optical molasses, becoming trapped in the 1D lattice. We also demonstrate multiple launches of Cs atoms to the trap.

TABLE OF CONTENTS

List of Figures

List of Tables

ACKNOWLEDGEMENTS

I am most grateful to my advisor Prof. David S. Weiss. His knowledge and experience in both experiment and theory have been an inspiration for me. His magic fingers in dealing with the apparatus and his great intuition in physics has always amazed me.

I would like to thank many colleagues who have contributed to this work. Dr. Jingbiao Chen worked with me on this project for about 3 years, and we did many things together. Neal Mayer helped me to check my English. Xiao Li, Dr. Karl Nelson and Dr. Toshiya Kinoshita also spent their time to help me when I needed them. I was really touched. The undergraduate students: Osama Kassis and Shanna Simmons worked with me on this project also and helped me with a large variety of things.

我最想感激是我的女儿，小小的年纪妈妈便离开了她．即使后来把她接到身边也没有太多的时间陪她玩．而她总是非常懂事．我还要感谢我的老公和父母这些年来给我的支持.

Chapter 1

Introduction of Electric Dipole Moment Theory and Experiments

Search for electric dipole moment (EDM) is one of the most important experiments in modern atomic physics. The experiments started about 50 years ago, and scientists have improved the sensitivity of experiments by many orders since then, but so far, no nonzero result has been found. The existence of a non-vanishing EDM in non-degenerate particles is predicted by the modern theories. In the CPT theorem, the combined charge and parity (CP) symmetry violation, which has been observed in particle physics experiments studying K and B mesons decay in 1964 [1] indicates that Time (T) symmetry should be violated also. But until now, there is no direct observation of T symmetry violation. Several models in quantum field theory predict different values of eEDM. Which model is correct will be decided by further experiments. The searching for EDM will provide a probe to test these models.

Modern experimental techniques, especially laser cooling and trapping, dramatically reduce noise sources and significantly improve the sensitivity in precision measurement experiments. Since laser cooling and trapping techniques were developed in 1980s [2-4], they have had a big impact in atomic physics, leading to the formation of the Bose-Einstein Condensate (BEC) [5] and degenerate fermions gas [6, 7]. One of the areas that these techniques have affected most is precision measurement. Cold atoms have been used in clocks [8, 9], gyroscopes [10], gravimeters [11], and measurements of

fundamental constants [12]. Some groups have started to set up experiments to test fundamental symmetries with cold atoms or molecules [13-15].

In this thesis, I will report on our experimental progress in the search for the electric dipole moment (EDM) of the electron using cold Cs and Rb atoms trapped in 1D optical lattices.

1.1. Time Reversal Symmetry and Electric Dipole Moments

Symmetry in physics refers to features of a physicsal system that are "unchanged" under certain transformations [16]. The transformations may be continuous or discrete. Continuous symmetry is characterized by invariance under a continuous change in the geometry of the system, such as time, spatial translation or spatial rotation. Discrete symmetry includes time reversal symmetry T, the direction of time is reversed, $t \mapsto -t$, parity symmetry P, the universe is reflected as in a mirror, $\vec{r} \mapsto -\vec{r}$, and charge conjugation symmetry C, reverse the sign of charge and magnetic moment of all particles [17], or turn a particle into its antiparticle and change the sign of its charge back. The combined CPT symmetry is conserved in quantum field theories (such as in standard model) [18]. So in the standard model, all physical laws remain unchanged in a mirror-image of our universe with all matters replaced by their antimatters, and the direction of time reversed. But individual symmetry (P, C or T) is not necessarily invariant in general. Dirac wrote in 1949 that “I do not believe there is any need for physical laws to be invariant under fluctuation in space and time although the exact laws of nature so far known do have this invariance” [19]. Since that was written, P violation

was observed by Wu [20] in 1957 in ^{60}Co β decay. Under charge conjugation, a left-handed neutrino changes into left-handed antineutrino. All observed neutrinos are left-handed and all observed antineutrinos are right-handed, so this symmetry is obviously broken [17]. The violation of combined CP symmetry was observed in the decay of the K_0 meson in 1964 [1]. If combined CPT symmetry is conserved, CP violation implies that T symmetry is also broken. It has also been proposed [21] that the mystery of the cosmological matter-antimatter asymmetry in our universe could come from baryon number non-conservation together with a CP violating interaction.

If a particle has a non-vanishing EDM, both P and T symmetry are broken. The EDM (d) of a particle is defined through the linear energy change in an external electric field E: $U = d \cdot \mathbf{E}$. Because both $\mathbf{E}$ and U are even variables under T reversal, while the d is odd under T reversal. Thus, if time reversal symmetry holds, a particle must have vanishing EDM. Contropositively, a non-vanishing EDM signal implys that T symmetry is broken. The electric dipole moment must lie along the particle spin [22] because, otherwise, we would be able to distinguish the states with "EDM up" and "EDM down", which adds two more states of a particle, and hence would result in nuclei and atoms with twice as many particles in each shell as we actually have due to the Pauli principle.

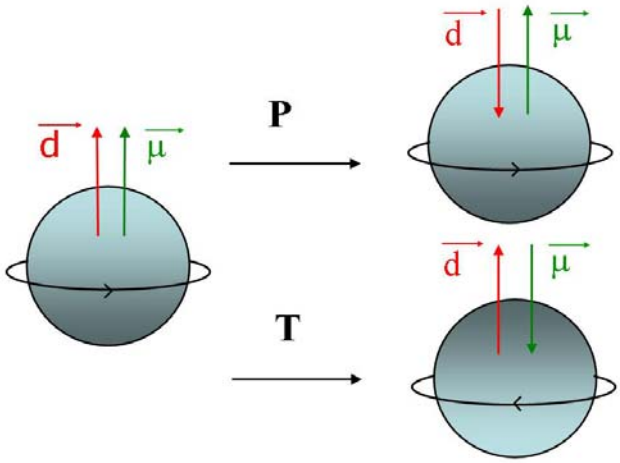

Fig. **1-1**: Transformations of magnetic dipole moment μ and electric dipole moment d under the time reversal T and parity reversal P. In each case, the result produces a different state with d anti-parallel to μ.

Under parity inversion and time-inversion, various quantities of interest transform as illustrated in Figure **1-1.** Under P reversal, the electric dipole moment changes direction and the magnetic dipole moment remains unchanged. Under T reversal, the electric dipole moment is unchanged and the magnetic dipole moment reverses direction. If T and P are good symmetries, the left and the right states are degenerate, which is not true in physics. If T and P are not good symmetries, as in the SM, *d* may be non-zero.

In fact many theories including the SM, do predict non-vanishing EDMs. In the SM, the violation of the combined C and P can be described with a phase (θ_{QCD}) in the Cabibbo-Kobayashi-Maskawa (CKM) matrix that accounts for quark mixing. The eEDM predicted by the SM is much smaller than the current experimental limit. Even though all experiments to date are consistent with the SM, there are still remaining challenges. The SM does not include gravity, fails to explain matter antimatter asymmetry or dark matter,

and has a "hierarchy" problem (the observed fundermental particle masses are surprisingly small). There are some possible extensions of the SM, such as SuperSymmetry (SUSY) [23, 24], Technicolor [24, 25], Left-Right symmetric models [26], Multi-Higgs model [27], and lepton flavor-changing model [28], which introduce new particles and forces to explain these problems, predict new sources of T violation, and consequently much larger electron EDMs, as shown in Table **1-1**. These predictions are very close to the current experimental sensitivities [29]. A measurement of the EDMs of fundamental particles can test new physics beyond the standard model, and will set a direct limitation on CP violation in strong interactions.

Table **1-1**: EDM prediction from different models.

model	$\|d_e\|$
Standard Model	$<10^{-37}$ e·cm
Left-right symmetric	10^{-26}-10^{-28} e·cm
Lepton flavor-changing	10^{-26}-10^{-29} e·cm
Multi-Higgs	10^{-27}-10^{-28} e·cm
Technicolor	10^{-27}-10^{-29} e·cm
Supersymmetry	$< 10^{-27}$ e·cm

1.2. Overview of the current electric dipole moment search experiments

The first experimental search for a permanent EDM of a fundamental particle was performed by Purcell and Ramsey in 1950 [30]. Since then, many groups have tried to measure EDMs [14, 29, 31]. Experimental searches for EDMs can be divided into three

categories based on sources of EDM. The underlying sources can be the neutron, the electron or a nucleus. The neutron is sensitive to the quark EDM, diamagnetic atoms (Hg, Xe, Rn) are sensitive to nuclear EDM, and paramagnetic atoms (Cs, Tl, Fr) and molecules (PbO, YbF, TlF) are sensitive to the electron EDM. The limits set by the most sensitive experiments in each category are comparable, and they constrain different combinations of CP-violating effects.

The current EDM limit for the neutron is 9.7×10^{-28} *e*-cm. The experiment was carried out by the Gatchina group [32, 33] using ultracold neutrons in a magnetic resonance spectrometer. In diamagnetic atoms, which probe nuclear EDM, the most sensitive experiment has been carried out with the ^{199}Hg atoms by the Fortson group. The limit is $d(^{199}\text{Hg}) = 2.1 \times 10^{-28}$ *e*-cm [31]. The experiment used hot ^{199}Hg atoms in a vapor cell. To measure the EDM, they measured the spin procession of polarized atoms by measuring the polarization change of a probe laser. The electron EDM has been searched for through atomic or molecular EDMs, which are enhanced compared with the electron EDM. The highest sensitivity to the electron EDM has been obtained with paramagnetic atoms, and is $d_e < 1.6\times10^{-27}$ *e*-cm [29]. The result was obtained by the Commin's group with hot Tl beams, where sodium atoms served as a comagnetometer to improve the sensitivity of the experiment. The Tl atoms were prepared in the $m_F = 0$ state and then transferred to a superposition of the $m_F = \pm1$ states. After the atoms passed through an electric field region, another RF pulse was applied. The number of atoms that returned back to the $m_F = 0$ state is related to the size of the EDM signal.

Other groups are also searching for the electron EDM with neutral molecules, ions or solid states. Molecules suitable for EDM experiments are usually polar and

diatomic [34, 35]. In these molecules, the effective internal electric field that an electron feels is much larger than the applied external fields, which provides a much larger enhancement factor than paramagnetic atoms can have. Hinds group has used YbF molecule beam to obtain the result d_e = -0.2±3.2×10^{-26} *e*-cm. Demille's group is attempting an experiment using hot PbO in a cell. An experiment with cooled molecular ions HfH^+ and PtH^+ trapped in an RF trap is being carried out in Cornell's group [13].

In 1968, Shapiro suggested that one could search for an electron EDM by applying a strong electric field to a solid, which has an unpaired electron spin at low temperature [36]. The signal to noise ratio can be much larger in a solid experiment than in the experiments with atoms or molecules. The EDM interaction would lead to a net sample magnetization that can be detected with a superconducting quantum interference device (SQUID) magnetometer. A method using a paramagnetic material has been proposed [37]. Another method for the detection of the EDM by measuring the voltage induced across the solid by the alignment of the sample's magnetic dipoles in an applied magnetic field B was introduced in [38]. It gave a limit on the electron EDM of 5×10^{-24} *e*-cm.

There are two other groups setting up experiments to measure EDMs with cold paramagnetic atoms. Heinzen's group is trying to measure EDM with cold Cs atoms trapped in a lattice and Gould's group is trying to measure EDM with Cold Cs fountain. Gould's current result is $-0.5 \pm 1.4 \times 10^{-22}$ e-cm [14].

Time reversal violation searches are also being carried out in other ways [39] besides with EDM measurements. Study of the angular correlation in β-decays [40, 41] is a complementary experiment for searching of the T symmetry broken, which is similar to

EDM searches. With the combination of laser cooling and trapping techniques and the recoil ion momentum spectroscopy [42], the experimental precision can be improved by investigation of β-decay of radioactive species.

1.3. The Electric Dipole Moment of paramagnetic atoms

Measuring the electron EDM directly would be difficult because electrons are accelerated in electric fields. This problem is avoided when electrons are bound in atoms. To the extent that there is an electron EDM, some atomic EDMs can be bigger, which make them good candidates to test electron EDM. But atomic EDMs are also sensitive to other sources of T-violation interactions. There are four mechanisms that might contribute to an atomic EDM [43]: the electron edm, a nuclear edm, T-violation quark-quark interaction and T-violation in the electron-nuclear interaction, as shown in Figure **1-2**. Paramagnetic atoms are not sensitive to nuclear EDM and quark-quark interactions. For a heavy paramagnetic atom, whose enhancement factor can be quite large, the atomic EDM mainly comes from electron EDM.

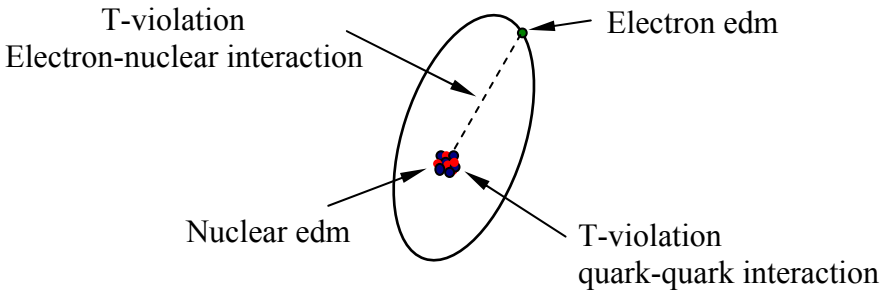

Fig. **1-2**: Four mechanisms could contribute to the atomic EDM. The EDM of

paramagnetic atoms are sensitive to the electron EDM.

1.3.1. Schiff theorem

For a neutral atom, there is no effect due to the EDMs of the constituent particles if they are non-relativistic point-like particles bounded by pure electrostatic force. The proof is given by Schiff [44]. The Hamiltonian of the EDM interaction is:

$$H_d = -\sum \overrightarrow{d_k} \cdot \vec{E}_{\text{int}}(r_k) \tag{1. 1}$$

The mixed state due to this perturbation is:

$$\left|n'\right\rangle = (1 + i\sum_k \frac{1}{e_k} \vec{d}_k \cdot \vec{p}_m)\left|n\right\rangle \tag{1. 2}$$

The EDM of the mixed state is

$$\left\langle n'\left|\sum_l e_l r_l\right|n\right\rangle = -\left\langle n\left|\sum_k d_k\right|n\right\rangle, \tag{1. 3}$$

which exactly cancels out EDM of any single individual particle. The net EDM of the particle is therefore zero. That is, when a particle is placed in an electric field, the electron cloud is rearranged to produce a net zero time average field for an electron.

1.3.2. Enhancement factors of atomic EDM

In real case, the approximations in Schiff's model are not totally satisfied. We list these conditions below [43, 45]:

- The particles have finite size and structure due to non-electrostatic forces.
- There are spin dependent contributions to the forces.
- There are relativistic corrections to the particle interactions.

- The particle spin direction is correlated with the electric field.

These effects can lead to nonzero effective internal electric field an electron can feel. Simply using second-order perturbation theory, one can calculate an approximate value for the atomic EDM D_A for a one-electron atom such as an alkali. Using a one-electron approximation for the alkalis, we have [18]:

$$D_A = \sum_{n'} \frac{\langle ns | -d_e(\beta - 1)\vec{\sigma} \cdot \vec{E} | n'P \rangle \langle n'p | -e\vec{r} | ns \rangle}{E_{ns} - E_{n'P}} + complex \quad conjugate \qquad (1.4)$$

The magnetic interactions increase rapidly with the atomic number Z, so the net EDM of a heavy paramagnetic atom can be much larger than the electron EDM. The enhancement factor R is:

$$R = \frac{d_a(atom)}{d_e(electron)} \propto \alpha^2 Z^3 \qquad (1.5)$$

,

where $R = \varepsilon_{eff} / \varepsilon_{ext}$, $\varepsilon_{eff} = P \cdot Q$, Q are relativistic effects that are proportional to Z^3 (Z is atomic number), and P is the particle's degree of polarization. Table **1-2** gives the enhancement factors of some atoms and molecules [29, 34, 35, 46].

Table **1-2**: Enhancement factors for several atoms and molecules

Particles	Cs	Rb	Tl	Fr	PbO	YbF
R	125.9	24.6	585	1150	60000	$\sim 1.6\times10^6$

In our experiment, we are using Cs and Rb atoms to measure electron EDM. Some molecules and atoms have very large enhancement factors. But the laser cooling

and trapping techniques for Cs and Rb atoms are also very mature, and they can be easily cooled to a very low temperature and trapped for a long time, which lead to a better sensitivity of atomic EDMs. It is unclear whether atoms or other systems will lead to the best ultimate sensitivity. Also, because the underlying atomic theory is so reliable for alkali atoms, with error bars below 3% [46, 47], they can yield the most precise information about the underlying time reversal symmetry breaking should the electron EDM be discovered if the alkali atoms are sufficiently sensitive.

1.4. General method for EDM measurement

The general way to detect the EDM of a particle is to apply an electric field and magnetic field, and measure the difference in the spin precession frequency under **E** reversal. The Hamiltonian of a particle with the total angular momentum **F** under electric field **E** and magnetic field **B** is:

$$H^{+} = (\mu\vec{B} + d\vec{E}) \cdot \frac{\vec{F}}{|F|}. \tag{1. 6}$$

With E-field reversal, the Hamiltonian becomes:

$$H^{-} = (\mu\vec{B} - d\vec{E}) \cdot \frac{\vec{F}}{|F|} \tag{1. 7}$$

The EDM signal is given by:

$$2d \cdot E = (H^{+} - H^{-}) \tag{1. 8}$$

1.5. Goals of our experiment

In our experiment, we will search for the electric dipole moment of the electron using Cs and Rb atoms in 1D optical lattice traps. With measurement time of about 3 seconds and 12 hours of integration time, our projected sensitivity is 3×10^{-30} *e*-cm, a 500-fold improvement over the current experimental limit of the electron EDM. A larger number of Rb atoms can be trapped in a lattice, which will compensate for its low enhancement factor, so that a same sensitivity of the EDM signal can be reached as with Cs atoms. They are used as a final check for the EDM signal is if nonzero EDM result is found.

In our experiment, the cooled Cs and Rb atoms will be trapped in two identical 1D optical lattices. With trapped and cold atoms, the systematic effect due to the motional induced magnetic field ($\propto v\times E$), which is a major systematic error in EDM searches with atomic beams, is dramatically reduced, and the applied electric field can be much higher than the E field used in cell experiments. Also, the measurement time, and hence inherent sensitivity, can be significantly larger. However, because the laser trap is on all the time during the experiment, the laser-atom interactions can introduce new systematic errors, which need to be considered.

1.6. Structure of this thesis

This thesis is organized as follows. In chapter 2, our EDM experiment is described in detail, and systematic errors and statistical noise sources are analyzed. In chapter 3, the design of the electric field plates is given, preliminary testing results of

small electric field plate charging are described, along with the design of magnetic field shielding and cancellation coils. In chapter 4, our current experimental setup is described in detail including the vacuum system, the laser systems for the magneto optical trap (MOT), molasses cooling and launching, cavity enhanced far off resonance 1D lattices, computer controlled system and detection system. In chapter 5, Cs atoms are demonstrated to be trapped in the MOT, and then launched 90 cm above MOT while guided by the 1D lattice. When the atoms reach the center of the measurement region, they are retrapped and cooled. Chapter 6 summarizes the current experimental results and describes our future plans.

References:

1. J. H. Christenson, J.W.C., V. L. Fitch *, and R. Turlay, *Evidence for the 2π Decay of the K_2^0 Meson.* Phys. Rev. Lett., 1964. **13**(4): p. 138.
2. D. J. Wineland, R.E.D., and F. L. Walls, *Radiation-Pressure Cooling of Bound Resonant Absorbers.* Phys. Rev. Lett., 1978. **40**(25): p. 1639.
3. Metcalf, W.D.P.a.H., *Laser Deceleration of an Atomic Beam.* Phys. Rev. Lett., 1982. **48**(9): p. 596.
4. W. Ertmer, R.B., J. L. Hall, and M. Zhu, *Laser Manipulation of Atomic Beam Velocities: Demonstration of Stopped Atoms and Velocity Reversal.* Phys. Rev. Lett., 1985. **54**(10): p. 996.
5. M. Anderson, J.E., M. Matthews, C. Wieman, and E. Cornell, *Observation of Bose-Einstein Condensation in a Dilute Atomic Vapor.* Science, 1995. **269**: p. 198.
6. M. Bartenstein, A.A., S. Riedl, S. Jochim, C. Chin, J. Hecker Denschlag, and R. Grimm, *Collective Excitations of a Degenerate Gas at the BEC-BCS Crossover.* Phys. Rev. Lett., 2004. **92**: p. 203201.

7. M. Greiner, C.A.R., and D. S. Jin, *Probing the Excitation Spectrum of a Fermi Gas in the BCS-BEC Crossover Regime.* Phys. Rev. Lett., 2005. **94**: p. 070403.
8. Kurt Gibble, S.C., *Laser-cooled Cs frequency standard and a measurement of the frequency shift due to ultracold collisions.* Phys. Rev. Lett., 1993. **70**: p. 1771-1774.
9. Martin M. Boyd, A.D.L., Sebastian Blatt, Seth M. Foreman, Tetsuya Ido, Tanya Zelevinsky, and Jun Ye, *87Sr Lattice Clock with Inaccuracy below 10-15.* Phys. Rev. Lett., 2007. **98**: p. 083002.
10. F. Yver-Leduc, P.C., J. Fils, A. Clairon, N. Dimarcq, D. Holleville, P. Bouyer, and A. Landragin, *Reaching the quantum noise limit in a high-sensitivity cold-atom inertial sensor.* J. Opt. B: Quant. Semiclass. Opt., 2003. **5**: p. S136.
11. Chu, M.K.a.S., *Measurement of the gravitational acceleration of an atom with a light-pulse atom interferometer.* Applied Physics B, 1992. **54**: p. 321-332.
12. D. S. Weiss, B.Y.a.S.C., *Precision measurement of the photon recoil of an atom using atomic interferometry.* Phys. Rev. Lett., 1993. **70**: p. 2706.
13. L. Sinclair, J.B., A. Leanhardt, E. Meyer, R. Stutz, E. Cornell. *An electron EDM search using trapped molecular ions*. in *DAMOP 2007*. 2007. Galgary, Canada.
14. Jason M. Amini, C.T.M.J., and Harvey Gould, *Demonstration of an Electron Electric Dipole Moment Experiment Using Electric-Field Quantization in a Cesium Cold Atom Fountain.* arXiv:physics, 2006. **v1**: p. 0602011.
15. H. Wang, D.F., A. Hime, D. Vieira, X. Zhao, *Towards a beta asymmetry measurement of polarized radioactive atoms in an optical dipole trap.* Bull. Ame. Phys. Soc., 2007. **52**(7): p. 149.
16. K. Brading, a.E.C., *Symmetries in Physics: Philosophical Reflections*. 2003: Cambridge Uni. Press.
17. Perkins, D.H., *Interduction to high energy physics*. 1987: Addison Wesley. 82.
18. I. B. Khriplovich, S.K.L., *CP violation without strangeness, electric dipole moment of particles, atoms, and molecules*. 1997: Springer. 37.
19. Dirac, P.A.M., *Forms of Relativistic Dynamics.* Rev. Mod. Phys., 1949. **21**: p. 392.

20. C. S. Wu, E.A., R. W. Hayward, D. D. Hoppes, and R. P. Hudson, *Experimental Test of Parity Conservation in Beta Decay.* Phys. Rev., 1957. **105**(4): p. 1413-1415.
21. Sakharov, A.D., Sov. Phys. JETP Lett., 1967. **5**: p. 24.
22. Hunter, L.R., *Tests of time-reversal invariance in atoms, molecules, and the neutron.* Science, 1991. **252**: p. 73-79.
23. Nilles, H.P., Phys. Rep., 1984. **110**: p. 1.
24. Triantaphyllou, T.A.a.G., Phys. Lett. B, 1992. **278**: p. 345.
25. Terning, T.A.a.J., Phys. Rev. D, 1994. **50**: p. 2116.
26. Pati, R.N.M.a.J.C., Phys. Rev. D, 1975. **11**: p. 2558.
27. Weinberg, S., *Gauge Theory of CP Nonconservation.* Phys. Rev. Lett., 1976. **37**(11): p. 657.
28. S. M. Barr, A.M., *Bounds on the electron electric dipole moment in a wide class of models.* Phys. Rev. Lett., 1987. **58**(3): p. 187.
29. B.C. Regan, E.D.C., C. J. Schmidt and D. DeMille, *New Limit on the Electron Electric Dipole Moment.* Phys. Rev. Lett., 2002. **88**: p. 071805.
30. Ramsey, E.M.P.a.N.F., *On the Possibility of Electric Dipole Moments for Elementary Particles and Nuclei.* Phys. Rev., 1950. **78**(6): p. 807.
31. M. V. Romalis, W.C.G., J. P. Jacobs *, and E. N. Fortson, *New Limit on the Permanent Electric Dipole Moment of 199Hg.* Phys. Rev. Lett., 2001. **86**(12): p. 2505.
32. I. S. Altarev, Y.V.B., N. V. Borovikova, A. I. Egorov, S. N. Ivanov, E. A. Kolomensky, M. S. Lasakov, and V. M. Lobashev and A.N.P. V. A. Nazarenko, A. P. Serebrov, Yu. V. Sobolev, and E. V. Shulgina, *Search for the neutron electric dipole moment.* Physics of Atomic Nuclei, 1996. **59**(7): p. 1152.
33. P. G. Harris *, C.A.B., K. Green, P. Iaydjiev, S. Ivanov, D. J. R. May, J. M. Pendlebury, D. Shiers, K. F. Smith, and M. van der Grinte, and P. Geltenbort, *New Experimental Limit on the Electric Dipole Moment of the Neutron.* Phys. Rev. Lett., 1999. **82**(5): p. 904.

34. D. DeMille, F.B., S. Bickman, D. Kawall, D. Krause, Jr., S. E. Maxwell, and L. R. Hunter, *Investigation of PbO as a system for measuring the electric dipole moment of the electron.* Physics Review A, 2000. **61**: p. 052507.

35. J. J. Hudson, B.E.S., M. R. Tarbutt, and E. A., *Measurement of the Electron Electric Dipole Moment Using YbF Molecules.* Phys. Rev. Lett., 2002. **89**(2): p. 023003.

36. Shapiro, F.L., Sov. Phys. Usp., 1968. **11**: p. 345.

37. Lamoreaux, S.K., *Solid-state systems for the electron electric dipole moment and other fundamental measurements.* Physics Review A, 2002. **66**(2): p. 022109.

38. B. J. Heidenreich, O.T.E., N. D. Charney, K. A. Virgien, A.W. Bridges, M. A. McKeon, S. K. Peck, D. Krause, Jr., and a.L.R.H. J. E. Gordon, S. K. Lamoreaux, *Limit on the Electron Electric Dipole Moment in Gadolinium-Iron Garnet.* Phys. Rev. Lett., 2005. **95**(16): p. 253004.

39. Angelopoulos, A., Phys. Lett. B, 1998. **444**: p. 43.

40. Herczeg, P., Prog. Part. Nucl. Phys., 2001. **46**: p. 413.

41. Wilschut, H., AIP conference proceedings, 2005. **802**: p. 223.

42. J. W. Turkstra, R.H., S. Knoop, R. Morgenstern, and R. E. Olson, *Recoil Momentum Spectroscopy of Highly Charged Ion Collisions on Magneto-Optically Trapped Na.* Phys. Rev. Lett., 2001. **87**(12): p. 123202.

43. Suzuki, W.B.a.M., *The electric dipole moment of the electron.* Rev. Mod. Phys., 1991. **63**: p. 313.

44. Schiff, L.I., *Measurability of Nuclear Electric Dipole Moments.* Phys. Rev., 1963. **132**(5): p. 2194.

45. Sandars, P.G.H., Phys. Lett., 1965. **14**: p. 194.

46. H. S. Nataraj, B.K.S., B. P. Das, R. K. Chaudhuri and D. Mukherjee, *The electron electric dipole moment enhancement factors of Rubidium and Caesium atoms.* ArXiv:physics, 2007. **0707**: p. 4086v1.

47. A.C. Hartely, E.L., A.M. Martensson-Pendrill, J. Phys. B, 1990. **23**: p. 3417.

Chapter 2
General Features of EDM Experiment and Noises and Systematic Errors Analysis

Our proposed EDM experiment uses cooled Cs and Rb atoms trapped in a pair of 10 cm long 1D optical lattice traps. The two species will not be trapped simultaneously, but rather used in alternating measurements. The projected sensitivity of the experiment is about 3×10^{-30} e-cm in a 12 hour of integration time. If atomic EDMs result from the electron EDM, Cs and Rb will differ by a factor of 5 [1]. This will provide a strong final check against systematic errors. Using cooled and trapped atoms dramatically suppresses motion-induced systematic error which is significant in the Tl beam experiment that sets current electron EDM limit, and also increases the measurement time compared with beam experiments. But trapping lasers can introduce new systematic errors. In this chapter, we outline the proposed experimental method, get the estimated shot noise limit, and analyze noise and systematic errors due to different sources.

2.1. Experimental Methods for electron EDM Search

2.1.1. General experimental description

The experiment is designed around a pair of parallel 1D far-off resonance optical lattice traps separated 10 mm apart, which allow the atoms to be coherently observed for more than 3 seconds. Each trap lies between two 30 × 4.2 cm parallel plates, one of which is shared, so that there is an electric field reversal within each measurement. The

atoms in one 1D lattice are spread over 10 cm (with a volume of ~ 10 mm^3). Small (0.8 mm) sections of atoms in each lattice will be independently imaged on 2 64-pixel photodiode arrays during the state-selective fluorescent detection. The measurement region is surrounded by magnetic shielding with the magnetic field shielded down to a few μGauss level. A small magnetic bias field (~100 nGauss) is scanned to produce independent Ramsey-type fringes for each subgroup of atoms. The sign of the electric field is reversed from shot to shot. The EDM signal is obtained by differential measurement in two positions (lattice 1 and lattice 2) under opposite signs of the electric field, and average over a long time (integration time *T*). The experimental sketch is shown in Figure **2-1.** The overall system sensitivity is proportional to $\frac{1}{RE_s\sqrt{N\tau T}}$ [2], where τ is the coherent measurement time in each shot. From this equation, we can see that in order to increase the sensitivity, we need larger E fields, and more atoms observed for a longer time. The features of our proposed experiment are first that we can apply high E field (~10^5 V/cm) in ultrahigh vacuum. With small residual magnetic fields, the electric field defines the atoms' quantization axis. Atoms trapped in far-off resonance lattice traps have long lifetime (some experiments show that lifetimes in the lattice are a few tens seconds [3]), so the coherent measurement time can be much longer than the time in beam experiments. With cold atoms trapped in lattices, the systematic error due to the motional B field, $\boldsymbol{v}\times\boldsymbol{E}$, is negligible. With the symmetric design of the experiment, common noise in the 2 lattices can be cancelled.

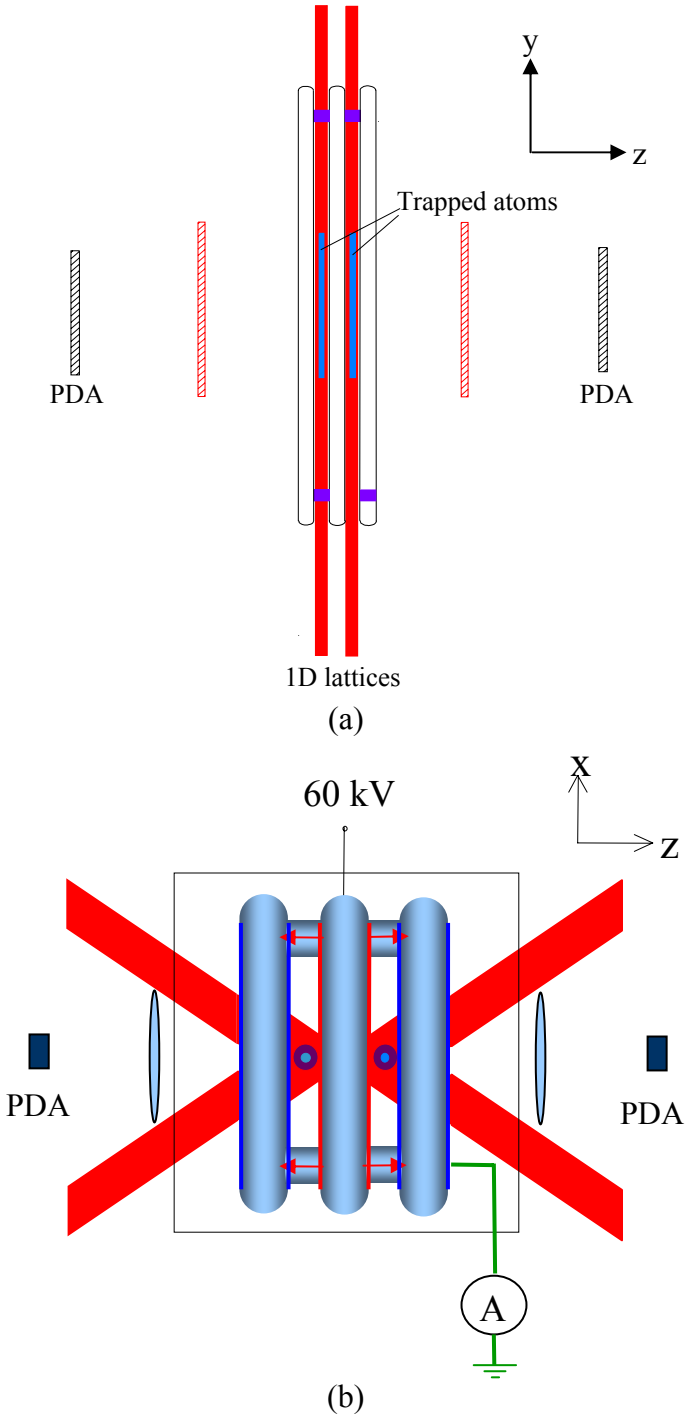

Fig. **2-1**: Experimental sketch. The atoms are trapped in 2 parallel 1D optical lattices, and stretch out over 10 cm in the vertical direction. Each lattice lays in between 2 glass electric field plates. The center plate is shared and connected to high voltage. (a) Side view of the experiment; (b) Top view of the experiment

2.1.2. State preparation

Atoms are first loaded from a Zeeman slower into a MOT, which is about 90 cm below the measurement region. After loading, the MOT magnetic field is changed to move atoms 5 mm away from the MOT center so that they overlap with one of the 1D lattice traps. Then, the MOT magnetic field is turned off and the detuning of the optical molasses (OM) laser beams is changed to create a moving reference frame [4] for the atoms. The OM beams are then shut off so that the atoms are launched upward, guided by the lattice in the horizontal direction. Before the atoms reach the top of their trajectory, 3 pairs of optical molasses beams in the measurement region are turned on to stop and cool the atoms. Once cooled, they will be trapped in 1D lattice. With multiple launches, and by switching loading between two lattices, atoms can be trapped in two adjacent 10-cm high sections of the parallel lattices. The total effective trapping volume exceeds 10 mm^3 (The atomic density distribution is the Gaussian shape. The atomic density $1/e^2$ in the trap is at the position of half of the full potential). Therefore 2×10^8 Cs atoms or 4×10^9 Rb atoms can be trapped at a sufficiently low density to avoid collisional dephasing during the measurement time [5].

After the traps are loaded, a small magnetic field is applied to define the quantization axis, and atoms are optically pumped to the stretched states. They are then transferred to the $m_F = 0$ states by several microwave π-pulses with different frequencies. Figure **2-2** shows an example of state preparation for Cs atoms. Atoms are optically pumped to the |4, 4> state first by σ+ light on resonance with the |F=4> to |F'=4> transition. With 4 (5) π pulses, Cs atoms are transferred to |4, 0> (|3, 0>) state.

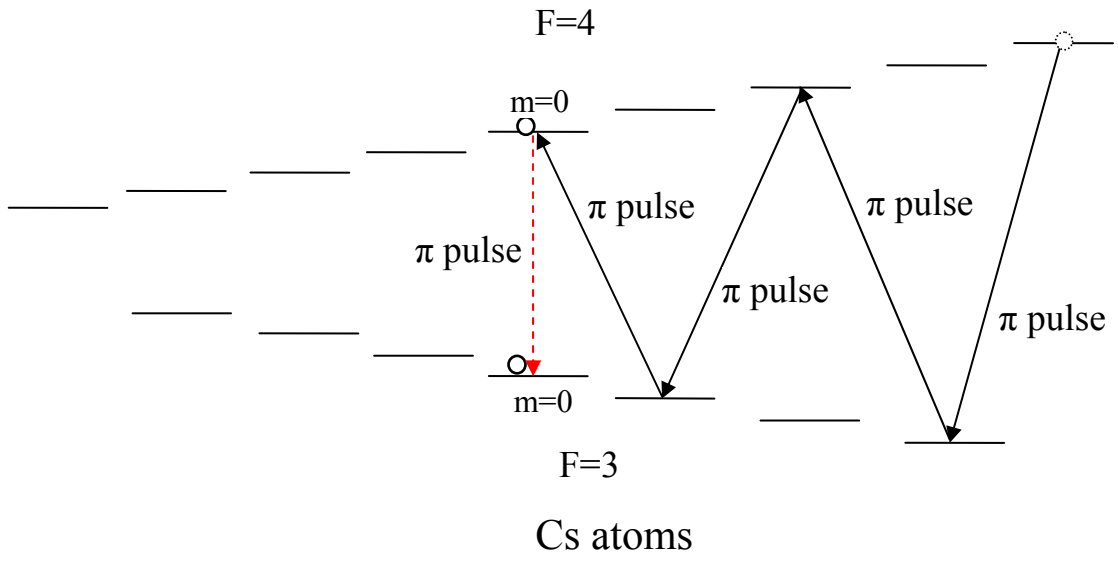

Fig. **2-2**: Cs atoms states' prepare. The Cs atoms are optically pumped to $|4,4\rangle$ state, with 4 or 5 different frequencies microwave π-pulses, the atoms will be transferred to F=4, m=0 state or F=3, m_F=0 state.

Cs atoms can also be optically pumped to |3, 3> by σ+ light on resonance with the |F=3> to |F'=3> transition. Rb atoms can be optically pumped to the |2, 2> (or |1, 1>) state, and then be transferred to the |1, 0> or |2, 0> state. After atoms are prepared in the m_F=0 state, the magnetic field direction is rotated to the z-axis, and then the magnitude is lowered while the electric field plates are charged to E_s ~150 kV/cm in 1 second. At the same time, the lattice depth is lowered to about 10 μK. A series of low frequency electromagnetic π-pulses will sequentially and coherently transfer atoms from $|F,0\rangle$ to a superposition of the stretched states. Atoms evolve under the E and B fields for a time τ. The phase difference between the two stretched states will be accumulated during this measurement time. Then atoms will be transferred to the m_F=0 state by another series of low frequency electromagnetic π-pulses. The number of atoms returned back to the m_F=0

state will be related to the energy difference between the stretched states, which is related to the EDM signal. The energy levels of Cs atoms' F=3 hyperfine level under an E field are shown in Figure **2-3** as an example.

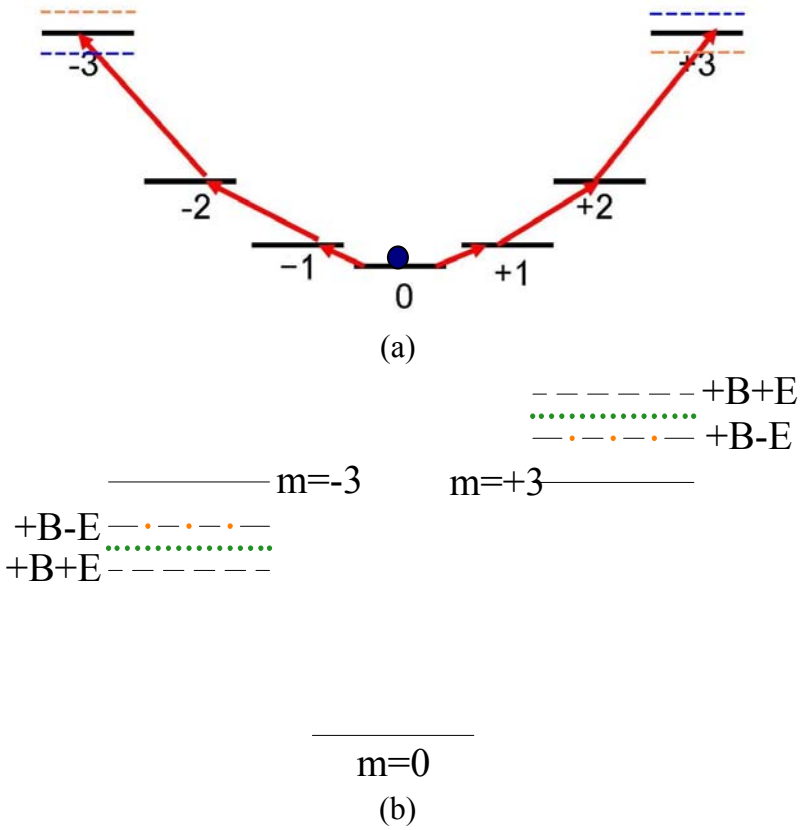

Fig. **2-3**: The F=3 energy level diagram of Cs atoms in combined applied fields. (a) Cs F=3 ground states in the E field and B=0. The E-field defines the atoms' quantization axis. The dotted lines are energy levels for a non-zero EDM. Blue: V; Orange: -V. (b) Energy levels under E field and a small bias B field. B is small enough that the energy splitting due to B field is much less than the quadratic DC Starks shift, so the E-field still defines the atoms' quantization axis. The solid lines are the energy levels for zero B field and zero EDM. Dotted lines are energy levels under B field without the EDM signal. Dashed lines and dash dot lines reflect the EDM signal under E reversal at a small bias B field.

The Cs atoms F=3 hyperfine level energy splitting in the electric field E_s is [6, 7]:

$$\frac{\delta\omega_{DC}}{2\pi} = -\frac{1}{2}E_s^2(\alpha - \frac{9}{7}\alpha_{10} + \frac{3m_F^2 - 12}{28}\alpha_{12})/h, \qquad (2.\ 1)$$

where $\alpha / h = 1.00 \times 10^{-5} Hz/(V/m)^2$, $\alpha_{10} / h = 1.99 \times 10^{-10} Hz(V/m)^2$, and $\alpha_{12} / h = 3.65 \times 10^{-12} Hz/(V/m)^2$. With E_s = 150 kV/cm, the energy splitting is:

$$\frac{\delta\omega_{DC}}{2\pi} = -\Delta E - 0.2 E_s^2 m_F^2 \times 10^{-8} \sim (1.13 \times 10^9 + 45 m_F^2)[Hz].$$

In zero B field, the energies of the $|F, \pm m_F\rangle$ states are different if the EDM signal is not zero. But this difference is the same under the E reversal. Under a small bias B field, the energy levels are shown in the Figure **2-3** (b) (For convenience, only m_F=0, and m_F=±3 states are shown there). If there is an EDM, the energy difference between two stretched states will be different under the E reversal. The EDM signal can be obtained by measuring this difference.

For Rb atoms F=1, there are 3 states. For Rb atoms F=2 or Cs atoms, there are more than 3 states. To simplify the expression, we only include m_F = 0 and stretched states in the states' evolution, since the other states only have non-zero populations while the states are being transferred and will not affect the results. The state evolution is shown in equation 2.2.

$$|\Psi_0\rangle = \begin{pmatrix} 0 \\ 1 \\ 0 \end{pmatrix} \xrightarrow{EM\ \ pulses} \frac{1}{\sqrt{2}} \begin{pmatrix} 1 \\ 0 \\ 1 \end{pmatrix} \xrightarrow{evolution} \frac{1}{\sqrt{2}} \begin{pmatrix} e^{\frac{-i(\eta_B \mu g B + \eta_E E d)\tau}{\hbar}} \\ 0 \\ e^{\frac{+i(\eta_B \mu g B + \eta_E E d)\tau}{\hbar}} \end{pmatrix} \qquad (2.2)$$

where, η_B (η_E) is +1 when the B (E) field is along the +z axis; and -1 when it is along the –z axis. After a time τ, another coherent series of low frequency electromagnetic pulses will be applied, and the state will become:

$$\begin{pmatrix} \frac{-i}{\sqrt{2}}\sin(\frac{\eta_B\mu_B g_F m_F B + \eta_E E d_a}{\hbar}\cdot\tau) \\ \cos(\frac{\eta_B\mu_B g_F m_F B + \eta_E E d_a}{\hbar}\cdot\tau) \\ \frac{i}{\sqrt{2}}\sin(\frac{\eta_B\mu_B g_F m_F B + \eta_E E d_a}{\hbar}\cdot\tau) \end{pmatrix}$$

The fraction of atoms returning back to m_F=0 is sensitive to the phase difference between the stretched states, which is proportional to the energy differences between these 2 states. This is similar to the previous thallium atomic beam experiment [8], but here the small bias B field is less than 5 μG (energy splitting between m_F=+3 and m_F=-3 states is only a few Hertz under this B field), and can be treated as a perturbation:

$$\frac{n_0}{n} = \cos^2(\frac{\eta_B\mu_B g_F m_F B + \eta_E E d_a}{\hbar}\cdot\tau) \qquad (2.\ 3)$$

By scanning the bias B field, we can get a Ramsey fringe-like signal, as shown in Figure **2-4**. The Ramsey fringe width is $1/2\tau$.

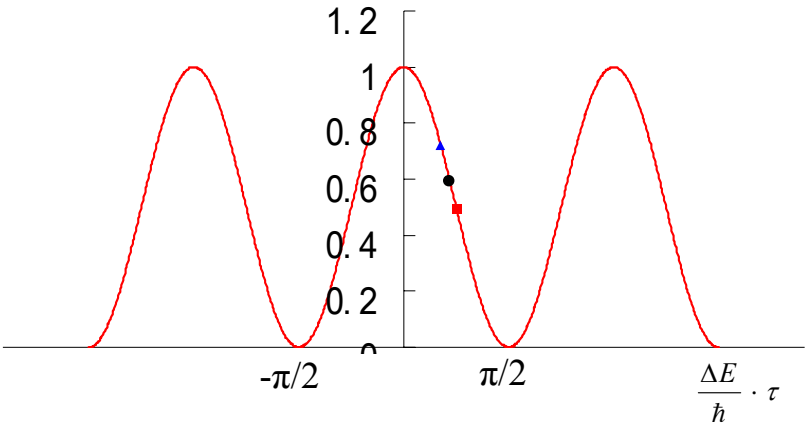

Fig. **2-4**: Ramsey fringe like signal by scanning the small B field. At τ=3 seconds, B = 40 nGauss corresponds to the π/2 point for Cs F=3, m_F=3.

2.1.3. Experimental general sensitivity

The EDM is a very small signal, which cannot be measured directly from the phase. A differential measurement is necessary to cancel out noise and systematic shifts. In our experiment, there is an E reversal in one measurement (2 adjacent positions 1 and 2 as shown in Figure **2-5**). There is also an E reversal in one place from shot to shot.

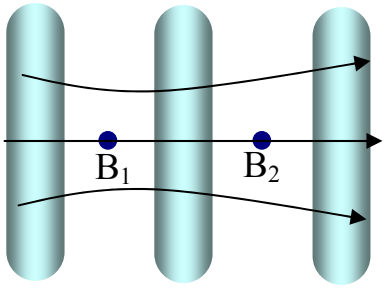

Fig. **2-5**: Residual magnetic field

We assume that in a small bias B field, the phase of the Ramsey fringe is changed to the position of the black dot in Figure 2.4 under zero EDM signal. If there is an EDM, under one E field, the phase is increased (the red square in Figure 2.4), under the opposite E field, the phase is decreased (the blue triangle in Fig 2.4). The EDM signal is obtained by measuring the phase difference between the red point and the blue point. The B field will be scanned over the whole Ramsey-like fringe to get the average signal. A B-field noise will cause the noise on the separation of stretched states, which is what we measured to get EDM signal, so this experiment is very sensitive to magnetic field noise. The B fields are different in the position 1 and 2 as shown in the Figure **2-5**. The magnetic of the B field can be expressed in the form:

$$B = B(z,t) = B_0 \pm \frac{\Delta B_z}{2} \pm \frac{\delta B_z}{2} \pm \frac{\delta \Delta B_z}{2}, \qquad (2.\ 4)$$

where ΔB_z is constant B-field gradient between position 1 and 2; δB_z is the B-field fluctuation between the +E and –E measurements, which is the same in space; $\delta \Delta B_z$ is the B field gradient fluctuation, which is a function of space and time. The EDM signal is obtained from equation 2.5:

$$\frac{4Ed_a}{\hbar} \cdot \tau = (\varphi_1^+ - \varphi_2^+) - (\varphi_1^- - \varphi_2^-), \qquad (2.\ 5)$$

where φ_1^+ and φ_2^+ are the phases at lattice 1 and lattice 2 respectively, φ_1^- and φ_2^- are the phases under the E reversal. We have:

$$\begin{cases} \varphi_1^+ = \dfrac{\mu_B g_F (B_0 + \dfrac{\Delta B_z}{2} + \dfrac{\delta B_z}{2} + \dfrac{\delta \Delta B_z}{2}) + Ed_a}{\hbar} \cdot \tau \\ \varphi_1^- = \dfrac{\mu_B g_F (B_0 + \dfrac{\Delta B_z}{2} - \dfrac{\delta B_z}{2} - \dfrac{\delta \Delta B_z}{2}) - Ed_a}{\hbar} \cdot \tau \end{cases},$$

$$\begin{cases} \varphi_2^+ = \dfrac{\mu_B g_F (B_0 - \dfrac{\Delta B_z}{2} + \dfrac{\delta B_z}{2} - \dfrac{\delta \Delta B_z}{2}) - Ed_a}{\hbar} \cdot \tau \\ \varphi_2^- = \dfrac{\mu_B g_F (B_0 - \dfrac{\Delta B_z}{2} - \dfrac{\delta B_z}{2} + \dfrac{\delta \Delta B_z}{2}) + Ed_a}{\hbar} \cdot \tau \end{cases} \quad (2.\ 6)$$

We can see clearly that the residual field B_0 has been cancelled, the B field gradient ΔB_z is cancelled by reversing the sign of the E field from shot to shot, and the field fluctuation δB_z (common mode noise) is cancelled in the measurements of two lattices in one shot. The only remaining term is the field gradient fluctuation $\delta \Delta B_z$. We have:

$$(\varphi_1^+ - \varphi_2^+) - (\varphi_1^- - \varphi_2^+) = \frac{4Ed_a}{\hbar} \cdot \tau + 2\delta \Delta B_z \quad (2.\ 7)$$

As shown in equation 2.7, the field gradient fluctuation $\delta \Delta B_z$ cannot be cancelled out by the differential measurement and needs to be take care of.

2.2. Shot noise limitation

The maximum achievable signal-to-noise S/N for detecting N uncorrelated atoms is limited by quantum statistics to $\sqrt{N}$ [9, 10] (shot noise limit). In real experiments, there are different sources of noise or systematic errors. In order to achieve the shot noise limit, all noise and systematic errors need to be less than or comparable to the shot noise limit. For the uncorrelated noise, increasing shots of the measurements will average it out and reduce the noise level. It needs to be less than the shot noise per measurement (per group). The number of atoms in one group is the number of atoms along the coherent length in one lattice per shot. If the coherence length is shorter than the pixel size of photodiode, the photodiode size is used. For instance, the coherent length of the collision induced noise is very small, the number of one group of atoms is the number of atoms, which signal is collected by one photodiode array pixel. While for the noise induced by the trapping laser, which is exactly same in one lattice, the number of one group of atoms is the total number of atoms in one lattice per shot (we call it shot noise per shot). Some interactions shift the difference of the stretched states differently under opposite E-field. This difference is the same from shot to shot, and cannot be averaged out by many measurements. They will give some offset on the measurement from the real EDM number, and cause an error. These systematic errors need to be less than the system sensitivity, which is set by the shot noise limit contributed from the total number of atoms in the whole integration time. If the integration time is 12 hours, the measurement time is 3 seconds, and the number of Cs atoms in one lattice is 10^8 atoms per shot, these three levels of shot noise limits are:

$$\begin{cases} \dfrac{\delta\omega_{pg}}{2\pi} = \dfrac{1}{\tau\sqrt{N\cdot\dfrac{l_{coherence}}{100}}} \sim 4\times10^{-4}/\sqrt{l}\,(Hz) & per\quad group\,(l\quad in\quad mm) \\ \dfrac{\delta\omega_{ps}}{2\pi} = \dfrac{1}{\tau\sqrt{N}} \sim 3\times10^{-5}\,(Hz) & per\quad shot \\ \dfrac{\delta\omega_{\mathbf{a}}}{2\pi} = \dfrac{1}{\sqrt{NT\tau}} \sim 3\times10^{-7}\,(Hz) & system\quad sensitivity \end{cases} \tag{2. 8}$$

For 2×10^9 Rb atoms. These three levels of shot noise limits are:

$$\begin{cases} \delta\omega_{pg} = \dfrac{1}{\tau\sqrt{N\cdot\dfrac{l_{coherence}}{100}}} \sim 0.9\times10^{-4}/\sqrt{l}\,(Hz) & per\quad group\,(l\quad in\quad mm) \\ \delta\omega_{ps} = \dfrac{1}{\tau\sqrt{N}} \sim 0.7\times10^{-5}\,(Hz) & per\quad shot \\ \delta\omega_{\mathbf{a}} = \dfrac{1}{\sqrt{NT\tau}} \sim 0.7\times10^{-7}\,(Hz) & overall \end{cases} \tag{2. 9}$$

The measurement sensitivity will ultimately be decided by the extent to which the experiment can reach its shot noise limit. The EDM signal is found by measuring the phase shift on the Ramsey fringes. For a signal atom with phase φ, on the Ramsey fringe, the possibility to measure 1 is $\cos^2\varphi$, the possibility to measure 0 is $\sin^2\varphi$. The noise on a signal measurement is:

$$\cos^2\varphi(1-\cos^2\varphi) + \sin^2\varphi\cdot\cos^2\varphi \tag{2. 10}$$

The phase shot noise $\delta\varphi$ can be obtained from the total number of atoms n by:

$$\delta(\cos^2\varphi) = 2\cos\varphi\sin\varphi\delta\varphi = \frac{2}{\sqrt{n}}(\cos^2\varphi\sin^2\varphi)\,. \tag{2. 11}$$

$$\Rightarrow \quad \delta\varphi = \frac{1}{\sqrt{n}}(\cos\varphi \sin\varphi) \tag{2. 12}$$

The EDM measurement is measure the phase difference on the Ramsey fringe. The EDM measurement sensitivity limited by shot noise is:

$$\begin{aligned} &\frac{4E_s R \cdot \langle \delta d_e \rangle}{\hbar} \cdot \tau = \frac{\delta\varphi}{slope} = \frac{1}{2\sqrt{n}} \\ &\xrightarrow{n = N \cdot (T/2\pi)} \langle \delta d_e \rangle = \frac{\hbar}{4 \cdot E_s R\sqrt{NT\tau/2}} \end{aligned} \tag{2. 13}$$

With the total numbers of 10^8 and 2×10^9 atoms for Cs and Rb respectively in one lattice, the experimental sensitivities for Cs and Rb atoms are: (under the E_s field 150 kV/cm, τ is 3 seconds, T is 12 hours)

$$\begin{cases} d_e \sim 3\times10^{-30} e-cm & Cs \\ d_e \sim 3\times10^{-30} e-cm & Rb \end{cases}. \tag{2. 14}$$

2.3. Experimental requirements and noise analysis

Before analyzing the noise and systematic errors, we need to think about the basic requirements of the experiment. After atoms are prepared in the measurement region and the right state, they need to remain the phase coherent during the measurement. To have a lifetime about 10 seconds in the trap, the vacuum needs to be better ~ 2×10^{-10} torr, and the heating due to the trapping laser needs to be small during the measurement. Also, photon scattering will change the phase of states, which needs to be considered.

2.3.1. Scattering and heating from the trapping laser

a. Photon scattering

During the measurement, atoms will be trapped in far-off resonance 1D lattices. Scattering of a photon from a trapping light field will cause the atom to dephase [11], which is very critical in the EDM experiment. The scattering rate needs to be less than the coherent measurement time.

The scattering rate due to light that is δ detuned from resonance, with saturation parameter s_0, and natural linewidth γ can be found with [12]:

$$\Gamma_s = \frac{s_0 \gamma/2}{1 + s_0 + (2\delta/\gamma)^2} \approx \frac{s_0 \gamma/2}{(2\delta/\gamma)^2} \qquad (2.\ 15)$$

For a YAG laser trap with a depth of 10 μK, the scattering rate is about $2\pi\times3\times10^{-2}$ s^{-1} (0.2 s^{-1}) for Cs atoms, and 0.1 s^{-1} for Rb atoms.

b. Trap potential noise induced heating.

The dynamics of noise-induced heating of atoms in dipole traps has been discussed in detail in[13]. Beam pointing noise causes fluctuations of the trap center, and leads to a constant heating rate, while intensity noise causes fluctuations in the trap spring constant and results in exponential heating. Our trap is a resonator-enhanced 1D optical lattice trap. It has a well defined spatial mode, so beam pointing noise is converted into intensity noise.

The heating rate constant Γ (energy e-folding rate) due to the intensity noise can be found with [13]:

$$\Gamma_h = \frac{1}{T_h(\text{sec})} = \pi^2 \omega_x^2 S_k(2\omega_x), \qquad (2.\ 16)$$

where ω_x is the trapping frequency. $S_k(2\omega_x)$ is the one sided power spectrum of the fractional fluctuation in the spring constant, defined as [13]:

$$S_k(\omega) = \frac{2}{\pi}\int_0^\infty d\tau \cos\omega\tau \left\langle \varepsilon(t)\varepsilon(t+\tau)\right\rangle, \qquad (2.\ 17)$$

where ε(t) is the fractional fluctuation of the intensity (defined as: $\frac{I(t) - \langle I \rangle}{\langle I \rangle}$). To get an energy *e*-folding time of 10 s at about 10 μK trap potential (the trap frequency ω_a = 35 kHz, ω_r = 13 Hz), the power spectrums of the intensity fractional fluctuation $S(2\omega_a) < 4\times10^{-12}$ (frac^2/Hz), $S(2\omega_r) < 2.5\times10^{-5}$ (frac^2/Hz) respectively.

2.3.2. Noise analysis

Interactions of atoms with the E field, the B field and the trapping laser field shift atomic Zeeman levels. Fluctuations in these fields affect the final measurement accuracy and sensitivity. Collisions between atoms also shift the energy levels between states. The interactions which are proportional to m^2 shift the energy levels of $\pm m_F$ states same amount. A constant shift can be compensated by changing the frequencies of π pulses to match the transition resonance. But fluctuations introduce noise in the contrast of the Ramsey fringe, and then introduce noise in the phase measurement. Some interactions

shift the $\pm m_F$ levels differently (such as the residual B field, trapping laser vector light shift). If the frequency of the electric-magnetic π pulse (used to transfer atoms to the superposition states) is set to the average of the two frequencies, it reduces the Ramsey fringe contrast. A constant reduced contrast does not affect the measurement sensitivity as shown in Figure **2-6**.

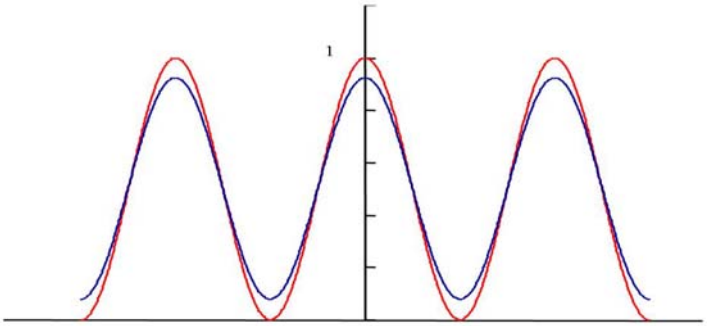

Fig. **2-6**: Ramsey fringe. The red one is the curve when the frequency of magneto-electrical pulse is on resonance. The blue one is curve when the frequency is not on resonance.

Fluctuations in the contrast will introduce noise in the measurement. Also the fluctuations in the detection system, such as the detection laser frequency and intensity noise, and electric noise in the detectors will affect the sensitivity and need to be controlled down to certain level.

Common mode noise will not limit measurement sensitivity even if the phase noise is more than a Ramsey fringe linewidth [14]. Fluctuations in the magnitude of E and B field are all common mode noise. Noise in the detection laser frequency and intensity is also common mode. In our experiment, the 2 lattice traps come from one laser, which is split into two beams by a beam splitter and injected into two cavities. The

injection laser frequency and intensity noise are exactly same for the two, but the cavity build-up coefficient might be different. This introduces different light fields in 2 adjacent lattices, and represents a substantial problem for EDM experiments [need to be controlled to less than the shot noise per shot, which will be discussed in 2.4.3.]

2.4. Statistical noises

The effects of noise that is uncorrelated in the y direction are significantly reduced because the noise is averaged out by detecting atoms with ~100 independent subgroups in one lattice. The collision induced frequency shift and phase shift, and the electronics noise in the detection system are noises of this type. The fluctuations of the B-field gradient come from the residual B field gradient due to the imperfection shielding magnetization of the shields and the current Johnson noise of the electrodes. The coherence length of the Johnson noise is roughly the distance between the electrodes and atoms (2 mm), while the coherence length of residual B field fluctuations can be much larger. The noise from the trapping laser is the same in the whole 1D lattice, and cannot be averaged out by independent subgroup measurement in one lattice. It needs to be controlled down to the shot noise per shot level.

2.4.1. Magnetic field gradient fluctuation

The magnetic field gradient fluctuations come from two sources. One is the residual magnetic field fluctuation, which is due to the environmental B field fluctuation.

This fluctuation is correlated in space. The worst case is that this fluctuation is same along one lattice. In order for this noise to be less than the shot noise per shot, the B gradient fluctuation needs to be less than:

$$2m_F g\mu_B \delta B_{grad} \cdot l_l \le \Delta\omega_{ps} \Rightarrow \delta B_{grad} = \begin{cases} 14\,pGauss/cm & Cs \\ 3.2\,pGauss/cm & Rb \end{cases} \qquad (2.\ 18)$$

The other source is the magnetic noise induced by Johnson noise from the electrodes and magnetic shielding. Its effect in EDM measurements was first pointed out by Lamoreaux [15]. The results for the ^{199}Hg–cell EDM measurement, the Cs-cell EDM measurement, and Tl-beam EDM measurement have been calculated in detail [15]. In our experimental design, the noise correlation length is about 2 mm in the y direction (the distance from the electrodes to the atoms). The distance between the 2 lattices is 10 mm, so the effective magnetic field is uncorrelated. The noise on the energy splitting needs to be less than the shot noise per group (with 2mm group size). Similar to equation 2.17, we have:

$$2m_F g\mu_B \delta B \le \Delta\omega_{pg} \quad \Rightarrow \delta B = \begin{cases} 180\,pGauss & Cs \\ 40\,pGauss & Rb \end{cases} \qquad (2.\ 19)$$

In our EDM experiment, the size of the atomic distribution and its distance to the electrodes (2 mm) are much smaller than the electrode size (300 mm × 42 mm, thickness 6 mm), so it is reasonable to treat the electrodes as infinite conducting slabs, which were analyzed in detail in[16, 17]. The vertical component of the DC magnetic noise field is:

$$B_{n,z}(\omega = 0) = \frac{\mu}{2}\sqrt{\frac{\sigma_e k_B T_{tem}}{2\pi} \cdot \frac{t_{th}}{z_l(z_l + t_{th})}}, \qquad (2.\ 20)$$

where T_{tem} is the temperature 300 K, μ is the magnetic permeability ($\mu=\mu_0$, $\mu_0 = 4\pi\times10^{-7}$ H/m =1.257 x 10^{-6} H/m, is the vacuum permeability), σ_e is the electric conductivity of the electrodes, k_B is Boltzmann constant (1.38×10^{-23}m^2 kg s^{-2} K^{-1}), t_{th} is the slab thickness, and z_l is the vertical distance to the slab. The noise field components in the horizontal directions are:

$$B_{n,x} = B_{n,y} = \frac{1}{\sqrt{2}} B_{n,z} \qquad (2.\ 21)$$

The sheet resistivity of the ITO coating we used for the test plates is 100 Ω/square ($\sigma_e \sim 10^5$ (Ωm)$^{-1}$). For 2 ITO coated glass plates 2 mm away from the clouds with this sheet resistivity, the magnetic field noise is about 16 pGauss/√Hz, which corresponds to 10 pGauss in a 3 seconds measurement time, which meets the experimental requirement.

Besides the electrodes, another main Johnson noise source is from the high-permeability magnetic shield material. Romalis calculated the Johnson noise from a 40 cm diameter, 60 cm length cylinder shield in [18]. His results show that the magnetic noise at the center is 70 pG/√Hz, and the noise gradient is 7 pG/cm/√Hz. In our experiment, what we care about is the noise gradient. We will use the same diameter shield as the innermost one, but with MetGlas tape as the shield material instead of μ metal. The results should have the same order, and are much smaller than the requirement.

2.4.2. Collisions induced frequency shift

At low temperatures, which are favorable for laser-cooled experiments, the scattering cross sections increase. Frequency and phase shift due to collisions between the trapped atoms could become quite significant.

The collision induced frequency shift in an electron EDM experiment has been studied in detail [5]. It can be expressed as:

$$\delta\omega_c = \sum_m n_m \langle v_a \lambda_m \rangle_{therm} . \qquad (2.\ 22)$$

where v_a is the relative velocity of the atoms, n_m is the partial density in state , λ_m is the cross section for s-wave scattering in m state. At zero magnetic field $\lambda_{f,m_f} = -\lambda_{f,-m_f}$. λ_m is about 10^{-12} cm^2 for the Cs $|3,-1\rangle \leftrightarrow |3,1\rangle$ transition at a few μK. For n = 10^{10} atoms/cm^3, v_a =2 cm/s, and assuming λ_m has the same order for the $|3,-3\rangle \leftrightarrow |3,3\rangle$ transition as of $|3,-1\rangle \leftrightarrow |3,1\rangle$ transition, the fluctuation of the density difference between the states $|3,-3\rangle$ and $|3,3\rangle$ per shot needs to be less than 2% to reach the shot noise limit. Line broadening due to collisions of Cs atoms is on the order of 0.01 Hz [5], which is much less than the Ramsey fringe linewidth, and will not cause problems.

2.4.3. Differential intensity fluctuations in the trapping laser

As we mentioned before, the trapping laser can have different noise in the two lattices due to different enhancement factors of the two cavities. The Hamiltonian of atom-laser interactions can be written as [20]:

$$H_{laser} = -\frac{1}{2}\alpha_{ac} \cdot \varepsilon_l^2 - \beta \vec{f} \cdot \vec{k}\varepsilon_l^2 - \vec{\varepsilon}_l^* \cdot \vec{\vec{T}}_{ac} \cdot \vec{\varepsilon}_l , \qquad (2.\ 23)$$

where α_{ac} is the scalar part of the ac polarizability, k is the wave vector of the laser, β is a constant that depends on the laser detuning and the polarization, T_{ac} is the tensor part of the ac polarizability. The first term provides a potential to trap atoms. It is independent of the Zeeman sublevels. The second term is the vector light shift, proportional to m, and the third term is the tensor light shift, which is proportional to m^2.

The tensor light shift has the following form:

$$\Delta\omega = \nu_T(F)(3\cos^2\varphi_T - 1)m^2, \qquad (2.\ 24)$$

where φ_T is the angle between the electric field of the trapping light and the spin quantization direction of atoms. In our experiment, we set it to be zero or $\pi/2$. ν_T is about 0.02 Hz at 10 μK lattice trap potential [2]. If the two states are separated by 100 Hz, the duration of a π pulse is 50 ms. Being 0.02 Hz off-resonance reduces the Ramsey fringe contrast by about 4×10^{-7} ($(\frac{\Omega}{\Omega'}\sin\frac{\Omega' t_\pi}{2})^2$, where Ω is the Rabi frequency and $\Omega' = \sqrt{\Omega^2 + \delta^2}$). The noise due to this reduced contrast fluctuation is negligible in the EDM measurement.

The vector light shift is produced by residual circular polarized light [21, 22]. This shift is linear in *m*, and is equivalent to an effective magnetic field. The frequency shift of the different Zeeman sublevels is:

$$\Delta\omega_{F=I\pm1/2} = \pm\frac{g_s\mu_B\delta B_{eff}}{2I+1}m = \pm\nu_v(|\varepsilon_L|^2 - |\varepsilon_R|^2)m\cos\theta \qquad (2.\ 25)$$

Where δB_{eff} is the effective magnetic field defined as $\delta\vec{B}_{eff} = B_v(|\varepsilon_L|^2 - |\varepsilon_R|^2)\hat{k}$, ε_L (ε_R) is a vector of left (right) circular polarized light, and θ is the angle between δB_{eff} and the quantization axis. A 10 μK trap depth for the Cs atoms gives $\upsilon_\upsilon \sim 5\times10^3$ Hz [2]. With linearly polarized light (10^{-3} reduction) and Brewster plates in the cavity to filter out circular polarization further (10^{-2} reduction), and $\boldsymbol{\delta B_{eff}}$ (the direction of the trapping beam) perpendicular to the atomic quantization axis (10^{-3} reduction), the vector light shift is very small, less than 2×10^{-4} Hz. The intensity fluctuation between the 2 lattices could possible cause problems, and needs to be less than the shot noise limit. For Cs atoms, it requires the intensity fluctuations between 2 lattices being:

$$\delta\omega = \frac{\delta(I_1 - I_2)}{\langle I\rangle}\times\Delta\omega < 2\pi\cdot\sqrt{2}\cdot 3\times10^{-5} \Rightarrow \frac{\delta(I_1 - I_2)}{\langle I\rangle} < \frac{3\sqrt{2}\times10^{-5}}{2\times10^{-4}} \sim 20\%$$

2.4.4. Noise in the detection system

Because atoms in opposite fields are measured simultaneously, fluctuations in the fluorescent detection laser frequency are common mode. It is straightforward to keep these below 100 kHz to preserve the quality of individual interference fringes. The photodiode array dark current noise is different in the two position measurements and needs to be less than the shot noise per group, which will be discussed in more detail in chapter 4.5

2.5. Systematic errors

Some of the systematic shifts that were important in previous atomic EDM searches, most notably $\boldsymbol{v}\times\boldsymbol{E}/c$ effect induced B field is four orders less than the beam experiment, and perpendicular to the quantization axis (E field defines the quantization axis), which make it negligible. But there are new systematic errors that relate to the 1D lattice trap. We have considered a wide range of potential systematic errors including leakage currents, E field gradients, B field gradients plus imperfection E reversal, and higher order-laser atom interactions. The high voltage power supplies and relays are put far away from the measurement region and maybe even need a shielding to reduce the induced B field due to these electronics. The effect of the hysteresis of the magnetic shielding due to the high voltage charging current is hard to predict and needs to be checked during the measurement.

2.5.1. Leakage current

Leakage currents will induce magnetic field B_{lc} which change sign under E-reversal, and mimic the EDM signal. The energy splitting due to this B field needs to be less than the EDM signal. For Cs atoms, F=3, μg=0.35 MHz/Gauss, it requires $2m_F g\mu_B B_{lc} \le \omega_a$, B_{lc} needs to be less than 0.14 pGauss ($B_{lc} \le 0.03$ pGauss for Rb atoms).

To keep leakage currents away from the atoms, the field plates are 12 inches long, and four spacers are mounted near the edge of the plates. Any current that flows through the spacers is about 12 cm away from the center of the atoms. We also electrically

connect to the high resistance plates at both ends, so the leakage current that flows on the surface of the plates will be suppressed. The leakage current through the spacers is far from the atoms as shown in Figure **2-7**.

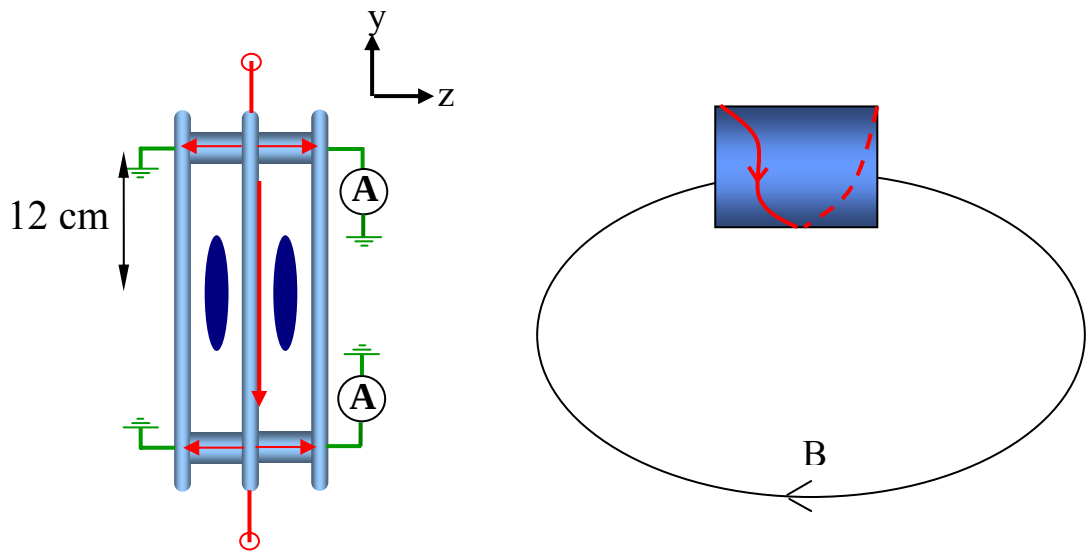

Fig. **2-7**: Leakage current between electrodes

The spacers between the E field plates are made of fused silica, which has very high resistivity, $>10^{18}$ Ωm. The bulk resistance is so large that the steady state leakage current through the spacer depends on the surface resistance. If the current flow straight from one side to another, the effective B field is in the x direction. The worst case is that the current flow on the spacer surface is like the drawing in the Figure **2-7** right. Such a current generates a B field in the z direction. The induced magnetic field due to this current is [23]:

$$B_z = -\frac{1}{l_s}\frac{\partial}{\partial l_s}\left(l_s \cdot \frac{\mu_0 I_s r_s^2}{4 l_s^2}\right) = \frac{\mu_0 I_s r_s^2}{4 l_s^3}, \qquad (2.\ 26)$$

where, r_s is the spacer radius, l_s is the distance between the spacers and the trapped atoms. With 4 spacers on the top and bottom, the corresponding leakage current needs to be less than 1.5 nA for the induced B field to be less than 0.14 pGauss. Any small systematic shift caused by these leakage currents will have a characteristic spatial dependence among the separate groups of atoms in the lattice.

The leakage current flow on the electric field plates can be very close to the atoms (the distance l_p is only about 2 mm). The magnitude of the resulting field is [23]:

$$B = \frac{\mu_0 I_p}{2\pi l_p} \qquad (2.\ 27)$$

One would expect that the z component of the B field is very small. I_p of 0.16 pA will have the B of 0.14 p Gauss. If B_z is 1% of the total field, the current flow on the surface only needs to be less than 16 pA in order for induced B field to be less than 0.14 pGauss. Monitoring the leakage currents of both top and bottom plates can be used to estimate the size of this current. This turns out also to be important for protecting the plates from catastrophic breakdown, since a precursor to breakdown is evident in the leakage current.

2.5.2. Electric field gradient

The experiment is sensitive in a number of indirect ways to time-independent gradients of the B_z component of the magnetic field. For instance, a small inhomogeneous E-field can be created by non-parallel or not-flat electric field plates, or

by patch fields. In E field gradient, atoms will be displaced in the lattice. If the magnitude of the E-field changes upon reversal, the center of the atomic distribution in the trap can thus be changed when the E field is reversed. If there is a B-field gradient, this leads to an E-field sign-dependent B-field, a false EDM signal.

The DC Stark shift due to the static E field is: $\frac{1}{2}\alpha E_s^2$. The force applied on an atom associate with E field gradient is: $F = \nabla U = \alpha E_s \nabla E_s$. The AC Stark shift due to the trapping light is: $U_0 \exp(-2\frac{r^2}{\omega_0^2})$, where r is the distance to the trap center. The atoms displacement can be found from:

$$\nabla U_E = \nabla U_{laser} \Rightarrow \alpha E_s \nabla E_s = \frac{4r}{\omega_0^2} U_0 \exp(-2\frac{r^2}{\omega_0^2}), \qquad (2.28)$$

The YAG laser beam waist ω_0 is 0.63 mm. At E_s = 150 kV/cm, $\nabla E \sim 100 \quad V/cm^2$, U_0 is about 10 μK, the displacement is about 0.01 mm.

If we have a magnetic gradient of 10^{-9} G/cm, to make sure the Zeeman sublevel splitting change less than the experimental sensitivity, the B field variation needs to be less than 0.14 pGauss for Cs. The atoms displacement difference needs to be less than 10^{-4} mm, which requires the E-field reversal to be accurate to within 1%.

2.5.3. Higher order interactions induced light shift

In the presence of a static E field, opposite parity atomic states will be mixed. This allows interactions of the electric-dipole amplitude with the magnetic dipole and electric quadrupole amplitudes driven by the optical field as shown in Figure **2-8**.

(a) (b)

Fig. **2-8**: Higher order laser atom interactions. (ε_s: DC electric dipole; ε^*: AC electric dipole; b: AC magnetic dipole; Q: AC electric quandrupole)

The frequency shift due to the AC magnetic dipole, AC electric dipole and DC electric dipole interaction is [2]:

$$\Delta\omega_{F=I\pm\frac{1}{2}} = \mp[\nu^1_{MD}(\hat{b}\cdot\hat{\sigma})(\hat{\varepsilon}\cdot\hat{\varepsilon}_s) + \nu^2_{MD}(\hat{b}\cdot\hat{\varepsilon}_s)(\hat{\varepsilon}\cdot\hat{\sigma})]m \qquad (2.\ 29)$$

At U = 10 μK, $E_s = 1.5\times10^7$ V/m, Δω is about $2\pi\times0.13$ Hz for Cs atoms.

The frequency shift due to the AC electric quadrupole, AC electric dipole and DC electric dipole interaction is [2]:

$$\Delta\omega_{F=I\pm\frac{1}{2}} = \mp[\nu^1_{EQ}(\hat{b}\cdot\hat{\sigma})(\hat{\varepsilon}\cdot\hat{\varepsilon}_s) + \nu^2_{EQ}(\hat{b}\cdot\hat{\varepsilon}_s)(\hat{\varepsilon}\cdot\hat{\sigma})]m \qquad (2.\ 30)$$

It has about the same magnitude as the frequency shift due to the AC magnetic dipole, AC electric dipole and DC electric dipole interactions. These frequency shifts are proportional to E and m. Since it changes sign upon E reversal, it has the same signature

as an EDM signal, so the value should be less than the experimental sensitivity (3×10^{-7} Hz for Cs atoms).

In our experiment, we set the trapping beam polarization to be parallel or perpendicular to the Es direction. This will reduce the frequency shift by a factor of 10^{-4} if the angle between the E field and light polarization direction (perpendicular direction) is 10^{-4} or less. By a pair of counter-propagating beams, this frequency shift is further reduced, but it needs the beam imbalance to be better than 2.4×10^{-3} for Cs atoms to reach the system sensitivity (0.5×10^{-3} for Rb atoms).

In summary, this chapter introduced our proposed EDM experiment, derived the estimated system sensitivity for EDM measurement, and analyzed the noises and systematic errors due to different sources.

References:

1. H. S. Nataraj, B.K.S., B. P. Das, R. K. Chaudhuri and D. Mukherjee, *The electron electric dipole moment enhancement factors of Rubidium and Caesium atoms.* ArXiv:physics, 2007. **0707**: p. 4086v1.
2. M. V. Romalis, E.N.F., *Zeeman frequency shifts in an optical dipole trap used to search for an electric-dipole moment.* PHYSICAL REVIEW A, 1999. **59**(6): p. 4547.
3. Mosk, S.J., H. Moritz, Th. Elsasser, M. Weidemuller and R. Grimm, *Resonator-Enhanced Optical Dipole Trap for Fermionic Lithium Atoms.* Opt. Lett., 2001. **26**: p. 1837.
4. M. A. Kasevich, E.R., S. Chu, and R. G. DeVoe, *RF spectroscopy in an atomic fountain.* Phys. Rev. Lett., 1989. **63**(6): p. 612-615.

5. Verhaar, M.B.a.B.J., *Role of collisions in the search for an electron electric-dipole moment.* PHYSICAL REVIEW A, 1994. **49**(6): p. R4285.
6. J. P. Carrico, A.A., M. R. Baker, S. Legowski, E. Lipworth, P. G. H. Sandars, T. S. Stein, and M. C. Weisskopf, *Atomic-Beam Resonance Measurement of the Differential Polarizability between Zeeman Substates in the Ground State of the Cesium Atom.* Physics Review, 1968. **170**(1): p. 64.
7. E. Simon, P.L., and A. Clairon, *Measurement of the Stark shift of the Cs hyperfine splitting in an atomic fountain.* Physics Review A, 1998. **57**(1): p. 439.
8. E. D. Commins, S.B.R., D. DeMille, and B. C. Regan, *Improved experimental limit on the electric dipole moment of the electron.* Physics review A, 1994. **50**(4): p. 2960-2977.
9. Ramsey, N., *Molecular Beams*. 1956(1985), Oxford: Oxford University Press.
10. Jacques Vanier, C.A., *The Quantum Physics of Atomic Frequency Standards*. 1989: Institute of Physics Publishing.
11. Loudon, R., *The Quantum Theory of Light*. 2000: Oxford University Press.
12. H. J. Metcalf, P.v.d.S., *Laser Cooling and Trapping*. 1999: Springer.
13. M. E. Gehm, K.M.O.H., T. A. Savard, and J. E. Thomas, *Dynamics of noise-induced heating in atom traps.* PHYSICAL REVIEW A, 1998. **58**(5): p. 3914.
14. J. B. Fixler, G.T.F., J. M. McGuirk, M. A. Kasevich, *Atom Interferometer Measurement of the Newtonian Constant of Gravity.* Science, 2007. **315**: p. 74-77.
15. Lamoreaux, S.K., *Feeble magnetic fields generated by thermal charge fluctuations in extended metallic conductors: Implications for electric-dipole moment experiments.* PHYSICAL REVIEW A, 1999. **60**(2): p. 1717.
16. Poutanen, T.V.a.T., *Magnetic field fluctuations arising from thermal motion of electric charge in conductors.* Journal of Applied Physics, 1984. **55**(11): p. 4015.
17. Jukka Nenonen, J.M., and Toiro Katila, *Thermal noise in biomagnetic measurements.* Rev. Sci. Instrum., 1996. **62**: p. 2397.
18. Romalis, M. 2003 [cited; Available from: www.tip.csiro.au/ISEC2003/talks/hottopic2.PDF.

19. R. A. Hart, X.X., R. Legere, and K. Gibble, *A quantum scattering interferometer.* Nature, 2007. **446**: p. 892-895.

20. C. Chin, V.L., V. Vuletić, A. J. Kerman, and S. Chu, *Measurement of an electron's elecreic dipole moment using Cs atoms trapped in optical lattices.* Physics REVIEW A, 2001. **63**: p. 033401.

21. Mathur, W.H.a.B.S., *Effective Operator Formalism in Optical Pumping.* PHYSICAL REVIEW, 1967. **163**(1): p. 12.

22. B. S. Mathur, H.T., and W. Happer, *Light Shifts in the Alkali Atoms.* PHYSICAL REVIEW, 1968. **171**(1): p. 11.

23. G. L. Pollack, D.R.S., *Electromagnetism*. 2002: Pollack & Stump. 291-296.

Chapter 3

Electric field and magnetic field preparations

In this chapter, the electric field plates design is described and the preliminary testing results for high voltage charging of small ITO coated glass plates and copper plates are given, and the results of background magnetic field measurements are described. The designs of magnetic shielding and cancellation coils are introduced.

3.1. Electric field plates design and test result

The electric field plates are a major component of our EDM experiment. In order to reduce the Johnson noise of electrodes and provide optical access to the measurement region, ITO coated glass plates will be used (as discussed in Chapter 2.4.1). The plates are 12” long to limit the effect of leakage current through spacers. We have the glass plates for final measurement, but they have not yet been coated. All our tests are on 1 inch diameter round copper plates and glass plates coated with ITO. We test the highest voltage which can be applied on the plates, and monitor the leakage current in the steady state and during the charging procedure.

3.1.1. The design of Electric field plates

The electric field plate drawing is shown in the Fig. 3.1.

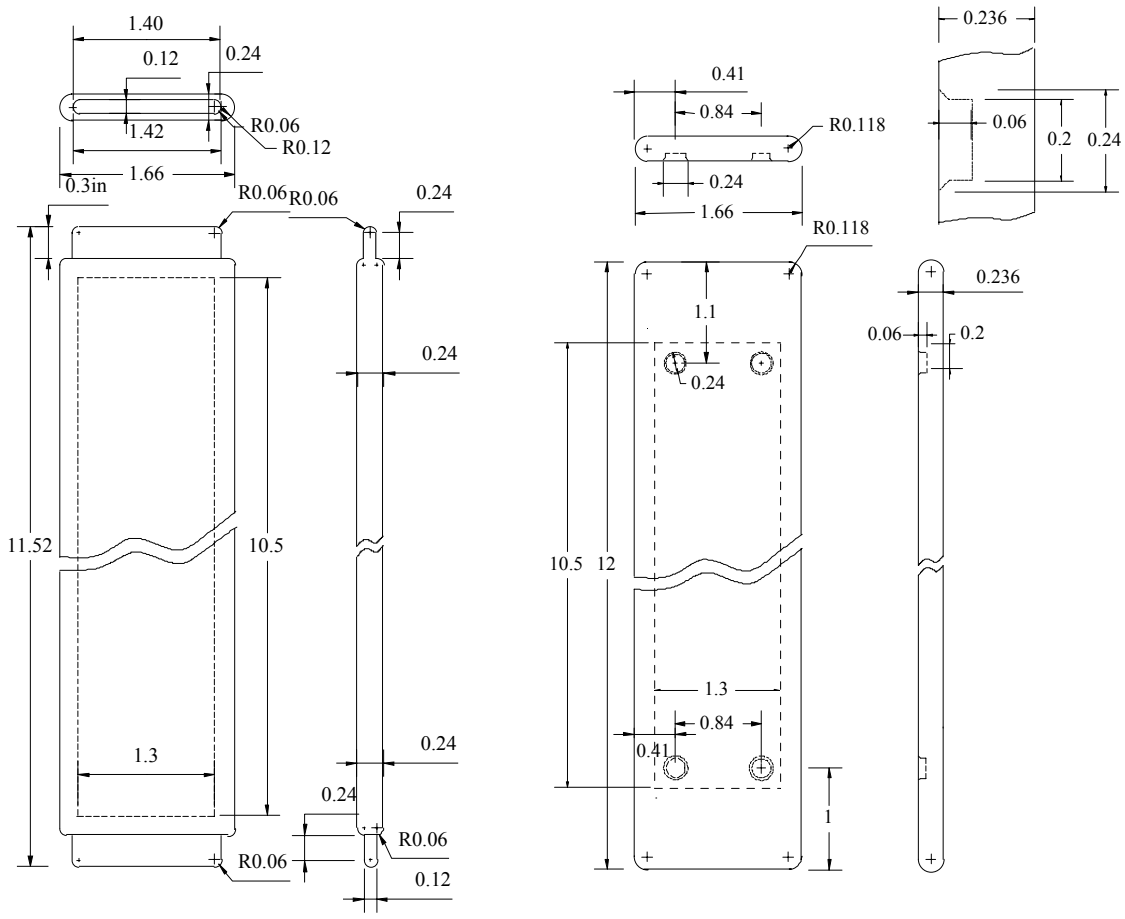

(a)

(b)

Fig. **3-1**: Drawing of the electric field plates (a) Center plate (Plate A). The whole plate will be coated with ITO, HR coating is coated under the ITO for 2 surfaces. (b) Side plates (Plate B, 2 pieces). The area in the dashed line on the surface with blind holes is coated with AR coating. All other areas are coated with ITO coating.

The orientation of these three plates is shown in Figure **3-2**. These three parallel glass electrical field plates with high voltage (switched from positive to negative from shot to shot) on the center piece and ground on the 2 side pieces can provide an E field up to 150 kV/cm. The center plate needs transparent ITO coating around the whole

surface, and high reflection coating under the ITO coating on the two surfaces. The side plates need ITO coating on one surface and all the edges as shown in Figure **3-2**. Four spacers (cut from one piece of 4 mm thick glass) made of fused silica are put between the glass plates to keep the plates parallel. Between two plates, 2 spacers catty cover to each other. The wedge of the center glass plate is less than 20" to keep 2 lattice trap beams parallel to the plates in order to cancel systematic errors induced by higher order laser-atom interactions (as discussed in 2.4.3).

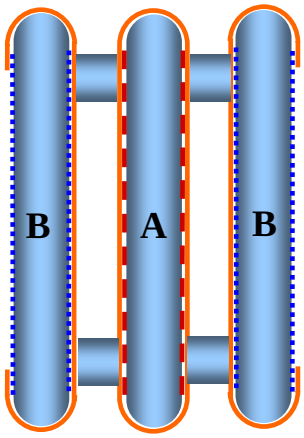

Fig. **3-2**: Coatings for glass field plates. The solid line is the ITO coating, the dashed line is the HR coating, and the dotted line is the AR coating.

We have tested the different shape spacers and found that the leakage current did not depend on the shape of spacers. The final design is cylindrical shape spacers. Due to glass machining issues, it is necessary to have chamfers at the edges to avoid cracks there, which could cause potential problems. We calculate the electric field strengths around plates without spacers and with spacers using Ansoft software. With 4 mm

separation between the plates, and a 60 kV voltage on the center plate, the results are shown in Figure **3-3.**

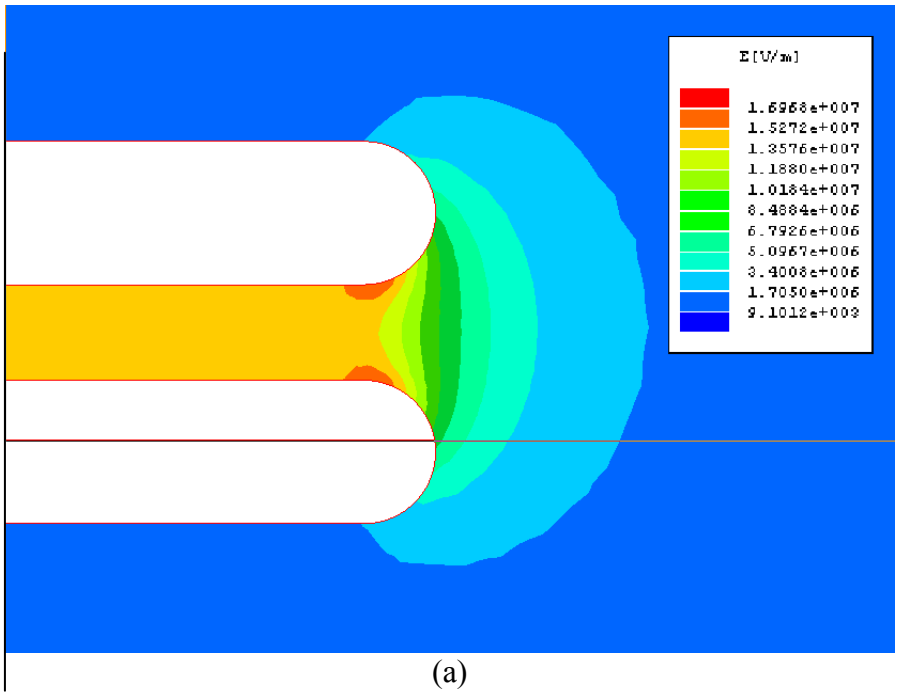

(a)

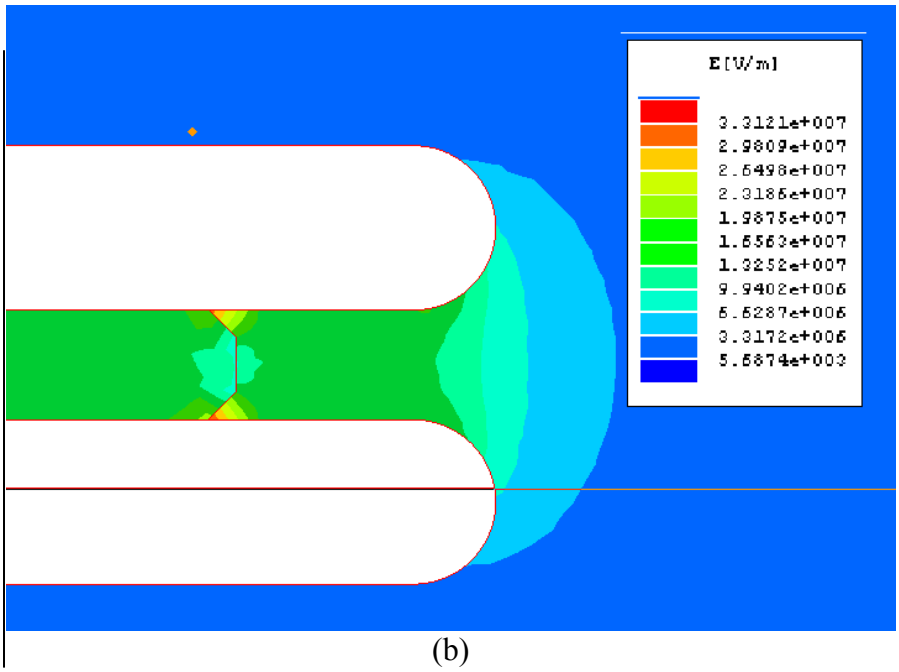

(b)

Fig. **3-3**: Electric field strength between 2 plates. The applied voltage is 60 kV, and the distance between plates is 4 mm. (a) The E strength without spacers. The maximum E is near the edge of plates, and about 1.7×10^7 V/m; (b) The E field strength with a spacer with 45° chamfers. The maximum E near the chamfer is up to 3.3×10^7 V/m.

The E field between the plates is 1.5×10^7 V/cm. The E field strength near the edge is about 1.7×10^7 V/m. With a spacer with a 45° chamfer, the maximum E field strength is about 3.3×10^7 V/m near the edge of the spacer. Changing to a 34° chamfer reduces the maximum E field strength to about 3×10^7 V/m. For real plates, the edge transition between the flat surface and curved edge is not perfectly smooth, which will make the E field higher. The breakdown E field in the vacuum depends on the material and the surface quality. By carefully processing electrodes, a uniform field of 3×10^7 V/m and higher had been reached [1-3]. In our test, the maximum uniform E field we obtained was about 1.67×10^7 V/cm. The real peak E field strength is unclear.

In our experiment, copper and ITO-coated glass plates have been used to test high voltage charging procedure. The plates are assembled in a similar way to we will use in the final EDM measurement. The center piece (copper or glass plates) is connected to high voltage, and 2 side pieces (copper plates) are connected to ground through a picoammeter (Keithley 6485). A precursor to breakdown is evident in the leakage current. Spacers made of fused silica are put between plates. The whole system is put in a vacuum chamber. We monitor breakdowns with a camera. When a breakdown happens, we can see a weak glow near the breakdown place on the monitor. A γ ray detector is used to make sure the dose of γ ray is safe for people. With a 3 mm thick

spacer, the highest voltage we can apply is 50 kV (average E is 1.67×10^7 V/m). Breakdowns happened near the edge of the plates.

3.1.2. High voltage charging and leakage current

The mock-up glass plates were coated by Thin Film Devices. The measured sheet resistance was 100 Ω/sq. At 852 nm, the transmission of the plate was 76%, with reflections of 10%, and 6.7% for the 2 surfaces respectively. The average absorption for one surface is about 3.5%.

a. Steady state leakage current

We measured the leakage current with small copper plates and ITO coated glass plates in a test vacuum chamber. For the copper plates, the surface quality is improved by conditioning the surface with Ar gas at 3.5 mtorr first. The steady leakage current drops a lot after the conditioning as shown in Table **3-1.** With a HV copper plate and a 3 mm fused silica spacer between plates, when the voltage is increased to 35kV, we observe a discharge near the edge of the HV plates. By polishing the edge, we can increase the positive voltage up to 50 kV without discharge. The test vacuum chamber is made of stainless steel. We find asymmetry of the leakage currents for the positive and negative voltage charging. The breakdown voltage during a negative voltage charging is smaller than a positive voltage charging because with negative voltage, electrons are

emitted from the electrode and hit the wall of the chamber. The positive ions generated from the chamber through this electron desorption process, provide an additional source and increase the leakage current [4]. By adding a quartz tube inside the vacuum around the high voltage system, the leakage current at negative voltage drops, but it is still not as good as the positive voltage. Table **3-1** gives the measured steady state leakage currents for the copper plates and the ITO-coated glass plates at different negative voltages.

Table **3-1**: Steady state leakage current under negative voltage, the separation between the plates is 3 mm.

Voltage	-18kV	-20kV	-25kV	-30kV
Copper Plate (Before Ar c.)		-10nA	-80nA	
Copper (Ar condition)			-100pA	-1nA
Copper w/ quartz tube	0pA	-0.3pA	-2pA	-10pA
ITO Plate	-500pA	-2nA		

From Table **3-1** we can clearly see the effect of the quartz tube. The leakage current drops from 100 pA to only 2 pA at 25 kV by adding the quartz tube. At –36 kV (120 kV/cm), the current is stabilized to –17 pA after 5 minutes. Table **3-2** gives the results for positive voltages.

Table **3-2**: Steady state leakage current for glass plates and copper plates under positive voltage. (The separation between the plates is 3 mm)

Voltage(kV)	20	30	40	45	46	48	50
Current(pA) (Glass)	2	8	4	5		50	260
Current(pA) (copper)	2.0	2.5	7	35	18		

The positive voltage results are still better than the negative voltage results. At 40 kV, the leakage is less than 10 pA. The leakage current also fluctuates. At -36kV, the leakage current range is from -26 pA to -12 pA.

b. High voltage charging time constant

We have measured the charging time constant for the copper plates and the ITO-coated glass plates. The cable we are using has capacitance of 29.8 pf/feet. Our cable is about 12 m long, so its total capacitance is about 1.2 *nf*. The capacitance of the plates can be obtained by $c_p = \frac{\varepsilon_0 A_p}{d_p}$, where A_p is the area of the plates, d_p is the distance between plates. The spacer used here is 6 mm thick. The capacitance of the plates is about 1.3 *pf*, much less than the cable capacitance. On short time scales, the leakage current is measured with Tektronix TDS3014B Oscilloscope, which displays the analog output of the picoammeter at the 200 nA range. A reading of 1V on the oscilloscope corresponds to a leakage current of 100 nA. The charging time constant can also be measured by monitoring on an oscilloscope the 'I-monitor' (current monitor) on the HV power supply rear panel. The time constant τ can be found by fitting the data

into equation: $I_i = I_{0i} e^{-\frac{t}{\tau_i}}$. Figure **3-4** gives the leakage current vs. the charging time for a copper plate.

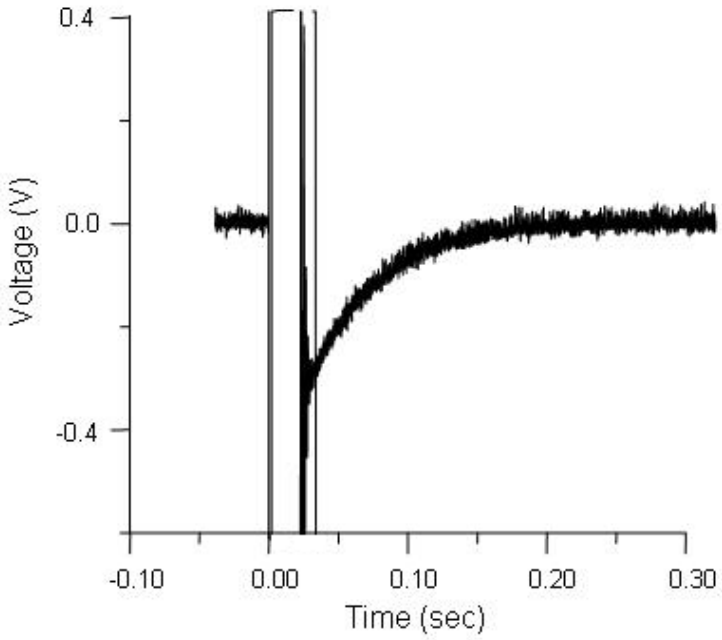

(a)

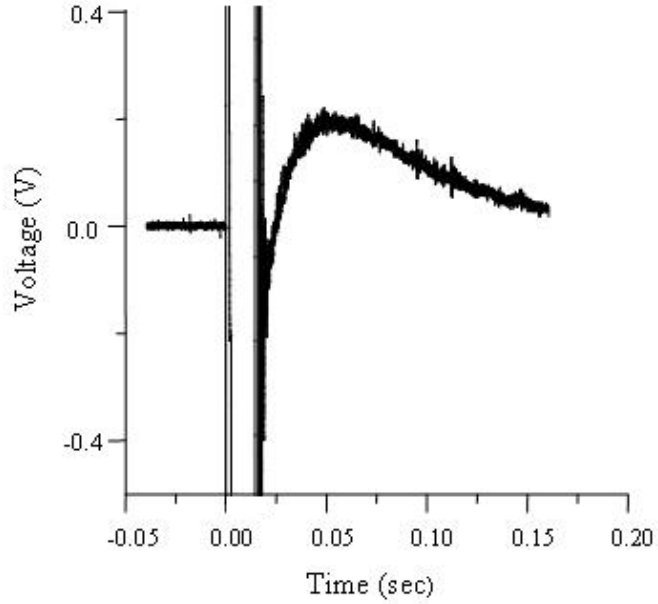

(b)

Fig. **3-4**: The leakage current vs. the charging time (100 nA per volt). Just after charging, the current is oscillating and the magnitude is so large that it is out of the ranging showing in the figure. (a) Charging from 0 to -35 kV, τ is 50 ms after the first 20 ms large oscillation; (b) Charging from 0 to 42 kV, τ is 200 ms.

For the copper plates, the time constants are different for different applied voltages. At ±5 kV, the time constant is 200 μs; while at ±30 kV, the leakage current oscillates during the first 20 ms, and then decays with a time-constant of about 50 ms. The time constant increases to 200 ms when charging to 42 kV. For charging to 30 kV, the peak current I_0 is 200 nA. On long time scales, the leakage current is measured by a computer read directly from the PicroAmmeter through RS 232 interface. The time resolution of the measurement system is 0.5 seconds. With a time constant of 50 ms, it takes 2 seconds for the leakage current drops to 10 pA. This agrees well with the data taken by the computer 2 seconds after charging.

The current oscillations at the first 20 ms tended to freeze the computer control system, requiring a reboot. Adding a 20 MΩ resistor in the system to reduce the oscillation dramatically improved things. The high voltage charging with this current-limit resistor in the circuit is measured. The spacer used here is fused silica cylinder with D = 0.5 in, L = 0.25 in. The plates are copper plates. Figure **3-5** shows the charging and discharging results. The applied voltage is +20 kV. The time constant is about 20 ms in both charging and discharging procedures. From the figure, we can clearly see that the oscillations at the beginning of the charging procedure are gone.

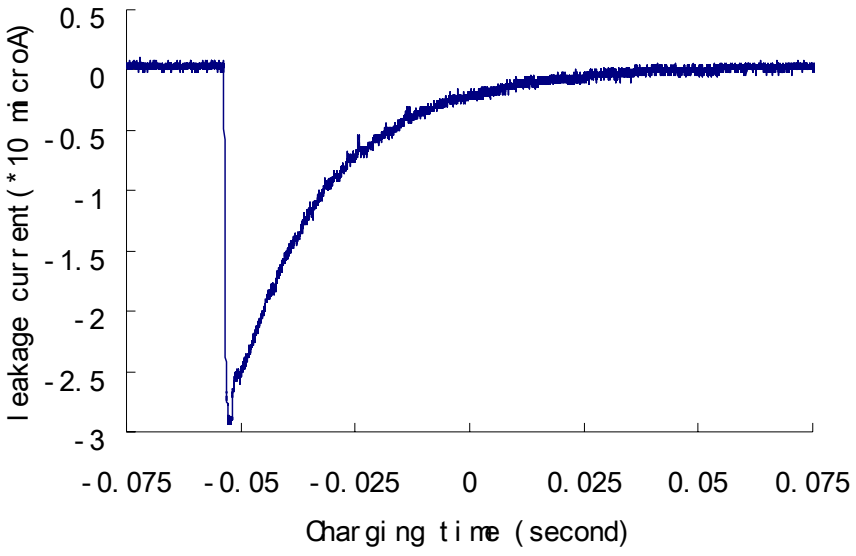

(a)

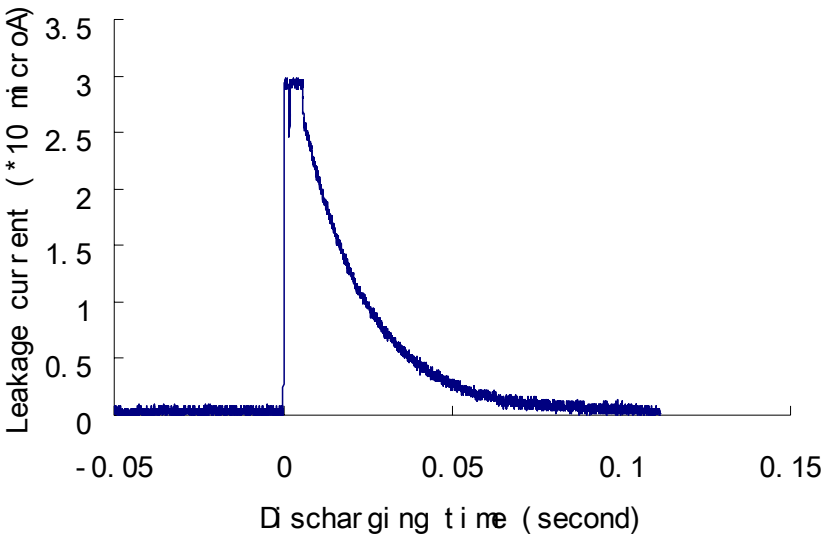

(b)

Fig. **3-5**: Leakage current vs. the charging time. The applied voltage is +20 kV (a) Charging procedure. The time constant is 20.4 ms (b) Discharging procedure. The time constant is 19.3 ms.

We also tested the charging of ITO-coated glass plates. Charging proceeds differently from metal plates. There are two current decay time constants. In the short time range, the positive charging time-constant is about 50 ms, and the negative charging time-constant is about 60 ms. Figure **3-6** shows the positive charging procedure from 0 to 25 kV.

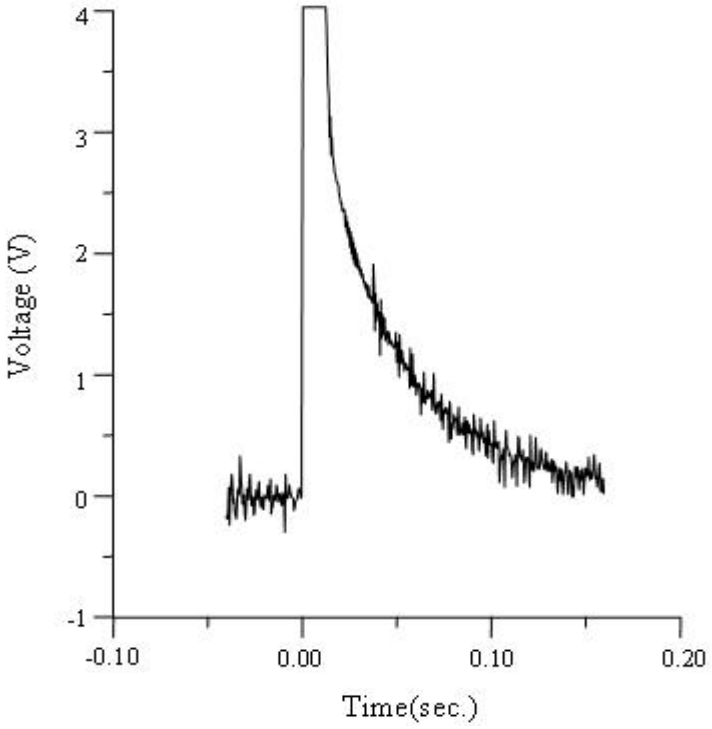

Fig. **3-6**: The current from the high voltage power supply vs. the time. The y unit is in voltage with 10 volts corresponding to 1.5 mA. The voltage switch from 0 to 25kV. The fit time constant is 48 ms.

At long times, the leakage current is monitored using a computer for more than 10 seconds. The results of the two charge procedures (0 → positive voltage, and 0 → negative voltage) are plotted together in Figure **3-7**. The red, blue and pink curves are for positive voltage charging, and the black and red circle ones curves are for negative voltage charging. It clearly shows that besides a short term time constant, there is also a long term time constant for the ITO coated glass. It is about 1 s for the negative voltage charging, and about 2 s for the positive voltage charging.

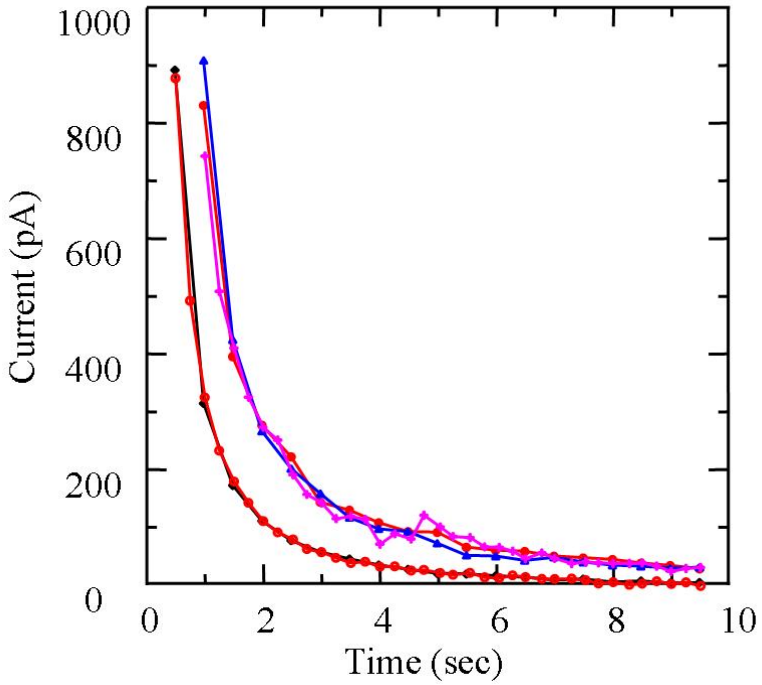

Fig. **3-7**: Leakage current vs. charging time for ITO coated glass. Red, blue and pink ones are positive voltage and black and red circle ones are negative voltage.

We also test the high voltage switching using timing like what we expect to use in the final EDM measurement. The plate is connected to the high voltage for 10 seconds, and then to ground for 5 seconds, and then to negative voltage for another 10 seconds, and then to group (+34kV, 0, –34kV, 0) with a repetition period of 30 seconds. Switching is controlled by 2 signals from the timing board (voltage polarity control and voltage on/off control). The data are recorded for 20 periods. Figure **3-8** shows one period from 100 second to 140 second.

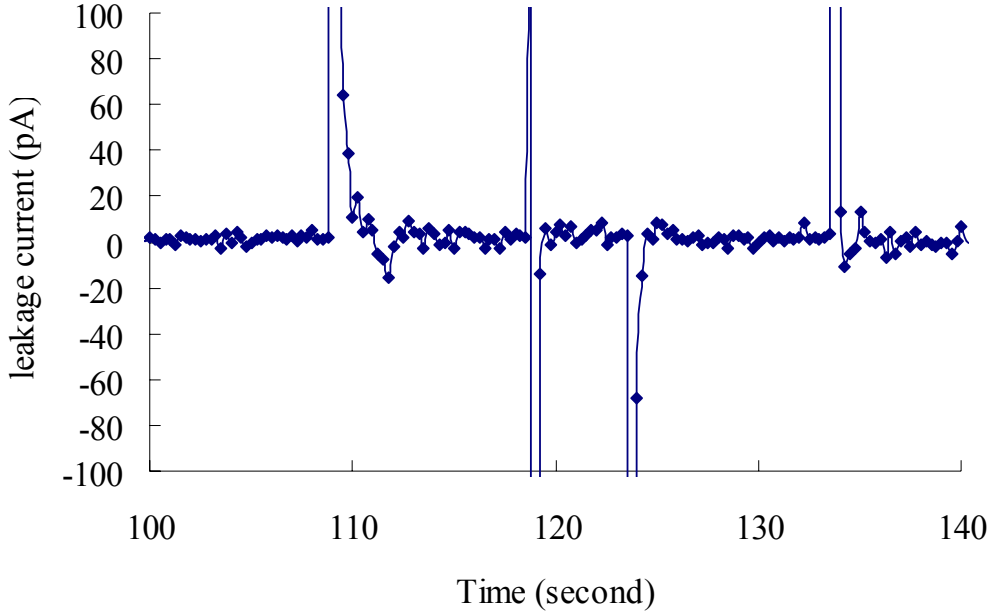

Fig. **3-8**: Leakage current vs. the time during the voltage switching. The voltage was switched from ground to positive, stayed 10 seconds, switched to ground, stayed 5 seconds, switched to negative, stayed 10 seconds, switched to ground again. The first peak is the positive charging, the second one is the positive discharging, the third one is the negative charging, and the fourth one is the negative discharging.

In our EDM experiment, the measurement chamber is made of fused quartz. Our tests using a silica shielding tube suggest we might be able to make negative charging as good as positive charging. The highest voltage that can be applied on the electrodes will depend on either the spacer structure or the glass plate edge smoothness. We do not fully understand the long charging time constant for the ITO coated glass plates. It could be due to pinholes on the ITO coating which might need a really long time to be fully charged. For the positive charging, the leakage current is about 800 pA after 1 second.

3.2. Background magnetic fields and cancellation

We examine the background magnetic field and field fluctuations due to different sources. To get smaller residual magnetic field near the measurement region, the magnetic fields are cancelled by 3 sets of coils outside the magnetic shielding.

3.2.1. Environment B field and field gradient fluctuations

We monitor the B field and field gradient with magnetic sensors (Applied Physics System). The results show that during the daytime, the peak to peak B fluctuations are about 1 mGauss, while they are much smaller at night, usually less than 0.1 mGauss. The field gradient fluctuation $\delta\nabla_x B_z$ is 7.1 μG/cm/√Hz. The elevator operation induced B field change is about 0.5 mGauss. With the Zeeman slower field on (70A) and off, the B field changes by 6.38 mGauss (z-axis), 39.85 mGauss (x-axis), 3.65 mGauss (y axis). There is a large 60 Hz B field noise, with a peak to peak level of about 550 μGauss. Two ion pumps (Varian 500 and Varian 55) contribute to a noise of 50 μGauss at this frequency (presumably due to the power supplies), the lights contribute to a noise of 160 μGauss at this frequency, and other power supplies contribute to a noise of 50 μGauss at this frequency. After we turn off all these sources, there is a noise of 400 μGauss at 60 Hz.

3.2.2. Background magnetic field cancellation coils design

The B field at the measurement region is B_x = 90 mGauss, B_y = 350 mGauss, B_z = 30 mGauss. This field needs to be cancelled first by 3 sets of coils and then shielded. Given the magnetic shielding size, the shape of coils used here are rectangular, and the size is shown in Figure **3-9**. Besides the Helmholtz-like coils to cancel the B field, we also have anti-Helmholtz coils (2 coils separated by the distance of coils size and have opposite current direction) to cancel the B gradient. (They have been setup, but have never been used.)

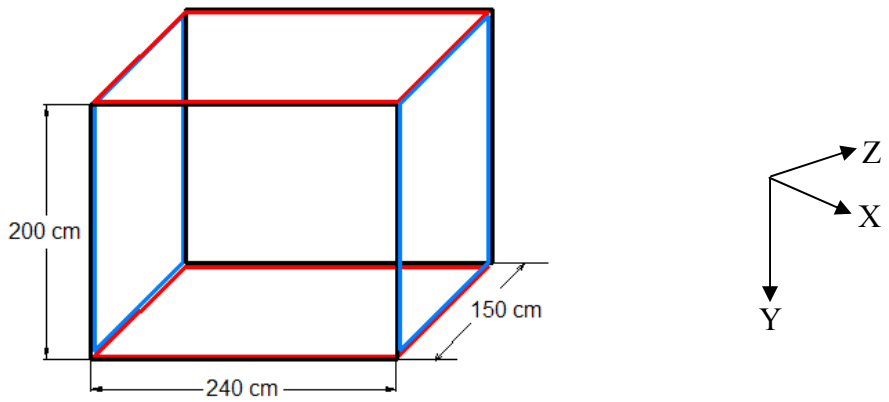

Fig. **3-9**: B cancellation coils. The red coils (By') can cancel By, the blue (Bx') and black (Bz') together cancel Bx and Bz. The right coordinates shows the real EDM experimental coordinates.

The wires we used here are AWG hook-up wire with a diameter 4.11 mm, and resistivity of 1.28 Ω/km. We have 44 turns of By' coils for the bias field and 24 turns for

the gradient; 30 turns of Bx' coils for the bias field and 22 turns for the gradient; 10 turns of Bz' coils for the bias field and 20 turns for the gradient. The power supplies for these coils are Agilent E3614A and Agilent E3610A.

With the cancellation coil set to zero the B field in the measurement center, there are still residual magnetic fields away from the center. We measured the original magnetic fields and the fields after the cancellation. At the center of the EDM measurement region, the original B field is (+0.09292, -0.34909, -0.02023) Gauss, by applying current Iy'=3.58 Amp, Ix'=1.99 Amp, Iz'=1.06 Amp on the cancellation coils, the B field become (+0.00274, -0.00347, +0.00393) Gauss. The results are shown in Figure **3-10.** The field changing in one direction (x, y or z) both before and after the cancellation is shown in one figure. For convenience of comparison, the data is displayed as B field minus an offset, which is set to make the center to be zero. The largest field gradient left is dB_y/dz. Because the second derivative is not zero, it cannot be cancelled along the whole distance. The magnitude of the gradient near the center is about 0.5 mG/cm

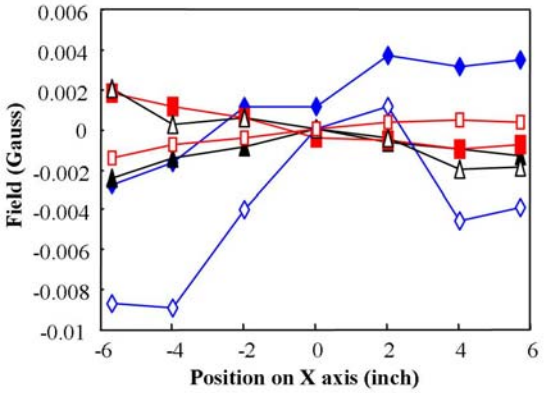

(a)

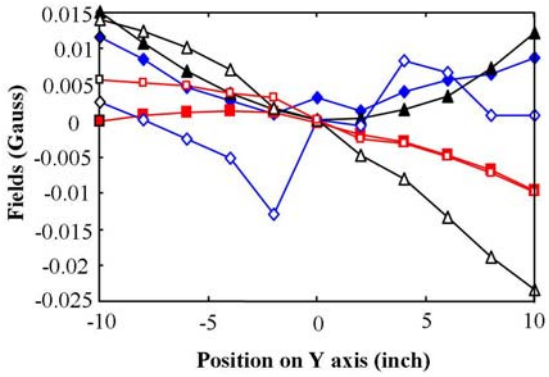

(b)

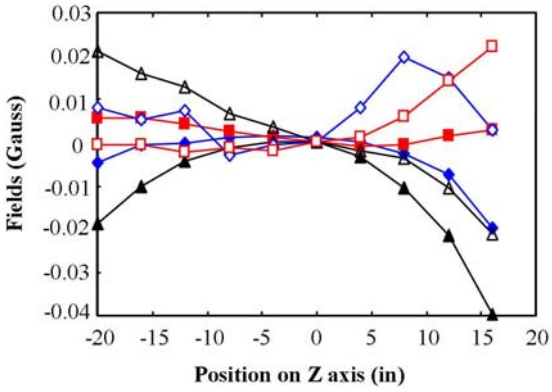

(c)

Fig. **3-10**: The magnetic field before and after the cancellation. (a) B field change along the x direction, (b) B field change along the y direction, (c) B field change along the z direction. Before: Unfilled dots; after: Solid dots. Bx(Blue), By(Black), Bz(Red)

3.3. Magnetic shielding

The magnetic shielding will use ferromagnetic materials which act like magnetic flux conductors to attract the field flux and deflect it away from the region to be shielded. Generally, a shielding factor is determined by the shield geometry and magnetic properties [5].

For an infinite long cylindrical shell with its axis transverse to the field, the shielding factor is [6]:

$$S_T = \frac{B_i}{B_0} = \frac{\mu t_{sh}}{2R_{sh}} \qquad (3.\ 1)$$

Where B_0 is the B field before introducing the shielding, B_i is the field inside the shielding, t_{sh} is the thickness of the shielding material, and R_{sh} is the radius of the shielding. The shielding factor in the axial direction is a more complicated problem.

Holes in a shielding are always necessary for optical access and vacuum pump connections. For a hole with a radius r_h in a shielding with a radius of $R_{sh} >> r_h$, the field inside the hole falls off as [7],

$$B(h) = B_{ext} e^{-k_s h / r_h} \qquad (3.\ 2)$$

where h is the distance from the hole and k_s is a constant about 1.5. Holes degrade the shielding factor only slightly (drops a few tens percent for the B field and B Field gradient) [8, 9].

To get a large shielding factor, multiple layers of shielding usually are used. The net shielding factor is not simply a product of individual factors because the presence of

the internal shield affects the internal boundary conditions. The transverse shielding factor is:

$$S_T = S_T^n \prod_{i=1}^{n-1} S_T^i \left[1 - \left(\frac{R_i}{R_{i+1}} \right)^2 \right] \qquad (3.3)$$

The structure of the 4 layers shielding we designed is shown in the Figure **3-11**.

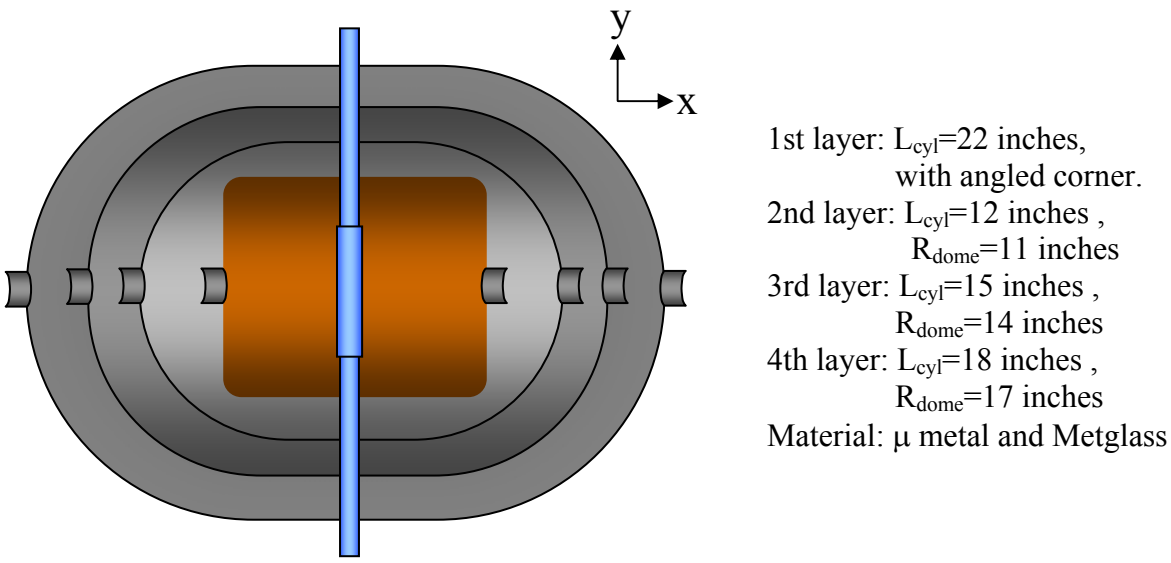

Fig. **3-11**: Structure of 4 layers magnetic shielding. The innermost layer material is metglas. The other 3 layer's shielding material are μ metal. There are 2 holes in the axial direction for the fibers and cables feed through. There are 2 holes 3 inches in the radial direction for the vacuum glass tube. And one layer made of 2 parts to assemble together plus 2 caps in the end.

For the first layer, we will use Metglas an amorphous cobalt-based alloy. It is suitable for making flexible electromagnetic shielding, magnetic sensors and high

frequency cores. The metglas we will use is 2” width and 22 micron thick. We will wrap the tape on a 24” long, 16” diameter plastic cylinder. The permeability after annealing will be improved by one order of magnitude over the As Cast (unannealed) one. But annealing will change its physical properties making it more fragile. The 6 mm μ-metal will be used in the other three layers materials.

There are two holes in the axial direction for the fibers and cables feed-through, and two holes in the radial direction for the vacuum glass tube. Each layer is made with two separate parts so that they can be assembled around the vacuum system, and has 2 caps at the two ends. The shielding factor is calculated by the Ansoft program. Because of the shielding symmetry, we use 2D calculations. The initial B field is produced by a pair of coils at (R = 40”, Z = ±25”, I = ±1 Amp), and the result is shown in the Figure **3-12** (a). Using a 4-layer magnetic shielding as we designed, the residual B field and field gradient are obtained by Ansoft software also, and shown in the Figure **3-12** (b).

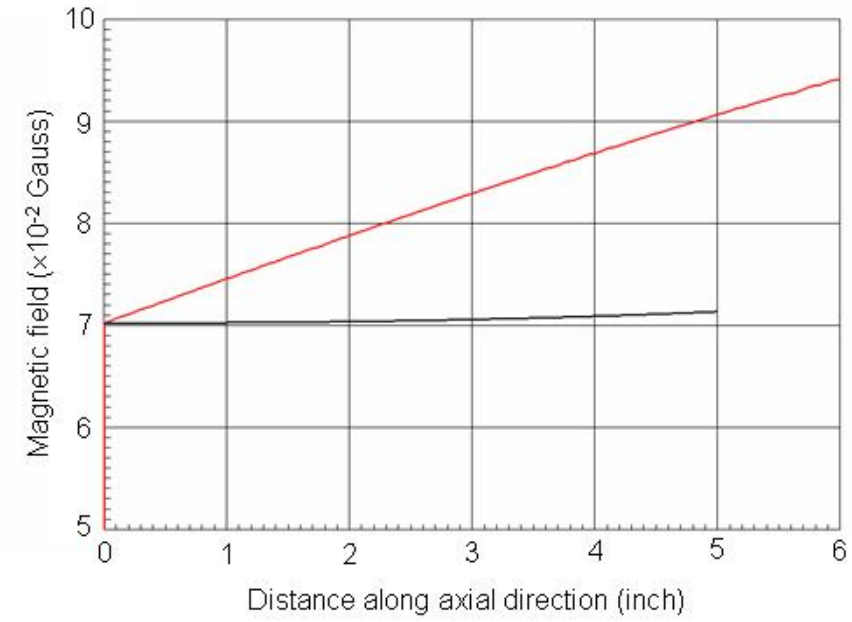

(a)

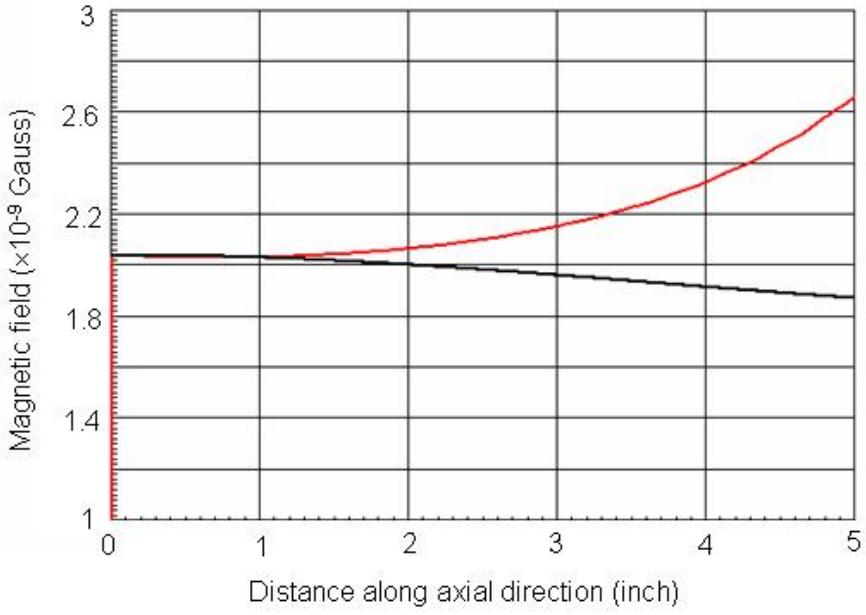

(b)

Fig. **3-12**: B field magnitude vs. the distance. (a) The initial B field under a pair of coils at (R = 40", Z = ±25", I = ±1 Amp). X is the along axial direction,Red curve is the B field and the black curve is the field gradient. (b) The residue B field with 4 layers of magnetic shielding. Red curve is the B field and the black curve is the field gradient.

The shielding factors of the B field and B field gradient obtained from the above results are:

$$S_A(B) = \frac{1.4\times10^{-5}}{2\times10^{-13}} = 7\times10^{7}$$

$$S_A(\nabla B) = \frac{0.36\times10^{-5}/2"}{0.5\times10^{-14}/2"} = 7\times10^{8}$$

With a series of concentric holes in a multilayer shield, which can be modeled as the decay of field in a pipe, as described in references[10, 11], shielding factors are reduced. The actual residual B-fields will depend on the shielding material and can be reasonably controlled down to a few μGauss level.

3.4. Magnetic field cancellation inside the shielding

The residual magnetic fields inside the shielding will be measured with Zeeman spectroscopy. Because there are two spatial arrays of independent groups of trapped atoms, field gradient in the y and z direction can also be obtained. The B_z gradient in the x direction (dB_z/dx) can be obtained by measuring dB_x/dz ($\nabla \times B = 0 \Rightarrow \frac{\partial B_z}{\partial x} = \frac{\partial B_x}{\partial z}$). Measured fields and field gradients can be cancelled using coils inside the magnetic shielding.

The surrounding magnetic shielding has a significant effect on the shape and the magnitude of the field generated by coils [12, 13]. The field strength is reduced because the shield generates an opposing magnetic field to keep the total flux through the shield

zero. The homogeneity is improved by the cylindrical wall of the shield because of the flattening of the field lines at this boundary. In the x direction (the axial direction of the cylindrical shielding), Helmholtz-like coils can be used to generate the uniform B field to cancel the residual field, while in the y and z directions (the radial direction of the cylindrical shielding), it is a much more complicated calculation [14].

3.4.1. Coils to cancel B field in axial direction

Helmholtz coils are widely used for generating uniform magnetic fields. However, if Helmholtz coils are used inside a ferromagnetic shield, the uniform magnetic field generated by the coils is disturbed because of the influence of the ferromagnetic shield. For a circular coil inside an infinitely long shielding with the infinite permeability, the magnetic field along the x axis (axial direction inside the shielding) is given by [14]:

$$H(x) = \frac{I_x}{R_0} \sum_{k=1}^{\infty} \frac{e^{-j_{0,k}|x|}}{J_1(j_{0,k})} = \frac{I_x}{R_0} \int_{-\infty}^{+\infty} \frac{e^{it|x|}}{2\pi I_{0x}(t)} dt \qquad (3.\ 4)$$

where I_{0x} is a modified Bessel function defined by $I_0(x) = J_0(ix)$, R_0 is the radius of the coil, x is the distance from the center of the coil to the measurement point in axial direction. The numerical result is shown in Figure **3-13.**

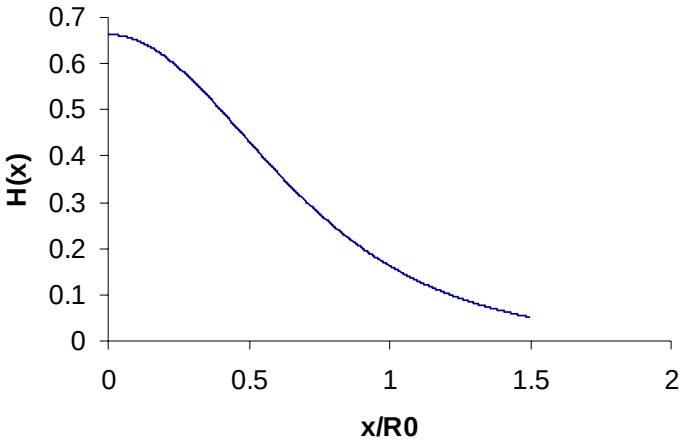

(a)

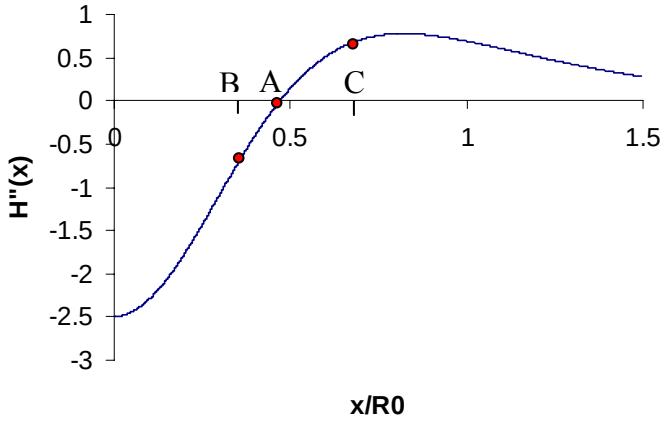

(b)

Fig. **3-13**: The magnetic field generated by a coil inside a cylindrical magnetic shielding (a)the magnitude of the field (b) The second derivative of the field

To get a uniform field at a given position, the field first and second derivatives need to be zero. At the center of a pair of coils which have the same current, the first derivatives are cancelled. The second derivatives have the same sign. To get the field second derivative to be zero, for one pair of coils, x0 = 0.4706 R_0 (different from the Helmholtz condition x=0.5R). To use multiple pairs of coils, they must be to added in 2

pairs, as shown in the Figure **3-13** (b) B and C points. The sum of the second derivative is zero (H"(B)+H"(C)=0).

In our design, a set of 3 pairs (±0.3467R0, ±0.4706R0, ±0.75R0R0) of coils are calculated to produced the uniform B field in the x direction. The B field is calculated by Ansoft Maxwell software. By assuming the applied current in each coil is 1 Amp. The field magnitude is shown in Figure **3-14.**

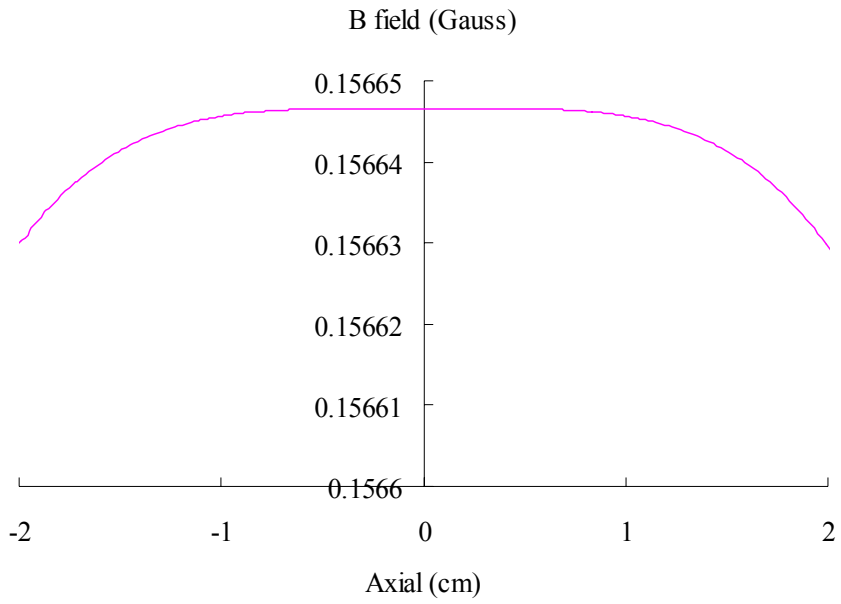

Fig. **3-14**: B field generated by 3 pairs of coils inside cylindrical shape magnetic shielding. The 3 pair at the position (±0.3467R0, ±0.4706R0, ±0.75R0R0), R0=8 inch, the current applied on each coil is set to be 1 Amp.

The B field is very uniform near the center region, the magnitude is 0.1566 Gauss under 1 Amp current. From the center to 5 mm away, the field only drops by 20 nGauss, which is about 1.3×10^{-7} of the field strength.

3.4.2. Coils to cancel B field in radial direction

In the radial directions (y and z directions), 2n coils provide B fields in the y or z directions. To get a uniform magnetic field, the angle θ, the angle between the coils and the x-axis, need to be set as [14]:

$$\theta = \pm \arcsin\left(\frac{2m-1}{2n}\right), \quad (\text{m}= 1,2,...\text{n}). \qquad (3.\ 5)$$

The Figure **3-15** shows the coil positions in the xy plane to provide the uniform B field in the y direction.

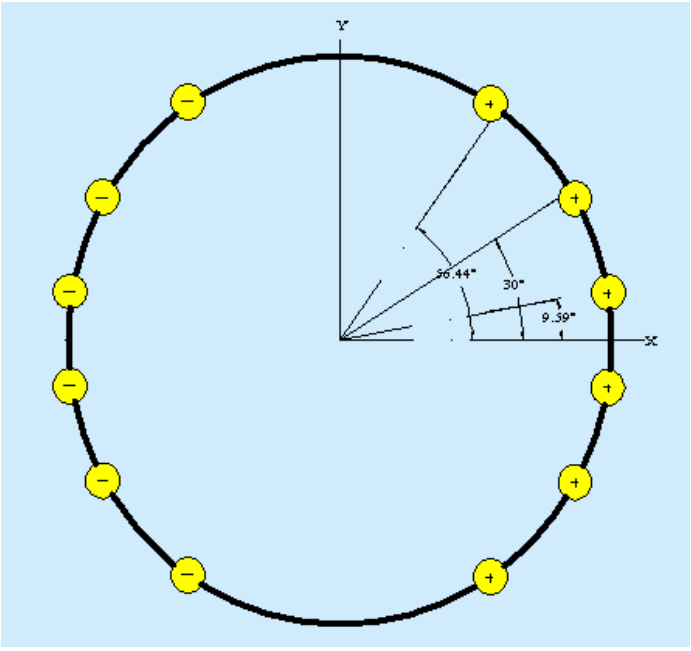

Fig. **3-15**: Coils position in the xy interface to provide the uniform B field in the y direction. Pairs of sources on the left and right portion of the picture are part of the same loop in the coil. Coil segments parallel to x axis are connected by straight lines on the bottom and semicircular coils at the top of the shield.

Because these coils are inside the magnetic shielding, it is very important that the B fields they provide are very stable, which requires low noise current power supplies. Also, these coils must not only provide the bias B fields, which needs to be very small and quiet, they are also used to provide B field to define the quantization axis during the optical pumping. The B field magnitude is about 100 mGauss level.

The coils can be shared to provide 2 different level B fields. The power supplies cannot be shared. We plan to use Pulse Instruments PI41702 four channel low noises DC bias card as the power supply for stable current source. The computer controlled coils' power supply is shown in Appendix F.

References:

1. Schumann U, G.S., Kurrat M, *Breakdown voltage of electrode arrangements in vacuum circuit breakers.* IEEE TRANSACTIONS ON DIELECTRICS AND ELECTRICAL INSULATION, 2003. **10**(4): p. 557.
2. A. V. Batrakov, D.S.N., G. E. Ozur, S. A. Popov, D. I. Proskurovsky, V. P. Rotshtein. *Increasing the electric strength of vacuum insulation by treatingthe electrodes with a low-energy, high-current electron beam*. in *Discharges and Electrical Insulation in Vacuum, Proceedings. ISDEIV., XVIIth International Symposium*. 1996.
3. Noer, R.J., Applied Physics A, 1982. **1**: p. bf28.

4. Latham, R.V., *High Voltage vacuum insulation: the physics basis*. 1981: Academic Press. 23.
5. Rikitake, T., *Magnetic and Electromagnetic Shielding*. 1987: Springer.
6. T J Sumner, J.M.P., K F Smith, *Convectional magnetic shielding.* J. Phyisics D: Applied Physics, 1987. **20**(9): p. 1095.
7. I. B. Khriplovich, S.K.L., *CP violation without strangeness, electric dipole moment of particles, atoms, and molecules*. 1997: Springer. 37.
8. Rikitake, T., *Magnetic shielding by a spherical shell having a hole.* Journal of Geomagnetism and Geoelectricity, 1990. **42**(10): p. 1221-1235.
9. Ekstrom, E.A.B.a.C.R., *Optimal three-layer cylindrical magnetic shield sets for scientific applications.* Rev. Sci. Instrum., 2002. **73**: p. 2699.
10. Thorp, S.M.F.a.T.L., *Shielding of Low Magnetic Fields with Multiple Cylindrical Shells.* Rev. Sci. Instrum., 1971. **42**(10): p. 1411.
11. Mager, A., *Magnetic shields.* IEEE TRANSACTIONS ON MAGNETICS, 1970. **6**(1): p. 67.
12. Rigby, K.W., *Design of magnets inside cylindrical superconducting shields.* Rev. Sci. Instrum., 1988. **59**(1): p. 156.
13. Pipkin, R.J.H.a.F.M., *Magnetically Shielded Solenoid with Field of High Homogeneity.* Rev. Sci. Instrum., 1965. **36**(2): p. 179.
14. Mutsumi Hosoya, E.G., *Coils for generating uniform fields in a cylindrical ferromagnetic shield.* Rev. Sci. Instrum., 1991. **62**(10): p. 2472.

Chapter 4

Experimental setup

In this chapter, the experimental setup is described in detail including the vacuum system, the laser systems for the MOT, molasses cooling and launching, cavity enhanced far-off-resonance 1D lattice, computer-controlled system and detection system.

4.1. Introduction

The experiment is performed in 3 connected vacuum chambers: oven chamber, main chamber and measurement chamber. The atoms from reservoirs in the oven chamber are first slowed down in a one-meter long Zeeman slower, and then loaded into the MOT in the main chamber. After loading, the B-field is adjusted by changing the MOT B-field and cancellation coils settings to move atoms so that they overlap with the YAG 1D lattice traps. The MOT cooling beams are also used as the optical molasses (OM) beams after MOT B-field is shut off. By changing the relative frequencies of OM beams to make a moving frame, the atoms can gain a selected velocity and be launched up to the measurement chamber while guided by the 1D optical lattice traps. The atoms are stopped and cooled by another 3 pairs of optical molasses beams when they reach the center of the measurement chamber, so that they are again trapped by the 1D lattice.

4.2. Vacuum chamber

The system includes 3 vacuum chambers pumped by 4 ion pumps (Varian 55, Varian 500, and two Thermionics PS100) and 2 Titanium sublimation pumps (TSP). The oven chamber has a relatively high pressure about 3×10^{-9} torr. The hot atoms are collimated by a glass capillary array (the nozzle) and then go through the Zeeman slower. The nozzle's temperature always needs to be higher than the other parts to make sure the atoms will not stick on the nozzle surface and block it. The main chamber is made of stainless steel with vacuum windows and current feedthroughs for the MOT coils. The pressure was 3×10^{-10} torr just after baking. The measurement chamber is a 1 m long glass chamber above the main chamber. The glass chamber has a 2.35 inch diameter and its center part is a 20 cm long and 3×3 inch wide square tube as shown in Figure 4.1**.** The square tube is the measurement region and has AR coating on its outer surfaces. The two flanges on the ends of the glass chamber are modified from commercial flanges for mounting of the electric field plates.

The glass chamber was baked to 130℃. The pressure was 8×10^{-10} torr after baking. The temperature increase rate used in baking is about 10℃/hour. (Baking at a higher temperature might be needed to get a better vacuum. The glass chamber and all the other electric field system parts could be baked to a high temperature (200 ℃) before they are assembled to the vacuum system to help reach a better vacuum.)

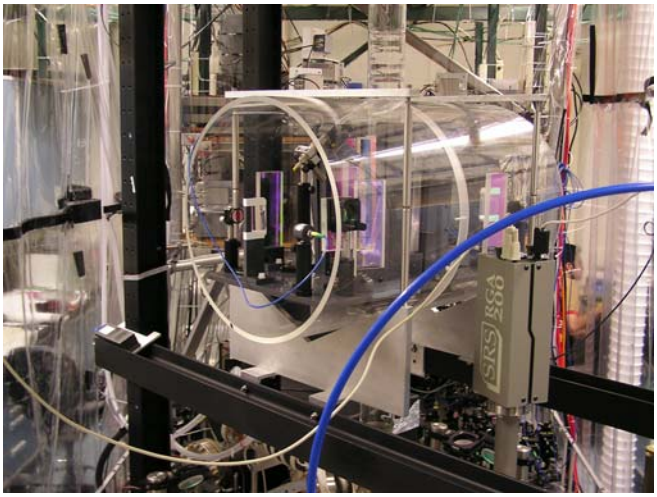

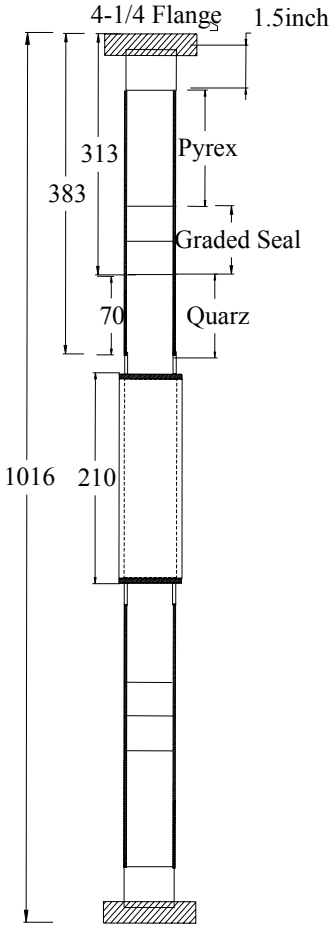

* Min ID of tube is 2.35 Inch (60m

Fig. **4-1**: Glass vacuum chamber. On the left is the real glass chamber assembled in the system. The big plastic cylinder is used to wrap the Metglass tape as the first layer of magnetic shielding. The optics in it are for the top transverse cooling and detections. The glass chamber is about 1 meter long with the center part being a 76×76×210 (mm) square tube as the measurement region. The square tube is made of fused quartz and AR coated on the surfaces.

Two six-way crosses are used in the system. One is between the MOT chamber and the glass chamber to provide high voltage feedthrough and vacuum pumps. The other is set above the glass chamber also for the high voltage (HV) feedthrough and pumps, as shown in Figure **4-2.**

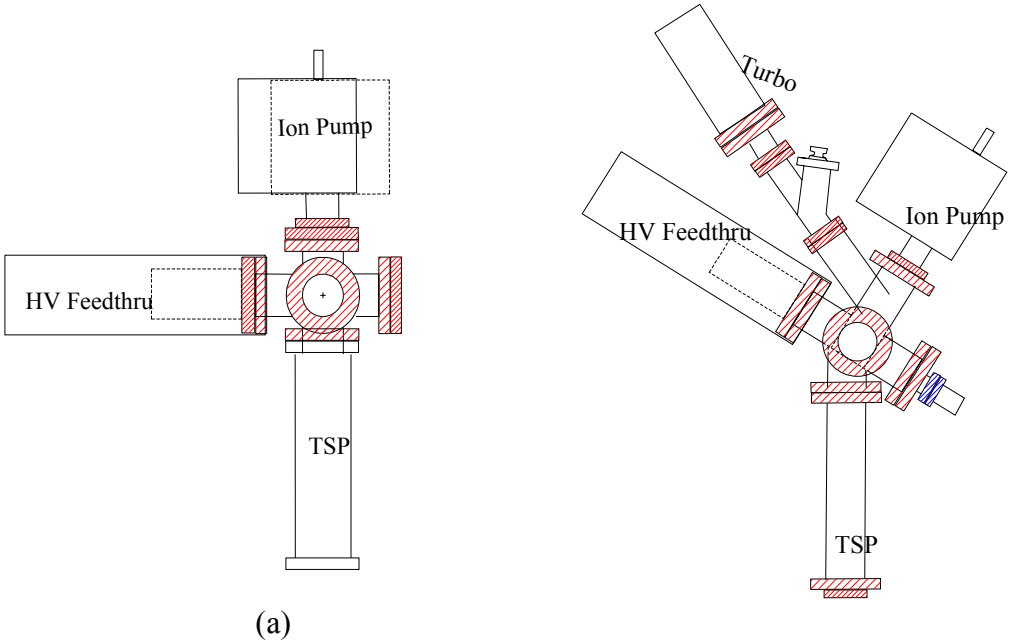

(a)

(b)

Fig. **4-2**: Six way crosses. (a) Top view of the six-way cross on the top of the glass chamber. (b) Top view of six-way cross below the glass chamber.

HV feedthroughs have not been assembled in the system yet. A turbo pump is used to pump the system first, and then ion pumps are turned on. The valve before the turbo pump is closed after that. A special stainless steel ring is put in the TSP tube as shown in Figure **4-3** to limit the flux of the evaporated titanium, prevent it from depositing on the spacers between the E-field plates.

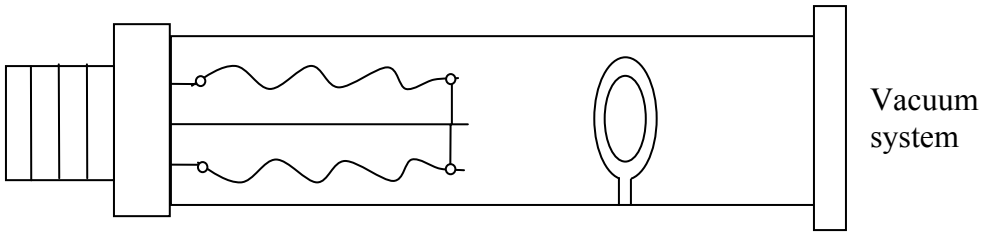

Fig. **4-3**: A stainless steel ring in TSP to limit the Ti flux deposit on the spacers.

The top six-way cross is mounted from the table on I-beams and connects with the glass chamber through a welded bellow to minimize the stress on the glass chamber. A 1.5×2.4 cm square tube is put between the main chamber and the measurement chamber to limit the flux from the main chamber to keep a high vacuum in the measurement chamber. In order to get a better vacuum, a TSP may ultimately be needed on the top six-way cross.

4.3. Diode laser system

All the cooling, repumping and detection laser beams are different for Cs and Rb atoms except for the 1D optical lattice, which is a YAG laser, far-off-resonance for both Cs and Rb atoms. The two different frequency laser beams (852 nm for Cs atoms and 780 nm for Rb atoms) are combined together through a dichroic mirror, which reflects light at 852 nm frequency and transmits light at 780 nm frequency. There are 4 diode lasers for the Cs atoms and 5 diode lasers for Rb atoms. The repumping laser for Cs atoms is locked to the Cs D_2 line F=3 → F'=3 and F'=4 crossover using saturated absorption spectroscopy techniques [76, 77], and then turned to the right frequency by AO modulators. The locking diagram is shown in Figure **4-4**.

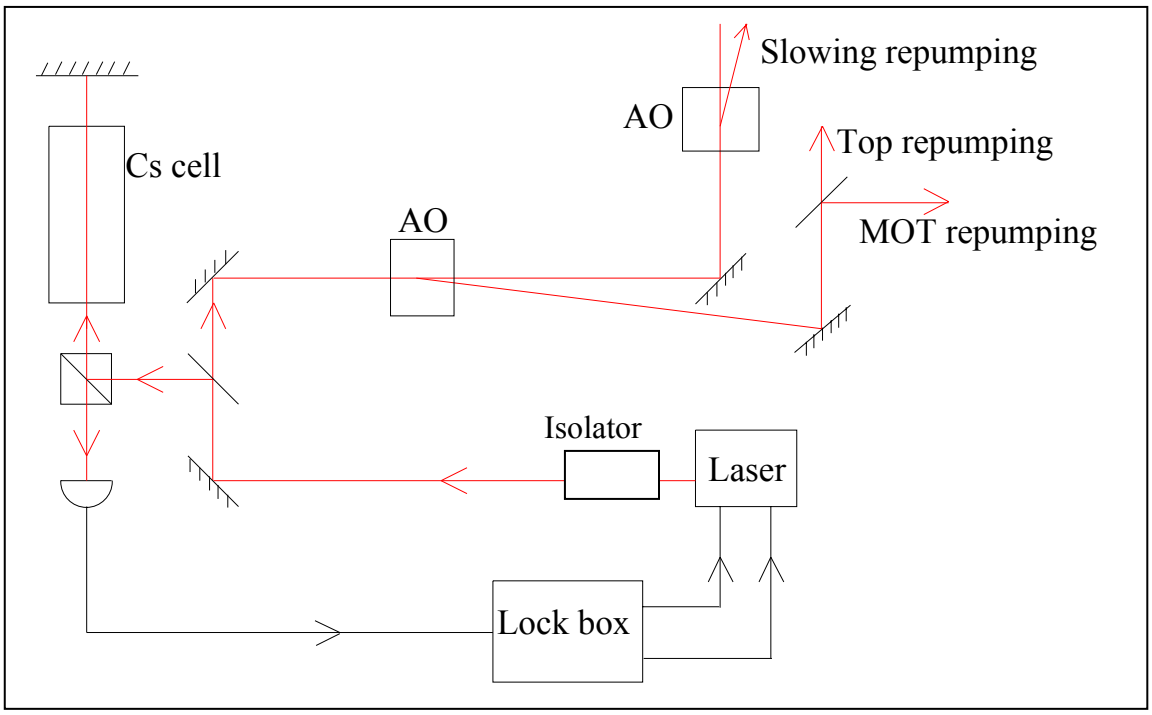

Fig. **4-4**: Schematic of repumping laser locking system for Cs atoms. Not all optical elements present in the experiment are shown. 10% of the incident beam is reflected from a beam splitter (BS) and double passed through a 5 cm long Cs cell. The saturation absorption spectrum signal is recorded by a photodiode and sent into the lock box. The error signal is driven by dithering the current applied on the diode. 90% of the transmitted laser beam will be used as the repumping beams (slowing, top and MOT optical molasses beams).

The current through the diode laser is modulated by a 3 kHz signal. Consequently, the absorption of the probe beam is modulated at this frequency and gives an error signal. The saturation absorption spectrum signal is recorded by a photodiode and sent into the servo circuit to lock the laser frequency. Two acousto-optic modulators (AOMs) are used to tune the laser frequency. One is for the repumping for the MOT and the top cooling system, the other one is for the slowing repumping. The repumping laser system for Rb atoms is similar to this.

The other near resonance laser beams for Cs atoms are provided by two high power diode lasers (SDL 5422-H1 laser diode), which are seeded by a master laser. The master laser is locked to the Cs D2 line F=4 → F'=4 and F'=5 crossover also with saturation absorption. The laser frequency is modulated by a homemade electro-optic modulator (EOM) at the frequency of 36.74 MHz (the modulation frequency is the measured resonance frequency of the EOM). The schematic of the laser locking diagram is shown in Figure **4-5**.

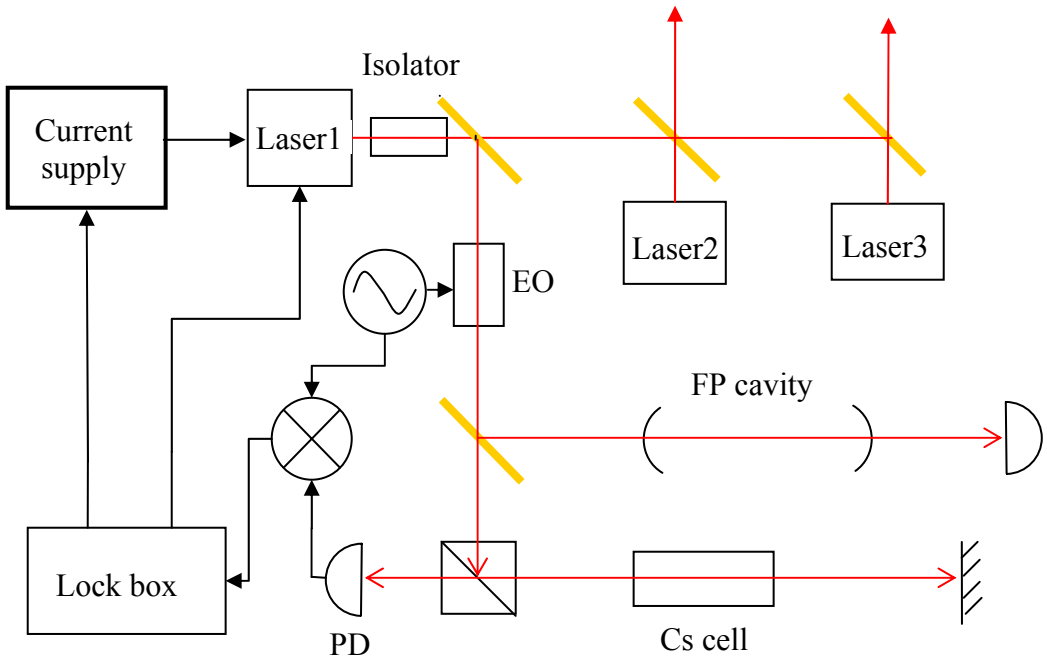

Fig. **4-5**: Schematic of the master laser locking for Cs atoms. The laser beam is frequency modulated by an EO modulator and double passes through a 5 cm long Cs cell. The saturation absorption spectrum signal is recorded by a photodiode and mixed with the EO driving frequency. The error signal goes into the lock circuit. The main beam passes through the beam splitter and seeds to diode lasers. The laser frequency is

monitored by the FP cavity.

Different from the repumping laser locking system, the frequency modulated saturation absorption signal is detected by a photodiode and then mixed with the EOM driven frequency. The error signal is sent to the servo circuit to control the laser current and a piezo. The laser beam transmitted from a beam splitter seeds 2 main lasers, which thus have exactly the same frequency and linewidth. The laser frequencies are monitored by a Fabry-Perot (FP) cavity. The Rb atom's laser locking schematic is similar to the Cs atom's system except that the master laser seeds 3 lasers and the locking is computer controlled (the circuit is shown in appendix B). The Cs master laser linewidth is 72 kHz. Laser 2 is used as the MOT's 2 pairs of 45° optical molasses beams, top optical molasses beams and top optical pumping beams. Laser 3 is used as the MOT horizontal optical molasses beams and the slowing beam. The frequencies of these laser beams are controlled by a series of AOMs. The 2 pairs of MOT cooling beams double-pass through AOMs to keep the alignment during the launch when the frequencies of the beams need to be changed. Pinholes are used for these beams to filter the spatial mode. The other pair of OM beams alignment is kept unchanged by coupling the laser into a fiber after the AO modulator. These beam diameters are about 16.5 mm (where the intensity falls to e^{-2}).

Another 3 pairs of OM beams are used in the measurement region to stop and cool atoms. In the vertical direction, the beam has an angle with the 1D lattice about 0.5 degrees, and is circularly polarized light with a $\lambda/4$ wave plate before the reflection mirror to flip the polarization. The beam diameter is about 3.5 mm before the top vacuum window and is about 2.8 mm after it is reflected back from the mirror, which is

2 meters away. The horizontal OM beams pass through a spherical lens first, followed by a cylindrical lens. The beam is collimated in a horizontal direction and diverges in a vertical direction. The total optical path from the fiber coupler to the atoms is about 110 cm, so near the center of the vacuum chamber, the beams are close to being plane waves. In the vertical direction, the beams are dramatically elongated to about 72 mm long; in the horizontal direction the beam size is about 7.6 mm. The beam path is shown in Figure **4-6**. The beams are linearly polarized, one 'S' , the other 'P'. The optical paths of the 'S' and 'P' laser beams are matched to keep the intensity balanced in the center atoms' region.

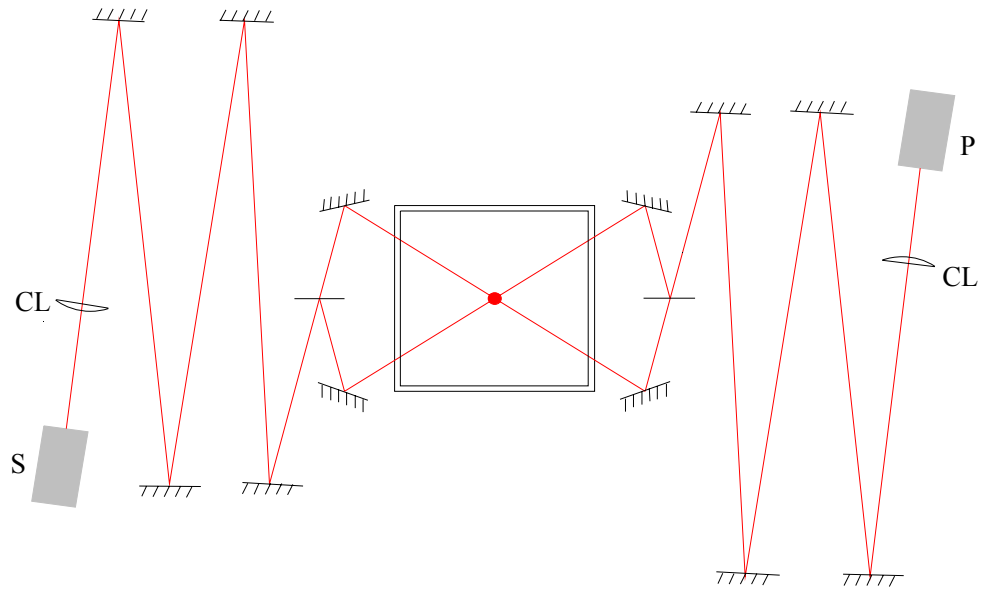

Fig. **4-6**: Optical path diagram for the upper horizontal optical molasses beams. One beam's polarization from the fiber coupler is set to S, the other beam's polarization is set to P. The beams pass through a spherical lens first and are collimated by a cylindrical lens. The beam is collimated in a horizontal direction and diverges in a vertical direction. The total optical path from the fiber coupler to the atoms is about 110 cm.

4.4. Resonator enhanced 1D optical lattice

Far-off-resonance traps (FORT) have been used in many experiments to trap atoms [78, 79]. They employ the optical dipole force to confine atoms. The origin of dipole forces is the ac Stark shift. For a two-level system in the limit of $|\delta| >> \Omega$ (Rabi frequency), the ac Stark shift of the ground state is given by [56]:

$$\Delta E_g = \frac{\hbar\Omega^2}{4\delta} = \frac{\hbar\gamma^2 I(r)}{8\delta I_s}, \tag{4. 1}$$

where γ is the excited state's decay rate, I_s is the laser saturation intensity. From this equation, we can see that a red detuned laser beam will produce an attractive potential, whereas a blue detuned laser beam will produce a repulsive potential. For 1D lattice traps, only red detuned trap can be used. We can see from equation 4.1 also that the trap potential is inversely proportional to the detuning, and the scattering rate is inversely proportional to the detuning squared, which has been discussed in chapter 3. A FORT can provide deep enough traps and still keep low a scattering rate. It can also be used to trap two species together as long as all the resonance lines for these two species are far detuned.

In our experiment, we use a YAG laser. The two closest transitions (the D1 line and the D2 line) for Cs and Rb atoms need to be included to obtain the trap potential. Contributions from other atomic transitions are negligible. We have:

$$U_{trap}(r) = \frac{\hbar I(r)}{8}\left(\frac{\gamma_{d1}^2}{I_{s,d1}\cdot\delta_1} + \frac{\gamma_{d2}^2}{I_{s,d2}\cdot\delta_2}\right) \tag{4. 2}$$

Cs atoms γ_{d1} is $2\pi\times4.56$ MHz, γ_{d2} is $2\pi\times5.22$ MHz, $I_{s,d1}$ is 2.5 mW/cm^2, $I_{s,d2}$ is 1.65 mW/cm^2. For a standing wave, a 1W laser for one beam provides potential of:

$$U_{trap}(r) \sim \begin{cases} 1.2\mu K & (Cs) \\ 1\mu K & (Rb) \end{cases} \tag{4. 3}$$

4.4.1. Cavity finesse and enhancement factor

The 1D optical lattice trap is resonator enhanced. The laser is a LightWave model 126 single mode (TEM00) single frequency laser with a wavelength of 1.064 μm, and a linewidth of 5 kHz. The laser is amplified by an IPG (YAR-10-1064-SF-PM) fiber-amplifier first. The output power from the fiber amplifier is from 100 mW to 10 Watts. Because the fiber amplifier is extremely sensitive to the back reflection, 2 isolators have been used to isolate the cavity reflection back into the fiber amplifier. The laser beam is modulated with a homemade EO phase modulator before it is amplified. The EO modulator has a resonance frequency of 10.6 MHz. The laser power injected into the cavity is controlled with a Pockels cell followed by a Glan laser prism. The two cavity mirrors have a radius of 2 m. The cavity is 3 centimeters longer than the confocal condition to ensure that only the TEM_{00} mode, with a waist of $w_0 = 0.63$ mm at the cavity center, is filled. The locking schematic of the YAG laser to the 2 meter long cavity is shown in Figure **4-7**.

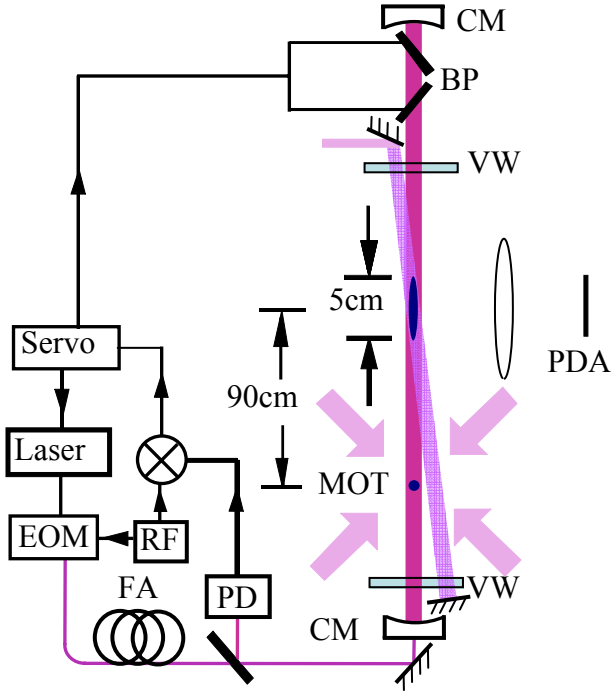

Fig. **4-7**: YAG laser locking system sketch. The laser beam frequency is modulated by an EO modulator and amplified before injected into the cavity. The reflection beam from the cavity is detected by a photodiode and mixed with the RF which drives the EO, and sent to the servo circuit to lock the laser frequency to the cavity resonance at high frequencies and cavity resonance locked to the laser at low frequencies. FA: fiber amplifier, PD: photodiode, CM: cavity mirror, VW: vacuum window, BP: Brewster plates.

The cavity is external to the vacuum chamber, so it contains two vacuum windows made of OH^- free IR-grade fused silica to reduce the absorption at 1064 nm and to avoid thermal lensing, and a pair of Brewster plates to turn the cavity resonance. The vacuum windows are mounted on flanges first as shown in Figure **4-8.**

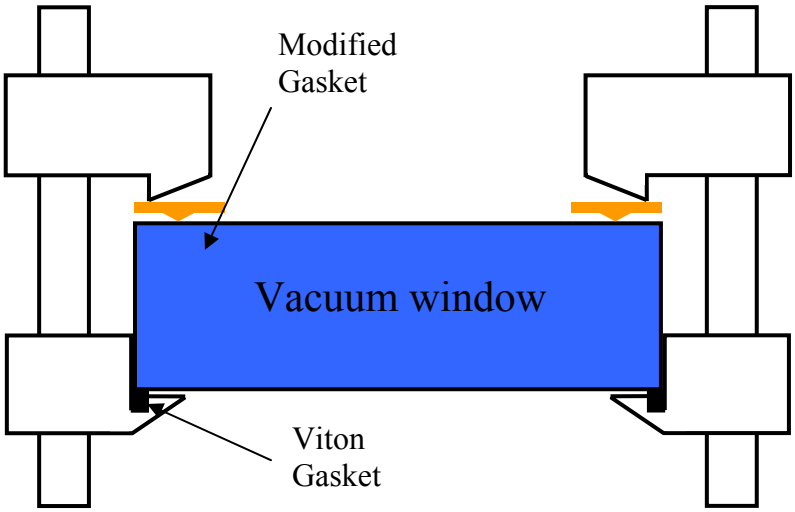

Fig. **4-8**: Vacuum window mount

Then, the flanges are mounted on a test vacuum chamber, and the seals between the vacuum windows and the flanges are checked. The torque applied on the windows is gradually increased until there is no leak. Usually the required torque is less than 30 pounds·inch. Then the window flange is taken off from the test chamber. The stress-induced birefringence of the window is measured. Before the vacuum windows, unwanted polarization of the YAG laser beam is less than 5×10^{-5} (which is the ratio between the transmission power after a laser glan and laser power before the laser glan, which could come from the imperfection of the laser polarization or imperfection of the laser glan). The vacuum window increases the fraction of the unwanted polarization to $(9 – 250) \times10^{-5}$ depending on the window's orientation angle. The window flanges are attached to the vacuum chamber with their birefringence axis as close to the polarization direction as possible, which is to within10 degrees.

For the build up cavity, we have the following equations [80]:

$$F = \frac{2\pi}{T_1 + T_2 + \ell}, \tag{4. 4}$$

$$\frac{P_r - (1-\varepsilon_m)P_{in}}{\varepsilon_m P_{in}} = (\ell_l + T_2 - T_1)^2 \left(\frac{F}{2\pi}\right)^2 \tag{4. 5}$$

where P_{in} denotes the input power, P_r denotes the reflected power, T_1 is the transmission of the coupled-in mirror, T_2 is the transmission of the coupled-out mirror. The mode matching factor ε_m is the ratio between the power coupled into the cavity and the total input power of P_{in} for the cavity TEM_{00} mode. From the equation, we can see that in order for all the power to be coupled into the TEM_{00} mode, the coupling-in mirror's transmission should equal to the round trip loss l_l plus the coupled out mirror transmission.

The coupling-out mirror has T_2 = 0.1% in the cavity. The coupling-in mirror was T_1=0.7%. Both the reflected and transmitted signals are measured with photodiodes and the data are shown in Figure **4-9**

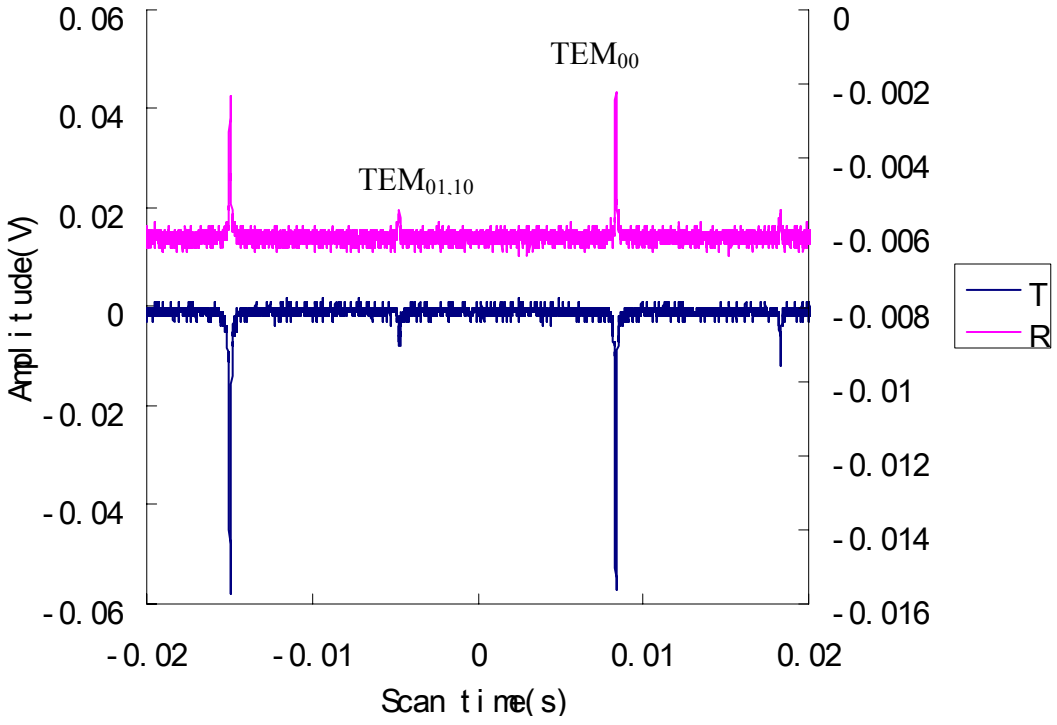

Fig. **4-9**: FP Cavity transmission and reflection. The blue curve is the transmission signal and the pink curve is the reflection signal. The small feature is the TEM01. The cavity is 2 meter long. The free spectrum range is 75 MHz.

From the transmission of the cavity, we can get the finesse of the cavity:

$$F = \frac{FSR}{Linewidth} = \frac{23.35ms}{0.086ms} = 271, \qquad (4.\ 6)$$

where FSR is the free spectrum range of the cavity. The enhancement factor Q (the ratio between the power inside the cavity and the input laser power) can be obtained by:

$$Q = \frac{Cavity\quad power}{Input\quad power} = \frac{580mV \times 8.3W / 100mV}{0.09W} = 53.5 \qquad (4.\ 7)$$

The coupled-in efficiency is: $\eta = 66\%$. The round trip loss of the cavity is 1.5%. The maximum power density inside the cavity exceeds 160 Watts, which corresponds to a trap potential depth of 200 μK.

4.4.2. Cavity locking

A Pound-Drever-Hall FM signal [81] is used to lock the cavity resonance to the laser frequency. The modulation frequency 10.6 MHz is chosen to be much less than the free spectral range (75 MHz) and much larger than the frequency difference between the TEM_{00} and TEM_{02} modes (~1.2 MHz). The reflection signal from the cavity is detected by a photodiode and mixed with the same frequency RF signal that drives the EO modulator, and the low-pass filtered signal from the mixer is sent to the servo circuit as the error signal to lock the laser to the cavity. The error signal is shown in Figure **4-10**.

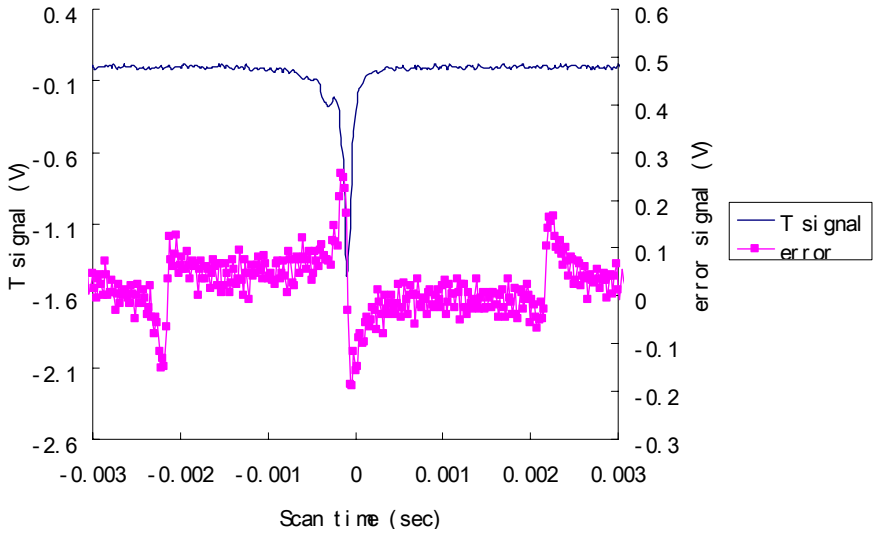

Fig. **4-10**: Transmission and error signals. The laser beam is modulated by an EOM

with driven a frequency of 10.6 MHz. The error signal was gotten from the mixer.

The lock servo circuit diagram is shown in appendix C. It has two output signals. The fast response feedback signal goes to the YAG laser to lock the laser frequency to the cavity resonance. The slow response feedback signal goes to the Brewster plates which are mounted onto two galvos to control plate angles to tune the cavity resonance to the YAG laser frequency. The servo system response is shown in Figure **4-11.**

The galvo response is 2 MHz/mV. The error signal is 6 kHz/mV. From figure (a), we found that the low pass filter servo bandwidth is about 700 Hz, that is, there is a π phase shift at 700 Hz. The high frequency response bandwidth is about 20 kHz. At this frequency, the phase shift is about π, and the gain reduces to less than 1.

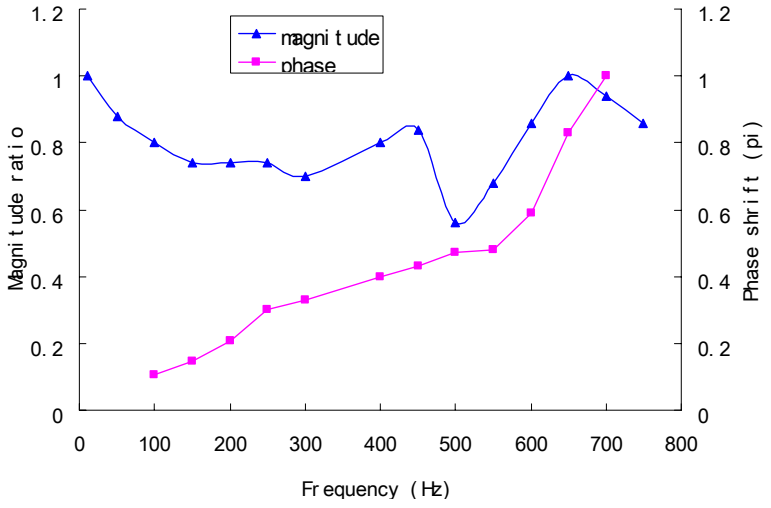

(a)

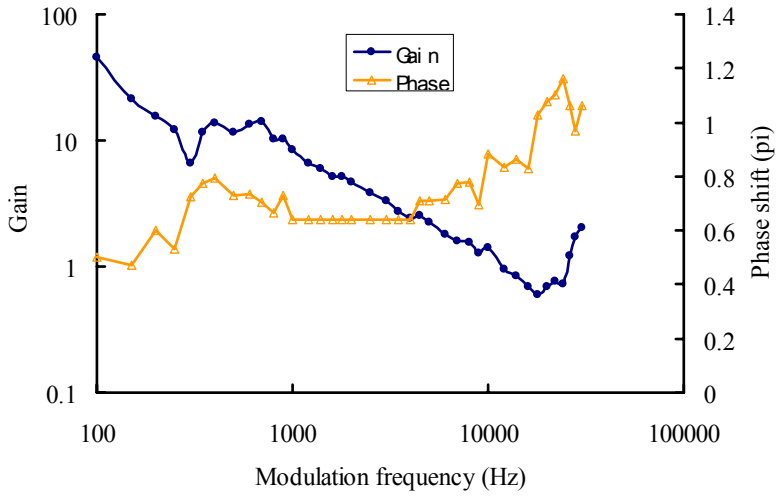

(b)

Fig. **4-11**: Servo system frequency response. (a) Low frequency response, (b) High frequency response.

4.4.3. Cavity transmission noise spectrum

The Brewster plates, which are used in the cavity to lock the cavity resonance to the YAG laser frequency, also filter out unwanted polarization, which is critical for reducing the systematic error as mentioned in chapter 3. The resonator has a well-defined spatial mode, so the laser beam pointing noise will convert to intensity fluctuations to heat the atoms [79]. In our locking system, the bandwidth of the circuit is lower than the axial trapping frequency, so the noise at this frequency cannot be reduced. The noise at twice the trap transverse frequency mainly comes from the vibration of the table.

The laser intensity inside the cavity is proportional to the transmission from the cavity. The transmission power is detected by a photodiode. Under the transmission

signal V_T = 0.390 V (measured from the oscilloscope), the noise spectrum at around twice the radial and axial frequencies are shown in Figure **4-12**, which is measured with SR760 spectrum analyzer. The fractional laser intensity fluctuation inside the cavity is:

$$\varepsilon_I(t) = \frac{I(t) - \langle I \rangle}{\langle I \rangle} = \frac{\delta V_T}{\langle V_T \rangle} \qquad (4.\ 8)$$

From equation 2.15, we can get the energy *e*-folding time $T_h = (\pi^2 \omega_x^2 S_k(2\omega_x))^{-1}$, where a one sided power spectrum of the fractional fluctuation in the spring constant $S_k(2\omega)$ can be obtained by:

$$S_k(\omega) = (\frac{\delta V_{Trms}}{\langle V_T \rangle})^2 \qquad (4.\ 9)$$

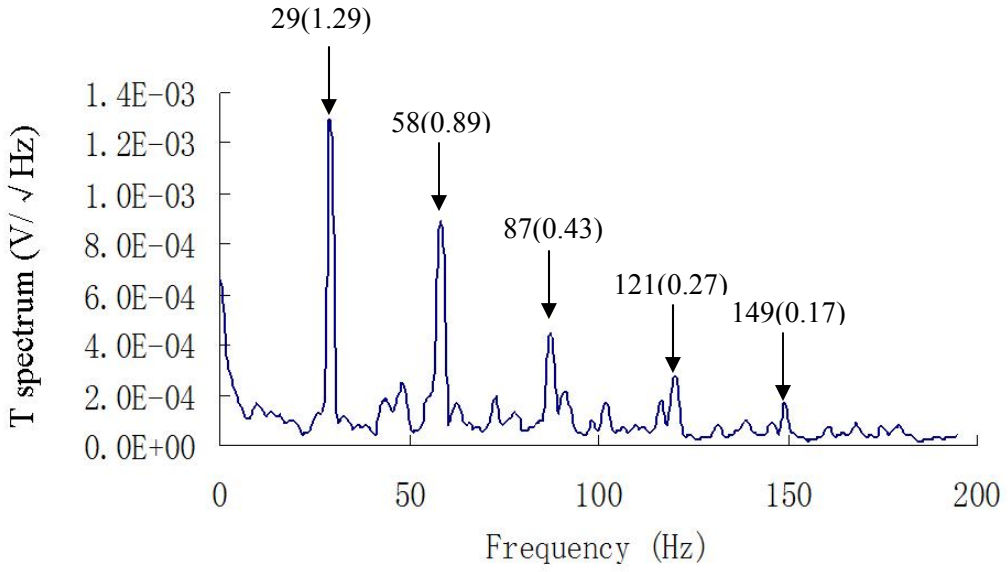

(a)

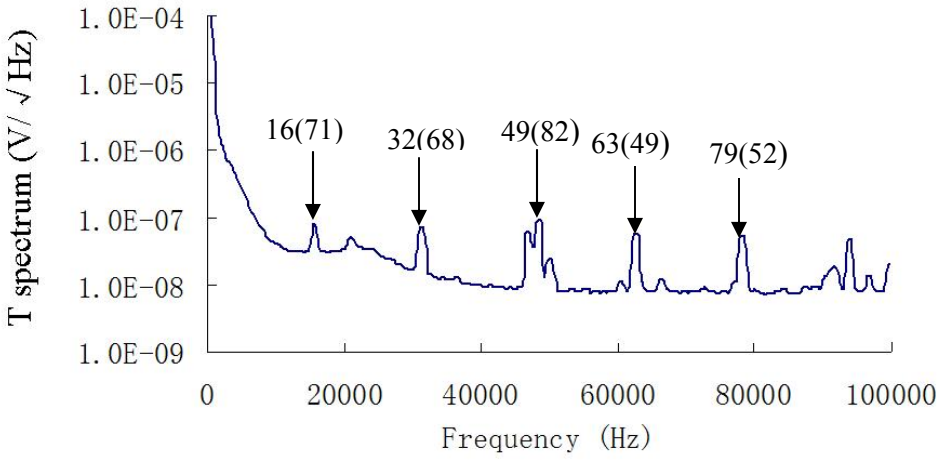

(b)

Fig. **4-12**: Cavity transmission noise spectrum. The average transmission signal is 390 mV (a) Low frequency range (0-200 Hz). The labels on the peak are the frequency with unit of Hz (magnitude with unit of mV) (b) High frequency range (0-100kHz). The labels on the peak are the frequency with unit of kHz (magnitude with unit of nV)

There are some resonant peaks in the noise spectrum. We don't know exactly what our trapping frequencies are, but this frequency can be slightly turned by changing the injection laser power, to avoid the noise peaks. At frequencies from 10 to 200 Hz, the noise spectrum density is about $0.2\,mV/\sqrt{Hz}$ (away from peaks), while at high frequency range (a few tens kHz), the noise spectrum density is about $20\,nV/\sqrt{Hz}$ (away from peaks). At the trapping potential of 100 μK, which we are using to measure the spectrum, we have

$$T_h = \frac{1}{\pi^2 \upsilon_r^2 S_k(2\upsilon_r)} = \frac{1}{\pi^2 \cdot 110^2 \cdot (0.2/390)^2} \sim 30\,\text{sec}$$

$$T_h = \frac{1}{\pi^2 \upsilon_y^2 S_k(2\upsilon_y)} = \frac{1}{\pi^2 \cdot (3\times 10^5)^2 \cdot (20\times 10^{-6}/390)^2} >> 30\,\text{sec}$$

The heating mainly comes from the low frequency. The expected energy *e*-folding time is about 30 s.

4.5. Fluorescence detection system

For the EDM measurement, the signals will be taken with 4 64-pixel photodiode arrays. The photodiode array is a Hamamatsu S8865-64 with 64 pixels and each pixel is 0.8 mm wide. The saturation output voltage is 3.5 V, and the noise level is 1 mV_{rms}. The noise to signal ratio is about 0.28×10^{-3}, which is less than the shot noise limit per shot $\frac{1}{\sqrt{n}} = 1.1\times10^{-3}$ for Cs atoms (10^8 atoms spread out 10 cm. The signal is taken with two 64 pixel photodiode arrays), and close to the shot noise limit for Rb atoms (0.24×10^{-3}). The photodiode array signal control diagram and the pulse sequences are shown in Figure **4-13.**

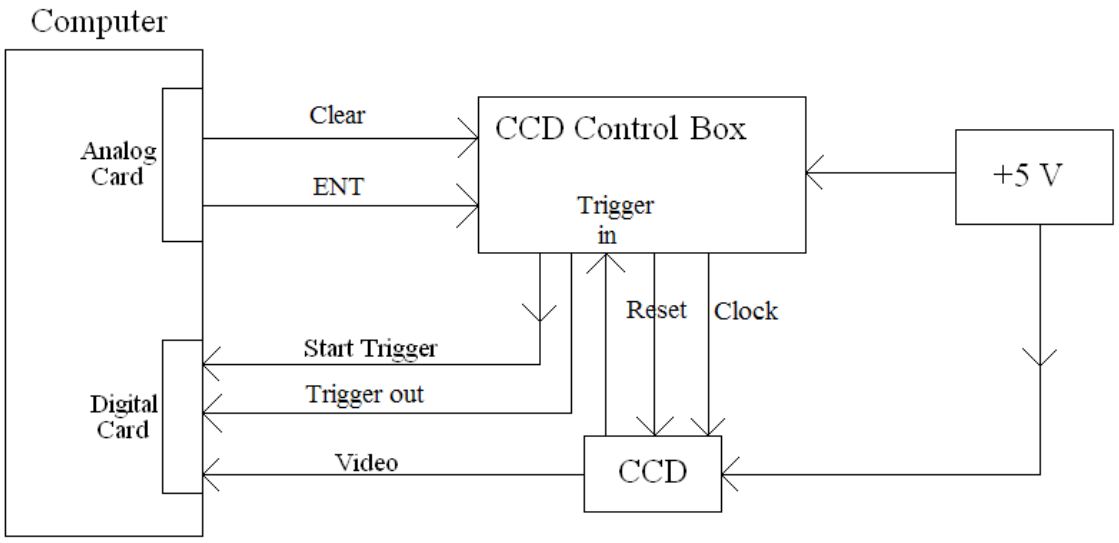

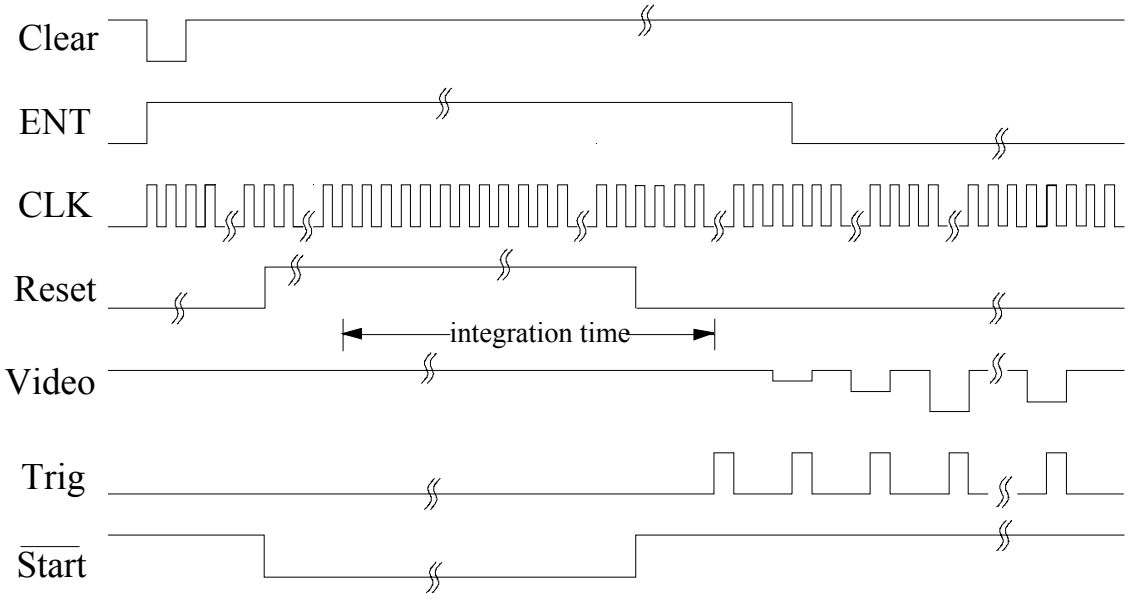

Fig. **4-13**: Photodiode control diagram. The CLK period is 2 μs, the integration time is 2048 μs. Clear signal is 4 μs, ENT high is 6 ms. Video signal and Trig signals are come from the photo diode array, one pixel is 2 period of CLK signal.

The clear and the ENT signals come from the timing board. The photodiode starts to integrate at 2064 μs after the ENT signal goes up. The integration time is 2048 μs. The video signal starts to read out 16 clock cycles after the reset goes down. The AD card reads the signals at the downward sloping trigger's edge, so the trigger signal is first inverted and then sent to the computer. The video signal has ripples at the trigger's edge. By adding a capacitor, it can be reduced. Figure **4-14** shows the video signals and the trigger signal (with a capacitor in the trigger signal, the circuit diagram is shown in appendix G), the peak to peak magnitude of the ripples is about 0.2 volts. Further consideration is needed if these ripples introduce noise into the EDM measurement.

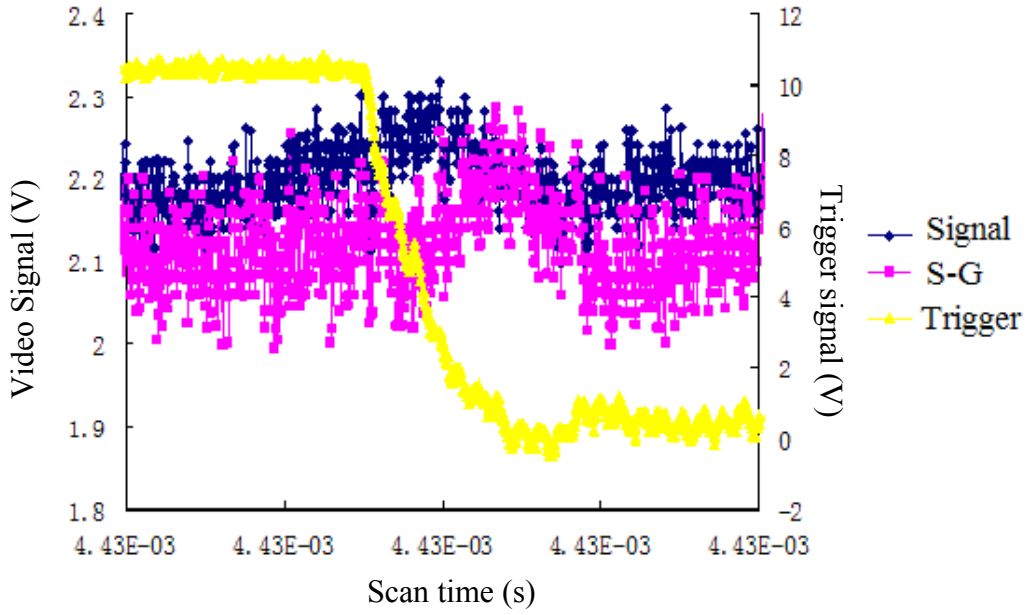

Fig. **4-14**: Trigger signal and video signals. The blue curve is the video signal measured directly and the pink curve is the video signal relative to the computer ground. The yellow curve shows the down edge of the trigger signal.

The measured sensitivity of the photodiode array is 0.96 V/nW at 852 nm (2.048 ms integration time). For Cs atoms, the maximum signal only needs to be 1 volt at 2 ms probe time to reach the shot noise limit. The imaging system collection efficiency η needs to be high enough to make sure the maximum output is 1 V (1 nW light illuminate on one pixel of the photodiode array). With high power on resonance probe laser [saturation illumination], we have:

$$\frac{N}{100}\cdot\eta h\nu\cdot\frac{\gamma}{2}\cdot 2\times 10^{-3}\geq 1\times 10^{-9}\rightarrow\eta\geq 10\% \qquad (4.\ 10)$$

To get this collection efficiency, the radius of the lens needs to be about 1 inch when the distance between lens and atoms is about 3 inches. (The commercial lens has

large imaging error, especially the view distortion. The data of this is shown in appendix E).

4.6. Computer control system

The supertime v3.1 vi's data is outputted via 7 National Instruments boards: five PCI 6713 analog output cards and two PCI-6534 high speed digital I/O timing cards. One digital card is used to generate the timing signal for the analog cards and the other digital card. The output from this timing card is rearranged together by a homemade digital circuit (Diagram is shown in appendix H) to create the actual timing signal. The other digital card is used as the digital signal control and has 64 channels. Five analog cards are used as the analog signal control and have 40 channels in total. We also have a 64 channel PCI 6071 analog input card, which can read in the photodiode array data, and the data from the photodiode. It can also be used to read in the magnetic field data or other instruments during the EDM measurement. The program to read the photodiode array data is photodiode v1.2 (It is a modified version from the program in Labview example programs. The card starts to read data when it receives a trigger signal, but the total time in the front panel still needs to be set close to the time period set in the supertime program to synthesize the two programs). A DT-3155 card is used to read the data from Pulnix CCD camera. (The CCD and photodiode data acquisition program cannot both run with the timing program on the same computer. We are not clear about the reason for this. It is possibly because they share the same PCI bus.) The timing program has two ways to repeat running, one is the software trigger, one is the hardware

trigger. In the hardware trigger mode, the whole time sequence will restart only when a line trigger signal comes. This will reduce to line noise. The line trigger circuit diagram is also shown in appendix K. A PCI6713 card can be used to generate the electromagnetic pulses to transfer atoms from the $|F, m_F = 0\rangle$ to the $|F, m_F = \pm F\rangle$ superposition.

Chapter 5

Atoms preparation and resonator enhanced optical guiding and trapping

In this chapter, the Zeeman slower and MOT performance are described. The atoms are transported from MOT to the measurement region while guided by cavity-enhanced 1D optical lattice traps as shown in Figure **5-1**.

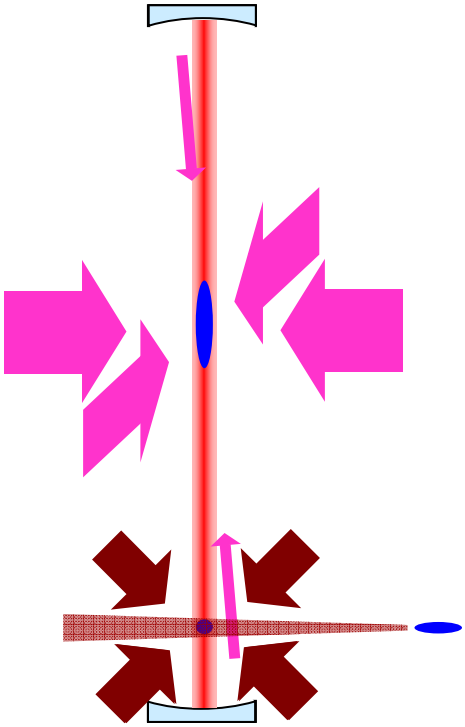

Fig. **5-1**: Sketch of experimental setup. The hot atoms from the oven are slowed down in the Zeeman slower and loaded into the MOT. MOT cooling beams are also used as the OM beams to launch and cool the atoms. When atoms reach the center of the interaction region (90 cm above the MOT position), they are stopped and cooled again by another 3 pairs of the OM beams.

The 1064 nm wavelength optical lattice is made in a 2 m long build-up cavity of light, and provides a transverse guide depth of up to 200 μK. We demonstrate a 90 cm launch of Cs atoms guided by a 1D optical lattice with the transport efficiency of about 50% from MOT. While one group of atoms are moving up, the MOT can start to collect atoms again. We have demonstrated multiple launching and loading atoms to the upper region is. By turning on the top OM cooling beams at different time, atoms can be stopped at different positions. We show that with 3 launches, atoms can be stretched out over 5 cm, so that the effective volume of this extended atom trap is ~ 6 mm^3.

5.1. Slowing the thermal atoms

5.1.1. Zeeman slower

After the atoms exit the oven nozzle they can be slowed by interacting with a counter-propagating on-resonance laser beam. The absorption of photons from the slowing laser and the sequential spontaneous photon emission in random directions can efficiently reduce the atom velocity in the longitudinal direction. In order to continuously decelerate atoms from hundreds of m/s to tens of m/s, it is necessary to keep the laser frequency on resonance with the atomic transition during the whole slowing procedure in which atoms have different Doppler shifts. Phillips and Metcalf demonstrated the Zeeman tuned slowing technique in 1982 [3] and Ertmer et al showed slow atoms with chirping laser frequency in 1985 [4]. In our experiment, a σ^- Zeeman

slower [82] is used to produce a large number of low speed atoms for efficient MOT loading as shown in Figure **5-2.**

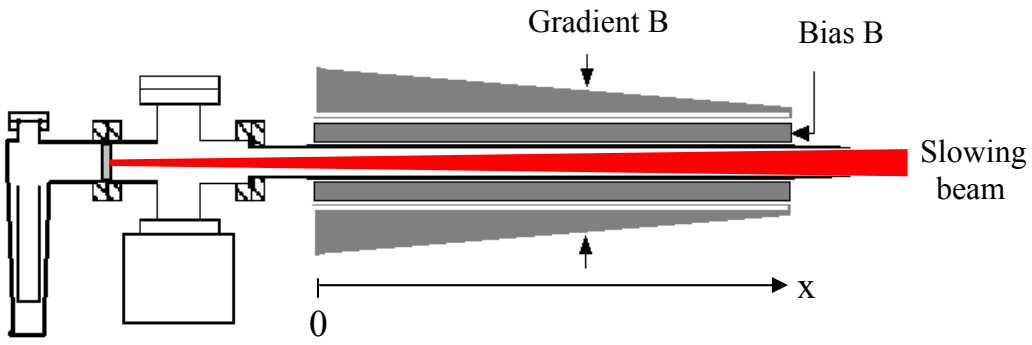

Fig. **5-2**: Schematic of Zeeman slower. The hot atoms from the reservoir are collimated by the nozzle first and then go to the Zeeman slower range about 1 meter long. The slower has 3 sets of coils: B bias and B gradient and B patch. The slowing and slowing repumping laser beams are partially focused on the nozzle.

Our Zeeman slower consists of Cs and Rb ovens, an ion pump and magnetic coils. Cs and Rb atoms are in separate ovens and can be heated independently. The temperature needs to have a gradient between the atom's reservoir and nozzle to make sure atoms do not stick on the nozzle. The nozzle temperature is kept at 50ºC when the experiment is not running. The flange which the nozzle is mounted on is cooled by running water all the time to make sure that the flange temperature does not change too much between when the experiments running or not. (We had a leak in this place at the beginning when we didn't have water cooling for this flange. The temperature changed a lot between running the experiment and not running the experiment, so the flange seal deteriorated.)

Three sets of solenoid magnets are used to generate the magnetic field. One is for the bias B field and the other 2 are the main gradient field coil and the patch coil to

generate the gradient B field. The gradient B field should have a profile [56] to match the velocity of slowed atoms:

$$B_{grad}(z) = B_{grad}\sqrt{1 - x / x_0} \tag{5. 1}$$

where x_0 is the total length of the slower, x=0 is the beginning position of the slower. This magnetic field causes a shift of the atom's Zeeman levels to compensate the change of Doppler shift due to deceleration. The total B field is:

$$B(z) = B_{bias} - B_{grad}\sqrt{1 - x/x_0} \tag{5. 2}$$

The slowing laser detuning is decided by the bias field B_{bias} and the atom's slowing velocity range is decided by the gradient field B_{grad}. Using the bias B field here is to have freedom to independently change the slowing beam frequency and make sure the atoms extracted from the Zeeman slower will not be on resonance with the slowing beam and will not be kicked back by the laser. For Cs atoms, the velocity that can be slowed is decided by the gradient field by:

$$\Delta v = \frac{1}{\hbar k}(g_e m_e - g_g m_g) \cdot B_{grad} = 1.2 \cdot B_{grad}(m/s) \tag{5. 3}$$

5.1.2. Velocity distribution after the Zeeman slower

For our Zeeman slower, the slowing laser beam is focused on the nozzle by two lenses outside the vacuum chamber. We found that the atoms are depumped to the F=3 hyperfine states during the slowing, so that they stop decelerating. A slowing repumper is necessary to pump back these atoms in order to continuously slow atoms. We monitor the atom's velocity distribution when they reach the MOT region. One laser beam

propagating at 45 degrees from the Zeeman slower direction is used as the detection beam. Its frequency is scanned to get the atom's velocity distribution. The atom signal is monitored on the oscilloscope, and the results are shown in Figure **5-3**. In the graph, the x unit is the detection laser frequency detuning (The laser is not locked. Its frequency is scanned by changing the AO driving frequency. The zero position drifts from shot to shot.). Another laser which is split from the detection laser, propagates perpendicular to the Zeeman slower and is used as a marker signal. In the Zeeman slower radial direction, the average atom velocity is zero and the velocity spread is small. The frequency of this laser when it is on resonance with atoms can be used as a marker for zero velocity. The atom's velocity can be determined from the detuning of the laser beam by:

$$\sqrt{2}k \cdot v = \delta \rightarrow v = 0.83 \times 10^{-6} \cdot \delta(m/s), \qquad (5.4)$$

where k is the laser beam wave vector, and δ is the laser beam detuning from $F = 4$ to F'=5 transition.

In the figure, the peak A is the marker signal for the position of the zero velocity. The peak B is the slowed atoms signal. Peaks C and D are atoms, which are not slowed. Without the slowing repumping laser beam, a large amount of atoms are not slowed as shown in (b), where the peak B is small. The total number of atoms can be calculated by integrating over some velocity range ($\int_{v_1}^{v_2}(Signal/v) \cdot dv$). By adding a repumping beam, 52% of the total atoms are removed in the velocity range 70-180 m/s. The slowed atoms are 24% of the total atoms compared with (a) in the velocity range of 70-180 m/s.

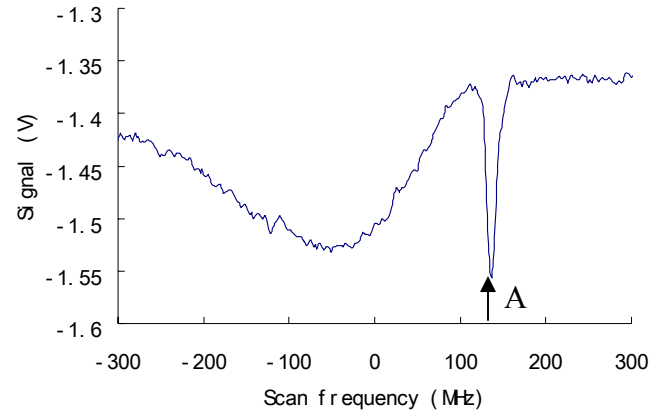

(a)

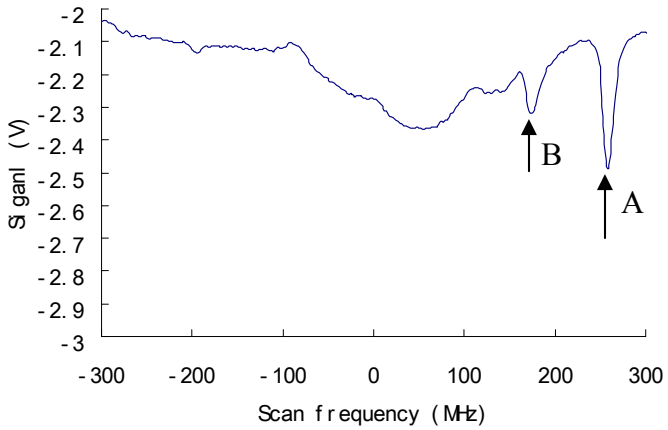

(b)

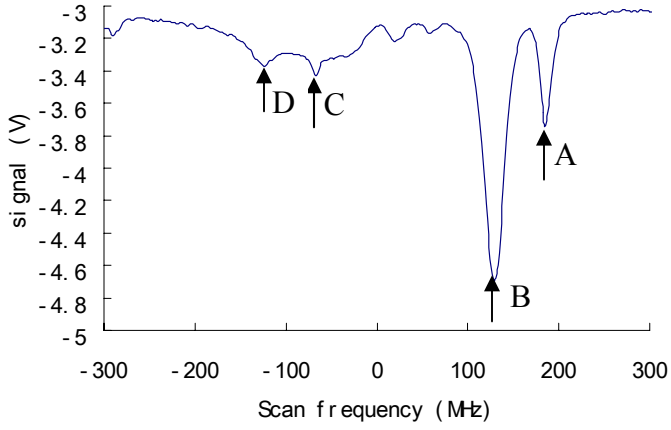

(c)

Fig. **5-3**: The atom's velocity distribution in the MOT region after Zeeman slowing. (a) Signal without the slowing beam (b) Signal without the slowing repumping (c) Signal with the slowing repumping.

The position of the small peaks C and D in figure (c) did not change when the slowing repumping frequency was changed, but the intensity of these peaks changed and the position changed when the B field was changed, which suggests that these features might be due to the imperfect changing of the B field along the slower. If the B field changes too fast in some places, atoms cannot be continuously slowed.

The field magnitudes due to these coils are:

$$\begin{cases} B_{bias} = 2.18 \quad Gauss / Amp \\ B_{grad} = 2.71 \quad Gauss / Amp \end{cases}.$$

At one setting of the slowing beam detuning, we tuned the B_{bias} and B_{grad} settings to optimize the MOT loading speed. The MOT loading rates at different slower laser detuning are measured to get the globe maximum. The best setting of the Zeeman slower for B_{bias}= 30 Gauss and B_{grad} = 170 Gauss. The slowing laser beam detuning is 55.3 MHz, the power is 20 mW, and the slowing repumping detuning is 42.3 MHz. At the maximum gradient B field, where the bias B field is changed by 20 Gauss, the loading speed drops in half.

5.1.3. Divergence of the atom beam and transverse cooling

The average longitudinal velocity of Cs atoms at 450 ºK (Oven temperature) is $v = \sqrt{\frac{KT}{m}} \sim 167 \quad m/s$. The nozzle we use here is a glass capillary array where each hole is 1 mm long and 10 μm in diameter. The average transverse velocity is about 5 m/s (roughly 3% of the axial velocity). The time for atoms to fly from the nozzle to the MOT is about 20 ms. This time is determined on the oscilloscope between the delay of the

MOT fluorescence signal and the start of MOT trigger. During the Zeeman cooling, atoms are heated in the transverse direction. The transverse heating is [83]:

$$\left(v_{x,y}^{rms}\right)^2 = \alpha \frac{v_{rec}^2}{3} N(t) \tag{5. 5}$$

where $N(t)$ is the total number of photons absorbed during the slowing time t, v_{rec} is the recoil velocity, α is a correction factor, which is about 1 in our case. The photon scattering leads to a transverse spreading of the beam given by [83]:

$$\left[x^{rms}(t)\right]^2 \sim \left(v_x^{rms}\right)^2 \frac{t^2}{3} \tag{5. 6}$$

For Cs atoms, the v_{rec} is 0.35 cm/s, the velocity increased due to heating is about 0.4 m/s, which is much less than the initial transverse velocity. One way to overcome the transverse expansion is to focus the slowing beam on the nozzle, so the atoms feel the radiation pressure in the transverse direction. In our experiment, we focused the slowing beam on the nozzle, but the measured flux near the nozzle is 1.7×10^{13} atoms/s is still much larger than the MOT loading rate. Adding transverse cooling before the Zeeman slower will dramatically improve the MOT loading speed [84].

5.2. Laser trapping and cooling of Cs and Rb atoms

The best tool for collecting ultra-cold atoms is the MOT [85]. A basic MOT requires three pairs of red-detuned, counter-propagating laser beams with opposite circular polarizations for each pair, and a pair of anti-Helmholtz coils to produce a quadrupole magnetic field near the MOT center. For alkali atoms, the MOT is often

operated between the upper ground hyperfine state F and the excited hyperfine state F'=F+1. Although direct decay into the lower ground state is forbidden, off-resonant excitations of the lower hyperfine excited state allow decay into the F-1 state, which removes atoms from the cooling cycle. An extra repumper laser needs to be added to pump atoms back to the F state.

5.2.1. Magneto-optical trap for Cs and Rb atoms

The MOT is very robust for cold atom preparation. It is fairly insensitive to trap parameters such as laser beam polarization, intensity balance, and beam alignment. We use the MOT laser beams as the optical molasses beams to cool atoms further after the MOT B field is turned off. During the launch, atoms will be moving in the OM beams about 4.5 mm, so the beams' profiles and intensity balances are very important to achieve low temperatures. For Cs atoms, six MOT beams drive the cooling transition ($6S_{1/2}F=4 \rightarrow 6P_{3/2}F'=5$), and a repumping laser ($6S_{1/2}F=4 \rightarrow 6P_{3/2}F'=4$) pump atoms on the F=3 back to the F=4 state. The laser beam sizes are about 8.3 mm (where the intensity drops to the e^{-2} of the peak intensity). The horizontal beams are spatially filtered by a single mode PM fiber. The maximum power of these beams is about 5 mWatts. The power in each beam of the two diagonal pairs is about 10 mWatts. These beams are spatially filtered with two pinholes. The detuning of these laser beams are shown in Figure **5-4** for Cs atoms and Figure **5-5** for Rb atoms. The MOT magnetic field

is provided by a pair of anti-Helmholtz coils with a gradient of 0.87 Gauss/mm (40A).

The Cs MOT signal is shown in Figure **5-6.**

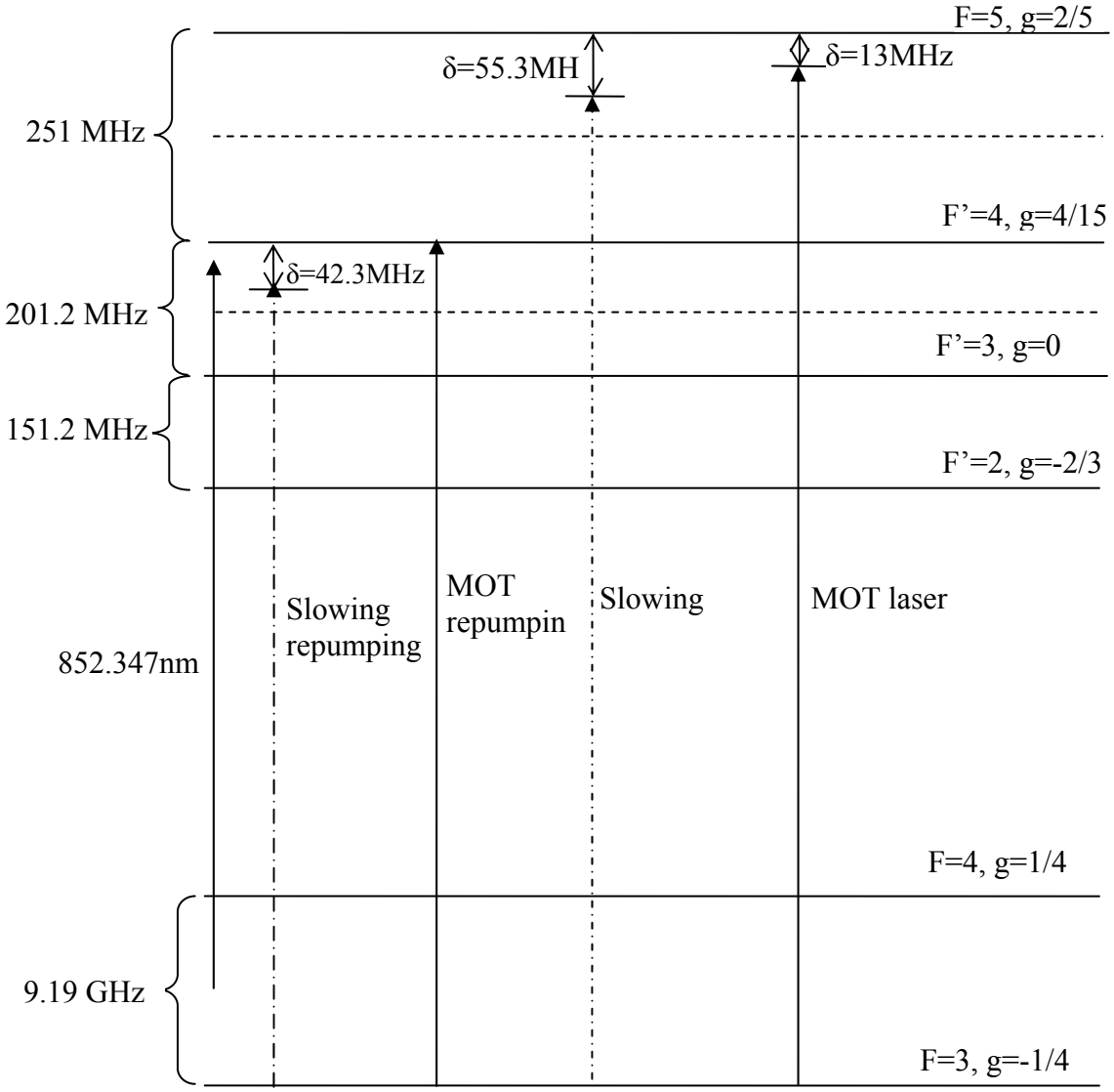

Fig. **5-4**: Frequencies of the laser beams derived from the master laser, main lasers and repumper lasers for Cs atoms. The horizontal dashed lines are the lock point of the master and repumping lasers. The 2 main lasers lock to the master laser. Their frequencies are tuned to the required frequencies by AOM. The 2 MOT laser beams double pass the AO modulators. The other laser beams pass the AO modulator once.

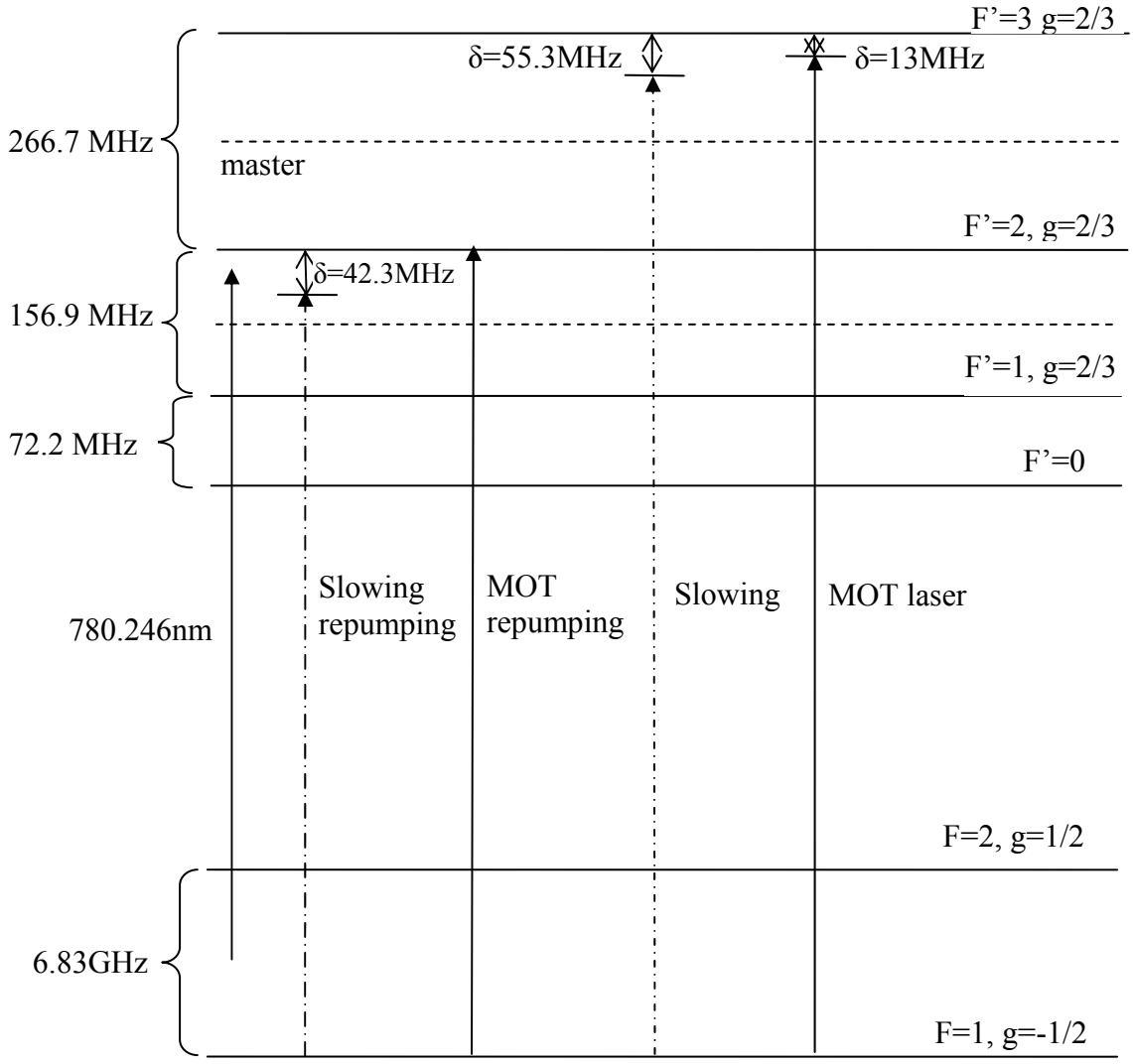

Fig. **5-5**: Frequencies of the laser beams derived from the master laser, main lasers and repumper lasers for ^{87}Rb atoms. The horizontal dashed lines are the lock point of the master laser and the repumping laser. The 3 main lasers lock to the master laser. And their frequencies are tuned to the required frequencies by AOM. The 2 diagonal MOT laser beams double pass the AO modulators. The other laser beams only pass the AO modulator once.

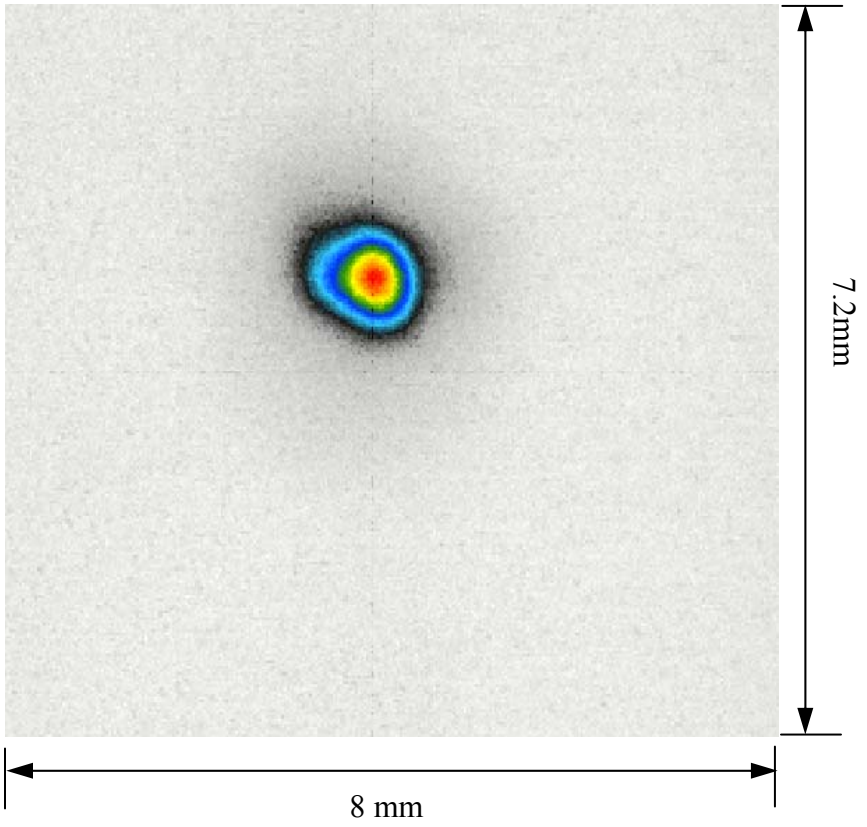

Fig. **5-6**: Cs MOT signal. The signal was taken by the Pulnix CCD camera after 500 ms of loading. The MOT size is about 1 mm (The MOT density drops to e^{-2} of the peak density).

The MOT signal is taken by a Pulnix CCD camera. The camera is set to the trigger mode, and it starts to integrate only when it gets a trigger signal from the timing board. Another control signal from the timing board is sent to the DT 3155 frame grabber card to signal it to begin reading the data.

5.2.2. MOT loading speed

The Cs and Rb MOT loading speeds are measured with a photodiode (FND100) with 1MΩ resistor. The sensitivity is 0.3 mV/nW. The atom number can be obtained by the following equation:

$$N \cdot \eta \cdot \frac{\Omega}{4\pi} \cdot \frac{s_0 \cdot \gamma/2}{1 + s_0 + (2\delta/\gamma)^2} = P, \tag{5. 7}$$

where N is the total number of atoms, η is the lens transmission efficiency, Ω is the solid angle of light collection, s_0 is the saturation parameter of the detection laser, δ is the detuning of the detection laser, and P is the power measured by the photodiode array.

For Cs atoms, when the oven temperature is set to 135 ºC, the s_0 is 5 and detuning is 2γ, the solid angle is about 1/400, the atom signal is 17.5 mV at 50 ms loading time. The corresponding loading speed is 2×10^8 atoms/s. For Rb atoms, the loading speed is 1.5×10^9 atoms/s.

5.2.3. Optical molasses cooling

After atoms are loaded into the MOT, the slowing and slowing repumping lasers are turned off. The atoms' positions change a few mm after the slowing beam is turned off due to the slowing beam radiation pressure. The MOT magnetic field is then turned off adiabatically in 4 ms. After that, the OM laser beam intensities are reduced and the detuning is increased to get a low temperature. The atoms' images are taken 20 ms after

they are released from the optical molasses. The temperature is determined from the expanding size of the atom cloud. The timing sequence is shown in Figure. **5-7.**

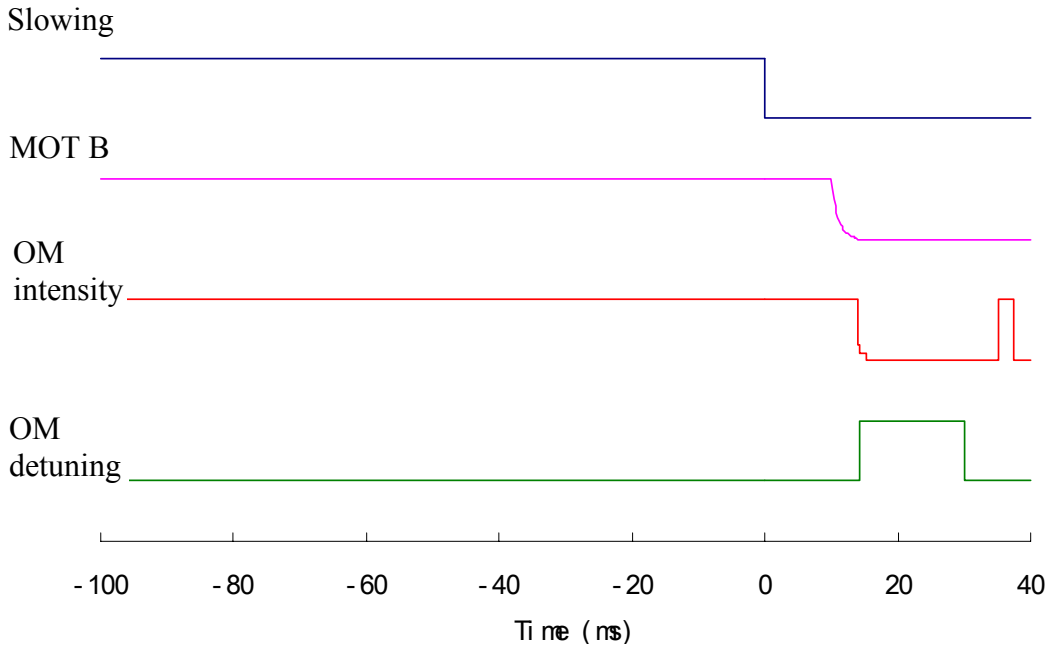

Fig. **5-7**: Timing sequence. After the loading, the slowing and slowing repumping laser beams were turned off first. Then the MOT magnetic field is turned off adiabatically in 4 ms. After that, the laser beam's intensities were reduced and the detuning was increased. The laser beams are briefly turned back on 20 ms after the atoms released from the optical molasses to act as probe beams.

The atoms average velocity can be obtained from the size of the atom cloud by:

$$v^2 t^2 = \frac{w^2 - w_0^2}{4}, \qquad . 8)$$

where t is the free expansion time, w_0 is the original width of the atom ball (Gauss width, not $1/e^2$), w is the width of the atomic ball after expansion. We first changed the bias B field settings to get the minimum atom expansion. The B fields are controlled by 3 pairs of Helmholtz coils controlled by the timing board. The atoms temperature is minimized

by changing the OM laser beams intensity and the detuning. The results are shown in Figure **5-8.**

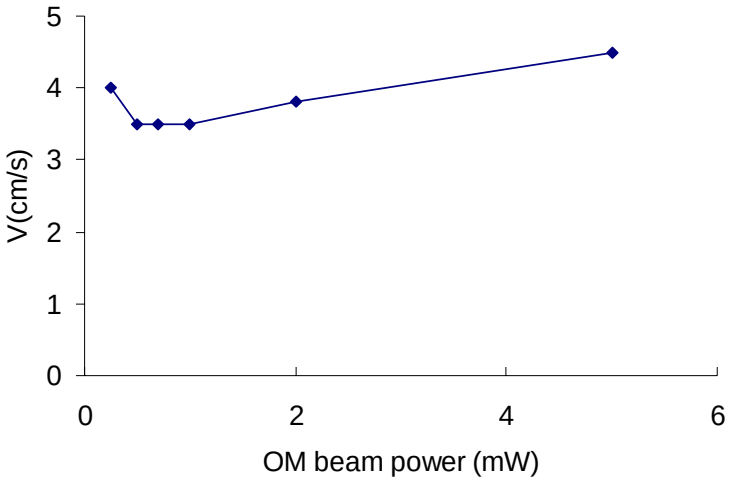

(a)

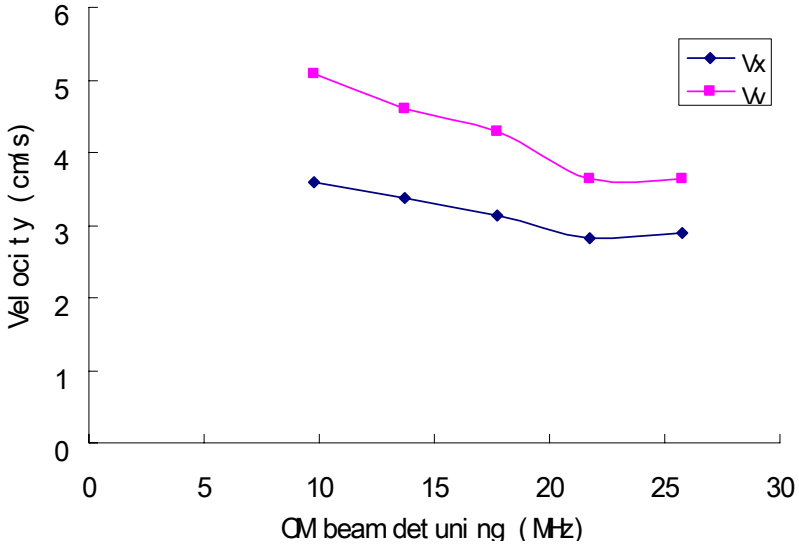

(b)

Fig. **5-8**: Atoms average velocity as a function of OM beam's intensity and detuning. (a) Atoms average velocity in the horizontal direction as a function of OM beam's power, the detuning is set to be 10 MHz. (b) Atoms average velocity as a function of OM beam's detuning.

From Figure **5-8**, we can see that the atoms average velocity is decreased when increasing the OM beam's detuning. The Zeeman slower provides a large magnetic field. It is unclear whether it should be on all the time or be switched off during the MOT's off cycle. The effect of keeping the Zeeman slower on is measured. The bias B-field settings are optimized separately under two different situations. After the slower B fields are turned off, the atoms are held in the MOT for a variable time (from 50 ms to 150 ms), then the MOT B field is turned off, and the atoms are cooled by the OM cooling. The atoms average velocity is measured and results are shown in Figure **5-9.**

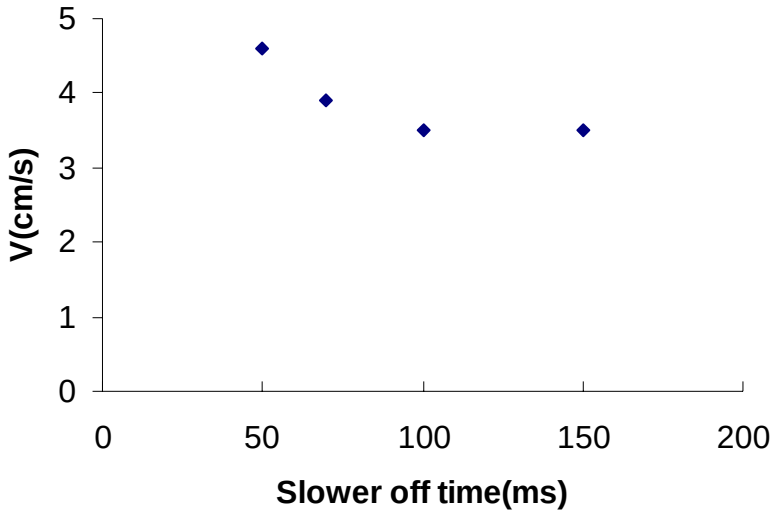

Fig. **5-9**: Atoms average velocity vs. the slower turn off time.

We can see from the above figure that the average velocity is higher at the earlier time when the slower is just turned off. After 100 ms, the fact that the velocity does not drop any more suggests that it needs 100 ms for the Eddy current generated by the slower to die off. The final average velocities of atoms with and without the slower B

field are about the same. So, just for the OM cooling, the slower B fields can be on all the time. If the final EDM measurement requires the slower B fields off, they can be turned off during the E field charging time.

5.3. Resonator enhanced optical guiding and trapping

The EDM experiment requires well-controlled magnetic fields. Since collecting ultra-cold atoms entails the use of magnetic fields in a magneto-optic trap (MOT) [85], and large field changes within magnetic shields are inconsistent with long-term stability, it is necessary to transport cold atoms into a magnetically shielded region, and trap them in the optical lattices. The most common transport technique, magnetic guiding, is of course inappropriate for this purpose [86]. Cold atoms have been transported non-magnetically by unguided launches and drops, dipole trap guided launches and drops, and optical tweezers. In our experiment, we launch atoms vertically while they are guided by a resonator-enhanced one-dimensional (1D) optical lattice. Before the atoms reach the top of their trajectory, they are stopped and cooled by optical molasses, becoming trapped in the 1D lattice 90 cm away from the MOT, far enough away to allow for very effective magnetic shielding. The overall transfer efficiency from the MOT to the 1D lattice trap is 50%. Compared with optical tweezers, this method is much faster and can transport more atoms per launch because the trap size is much larger than the focused light required for optical tweezers.

5.3.1. Moving molasses

Moving molasses is essentially optical molasses in a frame moving at a non-zero velocity relative to the lab frame [47]. It is a common technique used to launch atoms from a MOT to a distance above it while keeping the atoms cold. Figure 5-10 shows a diagram of the laser beam set-up used for the moving molasses in our experiment.

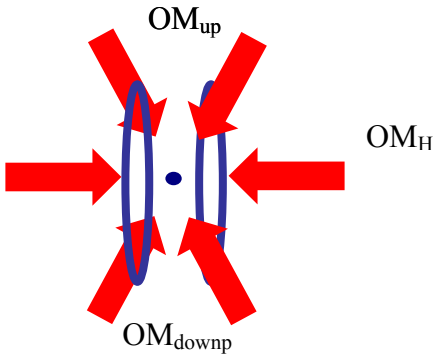

Fig. **5-10**: OM beams orientation

The beams initially have equal frequency ω before launching. The relative frequencies are changed during the launch. The down beams are changed to the frequency ω-2δ, the horizontal beams are changed to the frequency ω-δ, while the upper beams are kept at the same frequency. We have:

$$\begin{aligned} 2 \cdot \delta_H &= (\delta_{up} + \delta_{down}) \\ kv &= \frac{\sqrt{2}}{2} \cdot (\delta_{up} - \delta_{down}) \end{aligned} \qquad (5.9)$$

where δ_X is the detuning from resonance (X is *up, down* or *H*), v is the selected velocity, which atoms can get in the moving OM, and $k=2\pi/\lambda$ is the wave vector magnitude. The

2δ frequency difference of the up and down beams will cause the atoms to have an initial velocity $\sqrt{2}\delta/k$. The maximum height to which the atoms are launched is:

$$h = \frac{v^2}{2g} = \frac{\delta^2}{gk^2}. \qquad (5.10)$$

Acoustic-optics (AO) modulators are used to control laser frequencies in the experiment. Both the up and down beams double pass the AO modulators, while the horizontal beams pass the AO modulator once (The AO driving frequency for horizontal beams are always the sum of the frequencies which drive the up and down beams). These frequencies of AO modulators are controlled by SRS synthesized function generators. The frequencies are swept to the moving frame frequencies in 0.95 ms and then changed to a larger detuning while maintaining their relative frequency difference to get lower atom temperatures. The schematic of the frequency control is shown in Figure **5-11**.

The function generator frequency cannot cover the frequency for the AO driver, so frequency doublers are used. The AO driver frequencies for MOT status are ($2f_1$, $2f_1$, $4f_1$). During the launch, AO_{up} frequency keeps same while AO down frequency is swept from $2f_1$ to $2f_2$. The AO_H driver frequency needs to be swept from $4f_1$ to $2f_1+2f_2$, which is gotten by first mixing $2f_1$ with f_2. The frequency $(2f_1 + f_2)$ is selected by the high pass filter and is mixed with f_2 again. Another high pass filter is used to select the frequency ($2f_1+2f_2$). The leakage RF signals close to the selected frequency $2f_1 + f_2$ from the first mixer (such as $3f_2$, $4f_1-f_2$ etc) are third order and dramatically reduced to make sure the close frequency RF signals are small enough and do not affect laser intensity.

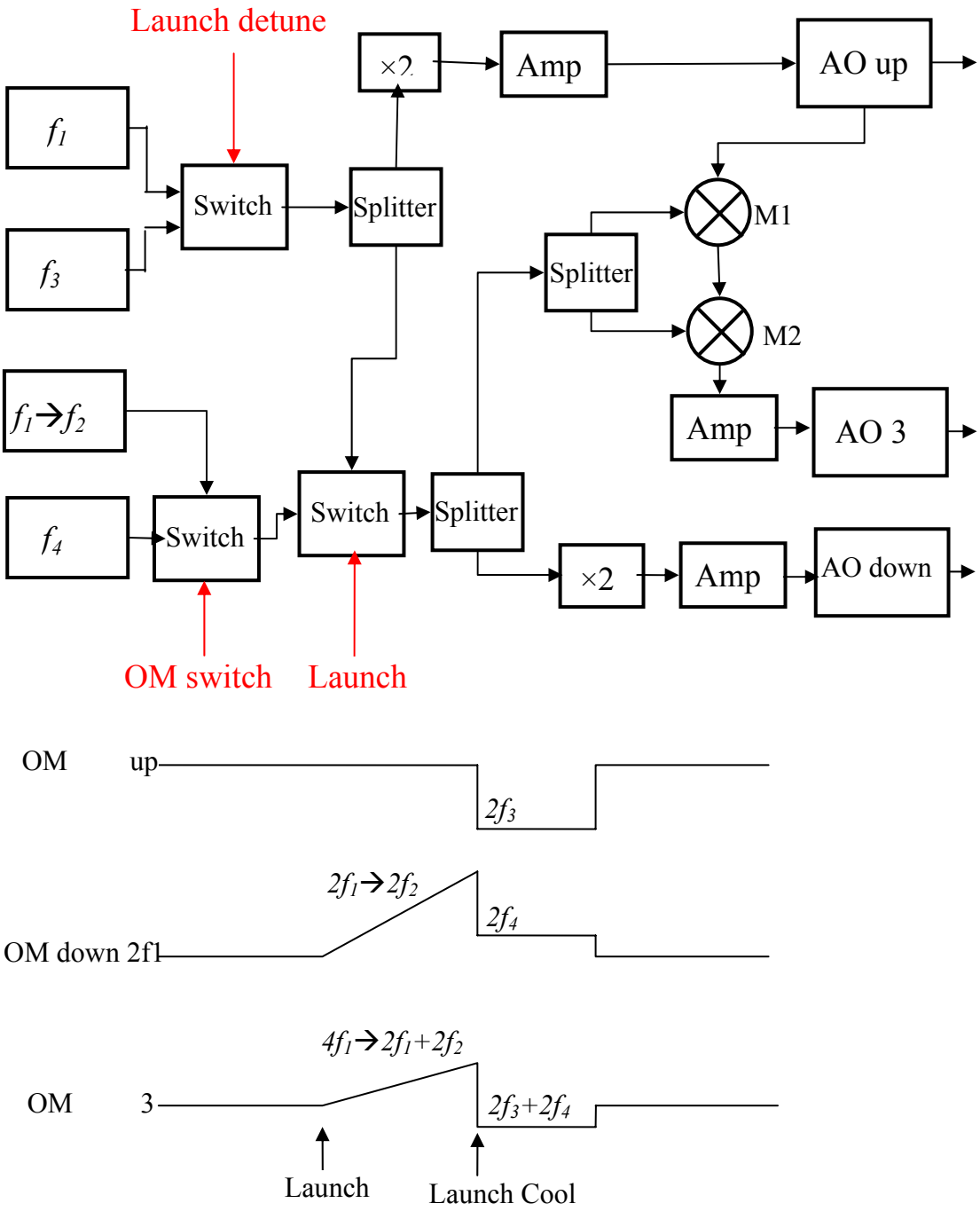

Fig. **5-11**: Schematic of OM beams frequency control. The launch detune, OM switch and launch signal come from the timing board. The down beam's AO frequency sweeps to $2f_2$ in 0.95 ms to change to the moving frame. The repetition rate for the sweeping is 1000 Hz. All 4 synthesized function generators are phase locked together on their rear panels. (RF switch is Minicircuit ZYSW, RF power splitter is Minicircuit ZFSC)

After the frequency sweeping, the OM detuning changed to ($2f_3$, $2f_4$, $2f_3+2f_4$), with the difference between f_3 and f_4 is the same as f_1 and f_2.

5.3.2. Transfer atoms into 1D optical lattice

The resonator enhanced 1D optical lattice is kept on all the time. It does not affect atoms loading into the MOT. The number of atom that remains in the lattice after the MOT is turned off depends on the relative size of the MOT and the lattice beam, the overlap between them, the atom temperature and the trap depth. To get a good overlap of the lattice with the MOT, a F=4 to F'=4 depumping laser is applied first from the top of the vacuum chamber. It propagates in the vertical direction (checked with a plumb bob) and aligned with the MOT. The lattice beam is aligned to overlap with this beam first. We measure the number of atoms left in the lattices after the molasses beams turned off. The MOT position is fine tuned in the z direction by the MOT anti-Helmholtz coils and in the x direction by the bias Helmholtz coils. Pictures of the atoms are taken from 2 directions during the MOT, and 100 ms after atoms are released into the lattices. The MOT and the lattice are overlapped within 50 μm. The conditions for the optical molasses beams are examined again. The number of atoms left in the lattice after 100 ms vs. the OM beams' detuning for different beam's power is shown in Figure **5-12**.

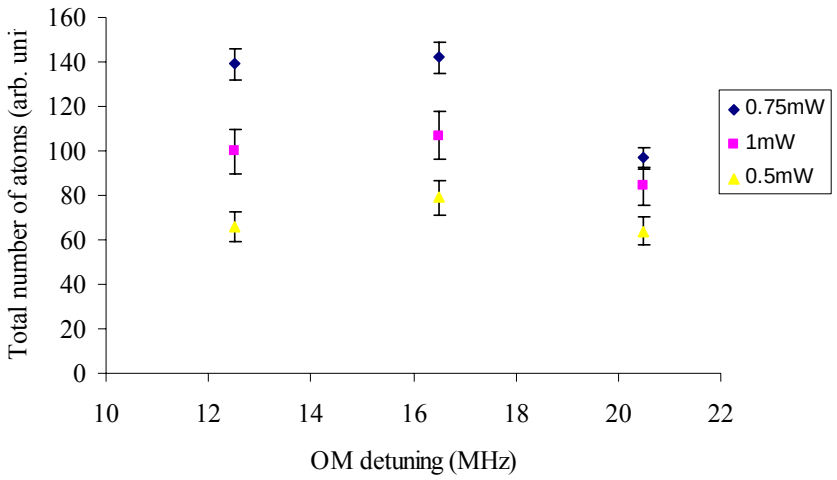

Fig. **5-12**: Number of atoms left in lattices after 100 ms vs. the OM beam detuning and duration. The optimal detuning is about 17 MHz, different from the free space measurement.

Different from the free space optical molasses cooling, where the atom's temperature is decreased when the molasses frequency detuning increased and become flattened at a detuning of 25 MHz, in the lattices, the best cooling condition is 17MHz detuning with the beam power of 0.38 mW. The atom's storage time in the lattice is also measured and shown in Figure **5-13**.

The number of atoms left in the lattice does not exponentially decay. The loss of the number of atoms is larger at short times range, while the density decays almost exponentially, which indicates that the loss in the first 100 ms is dominated by the mode mismatch between atoms and the 1D lattice. The atoms close to the edge are not trapped in the lattice efficiently and are lost faster, so the size of atom cloud decreases in the first 10 to 20 ms.

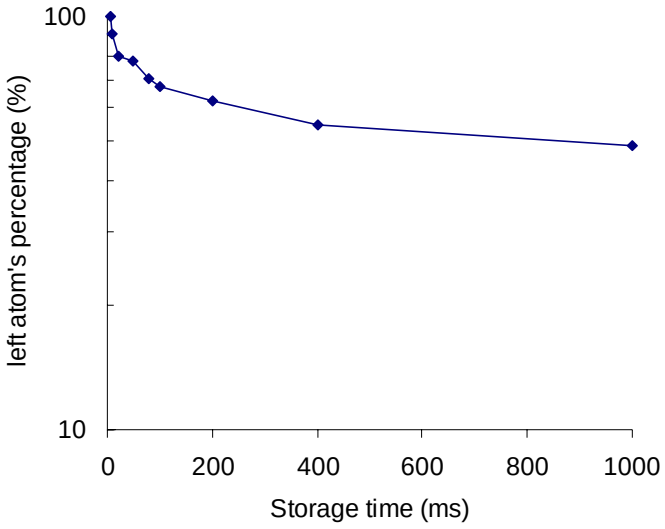

(a)

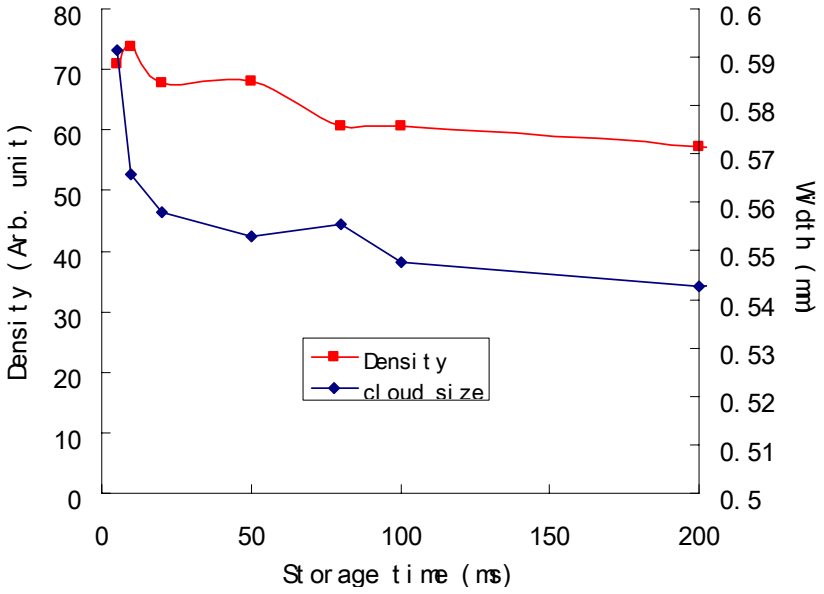

(b)

Fig. **5-13**: Atoms' signal at different storage time. (a) Atom's number percentage left in the lattice at different storage time. (b) Density and atom ball size changes at different storage time.

5.3.3. Resonator enhanced 1D optical lattice guide

In our experiment, atoms are launched 90 cm above the MOT while guided by the 1D lattice. In order to have large transport efficiency, the trap depth has to be deep and the laser linewidth needs to be narrow to avoid heating of atoms. Resonators which can enhance the laser power while keeping the linewidth the same are suitable for this purpose. They have been used to enhance trap laser intensity in order to increase the coupling of the atoms to the light field in some experiments [79, 87].

In our experiment, we use the same 1D lattice trap to guide atoms during the launch and to trap atoms in the measurement region. After the frequency sweeping, the detuning is changed from 13 MHz (red of the Cs F=4 $\rightarrow$ F'=5 transition) to 17 MHz, and the molasses beam intensities are reduce from 8 mW/cm^2 to 0.4 mW/cm^2 to lower the temperature in the moving frame further. After 0.5 ms of low intensity OM cooling in the moving frame, the molasses light is shut off.

The launch direction is determined by the orientation of the molasses beams. The bisecting line of the angle between 2 pairs of diagonal optical molasses beams needs to be in the vertical direction, and the horizontal optical molasses pair needs to be perpendicular to this line. To get a good alignment, the initial velocity is set to 0.5 m/s (the frequency of the f_1 is 28.115 MHz, the frequency of f_2 is 28.335 MHz) first and increased to 4.4 m/s gradually. With the 1D lattice on all the time, atoms are launched up, reach the top of their trajectory and dropped back again. A fluorescence signal from atoms is taken when they pass through the molasses beams. The alignment of these beams is adjusted to find the maximum drop signal. The higher the initial velocity is, the more sensitive the alignment. For the 4 m/s launch, the signal drops about 10% for a 5

mrad change of alignment.

To launch the atoms to the measurement chamber, the initial velocity is set to 4.4 m/s. In the vertical direction, atoms kinetic energy is much larger than the trap potential depth. When they move up, they feel a time-averaged potential. It does not change their trajectory locally. In the horizontal direction, their kinetic energy is smaller than the averaged potential, so they are guided. Atoms experience the time averaged transverse guiding potential from a depth of 60 μK near the MOT to 100 μK near the cavity center.

The transverse radius of the atom distribution at launch time is 900 μm (FWHM). It is not primarily determined by the final temperature, but by the repulsion from photon rescattering before and during the atom's acceleration. Shelving atoms in dark states, which can be used to minimize rescattering, compromises atom acceleration. An atom's initial transverse energy depends on its transverse position, so the dependence of the transverse size on density limits the number of atoms in each launch.

The atom's target destination at the center of the up glass chamber is 90 cm above the MOT, 7 cm short of the top of their trajectory. We observe the atom distribution in this region by pulsing on a high intensity resonant fluorescence beam about 300 ms after launch. The scattered light from the atoms are imaged on a CCD camera to measure the radius of atomic distribution, and on a 5 cm linear photodiode array to measure the length in vertical direction. The radius of the atom distribution is 0.23 mm and its length is 20 mm (FWHM, see Figure **5-14**).

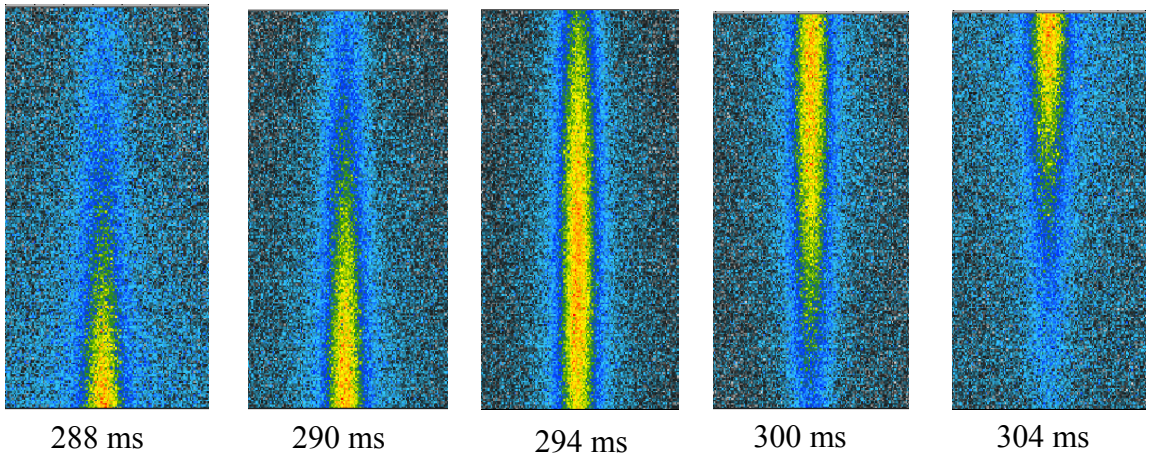

(a)

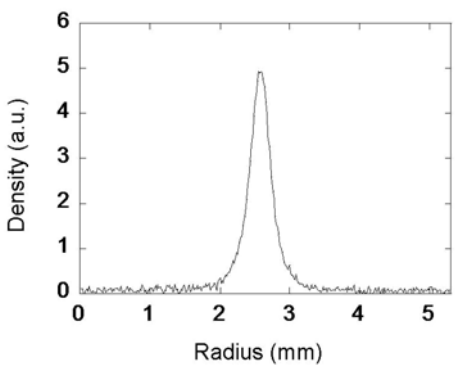

(b)

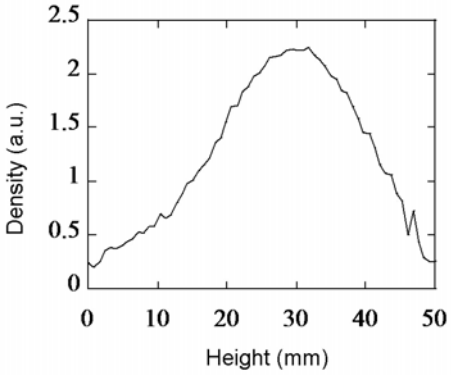

(c)

Fig. **5-14**: Image of the atoms in the upper trapping region. (a) Atoms' image on CCD camera at different time. The vertical cloud size is much larger than the field of view. (b) The horizontal atom distribution. The signal is the average over 50 pixels (about 1 mm) in the vertical direction. (c) The vertical atom distribution. This measurement was made with a linear photodiode array.

The number of atoms that reach the upper region depends on the guide depth as shown in Figure **5-15**. At full lattice intensity, η =50% of the atoms in the MOT reach the upper region. Of the 50% of atoms that are lost, 30% are not guided all the way, 40% are not initially trapped in the lattice, and 30% are lost to background gas collisions.

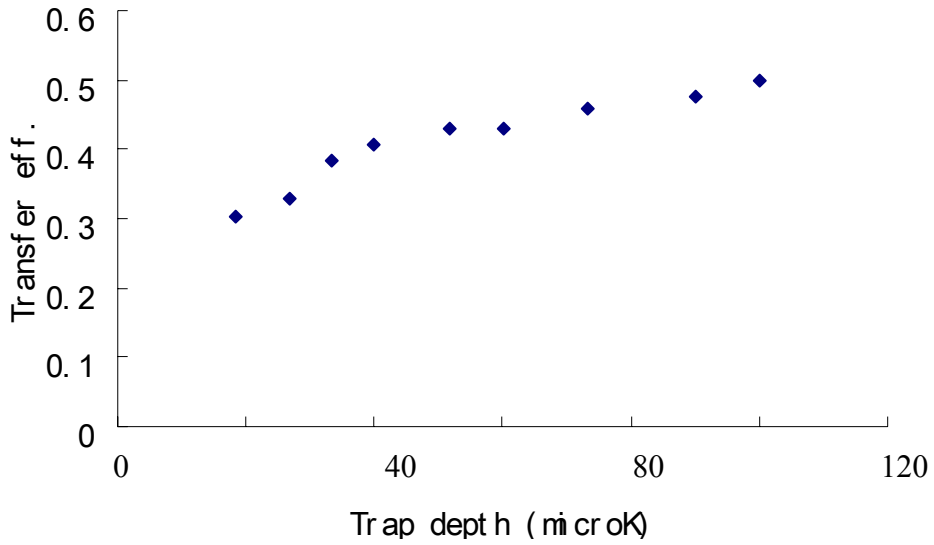

Fig. **5-15**: The transfer efficiency, η, as a function of trap depth.

5.3.4. Stop atoms and trap in the 1D optical lattice

When the atoms reach the target region, we turn on a set of optical molasses beams to stop and re-cool them in the 1D optical lattice traps. In the vertical direction, stopping is accomplished by a 200 μs pulse, with subsequent 1 ms cooling with 2 pairs of horizontal OM beams at intensity of 0.3 mW/cm^2 per beam and a vertical OM pair with 1.5 mW/cm^2 per beam (The intensity of the horizontal beam is limited by the laser power coupled in fibers. The vertical beams is nearly along the lattice, may require higher intensity) .

To undo transverse spreading, we next let atoms freely evolve in the lattice for 6 ms, during which time they collapse to the center. Then we turn the molasses lights back on for 1 ms, at which point the radius of the distribution is 230 μm. A second iteration

further reduces the radius to 210 μm. Figure **5-16** shows the atom's width changing with cooling step. From this figure, we can see that after 2 cooling procedures, the atomic cloud size does not reduce much more.

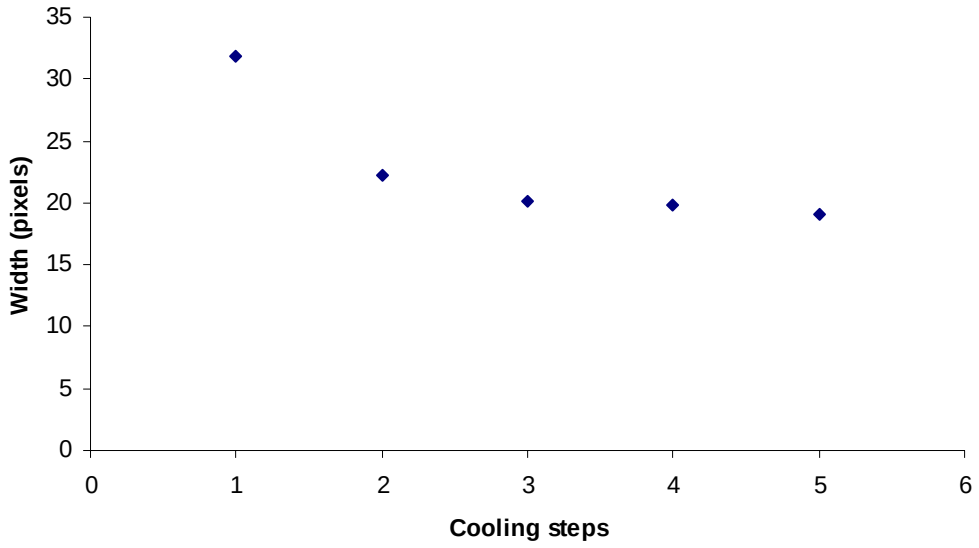

Fig. **5-16**: Atom's width vs. cooling steps. The width drops for the first few cooling steps and then cam to a constant.

The atoms lifetime in the measurement region was also measured with the different trap depths. The results are shown in Figure **5-17**. At different trap depths, the initial number of atoms can be captured by the lattice are different, but the lifetimes are same. Also, in both cases, the numbers of atoms left exponential decay, which suggests that the lifetime is limited by one body collision with the background gas. The lifetime is about 1.7 seconds. (We had a small leak in the MOT coil connection, which became worse and worse.)

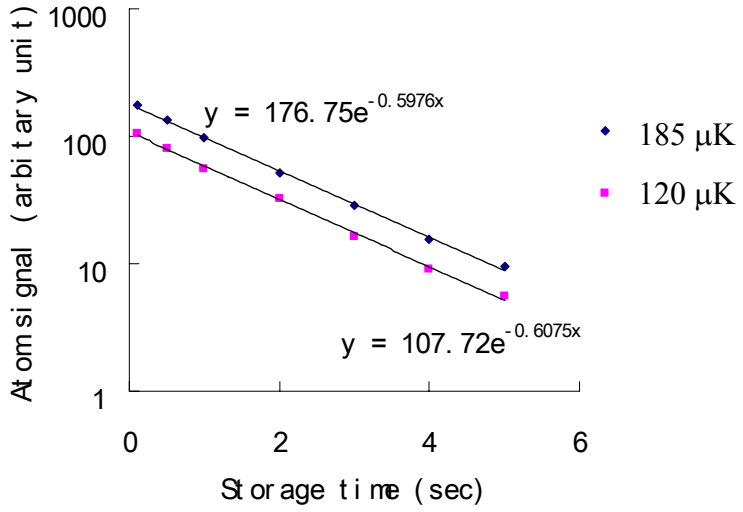

Fig. **5-17**: Atoms lifetime measurement in the up chamber under different trap depth.

5.3.5. Atoms heating in the lattice

After atoms are trapped in the lattice, the lattice noise can heat the atoms. If the original atoms' width is small (If the atom distribution is larger, close to the trap edge, the atoms near the edge can be easily kicked out of the trap, takes away high energy, which is evaporative cooling. In this case, instead of increase the width, heating will cause atom loss). The average potential energy of atoms in the dipole trap:

$$\langle U \rangle = U_0 \cdot \frac{2}{\pi w_1^2} \int_0^{\infty} \int_0^{2\pi} (1 - e^{-2\frac{r^2}{w_0^2}}) e^{-2\frac{r^2}{w_1^2}} r d\theta dr = U_0 \frac{w_1^2}{w_1^2 + w_0^2}, \qquad (5.11)$$

where w_1 is the atomic distribution size and w_0 is the lattice beam size. In the harmonic trap, the average kinetic energy equals the average potential energy. The trap laser beam size is 0.63 mm, the atom cloud size is shown in Figure **5-18.** The atomic distribution

is about one third of the lattice size. The average kinetic energy is calculated from the atomic density distribution to get the kinetic energy distribution. At r=0.24mm, the averaged kinetic energy is only about 5% less than the potential energy (difference), so the total energy is about twice of the potential energy.

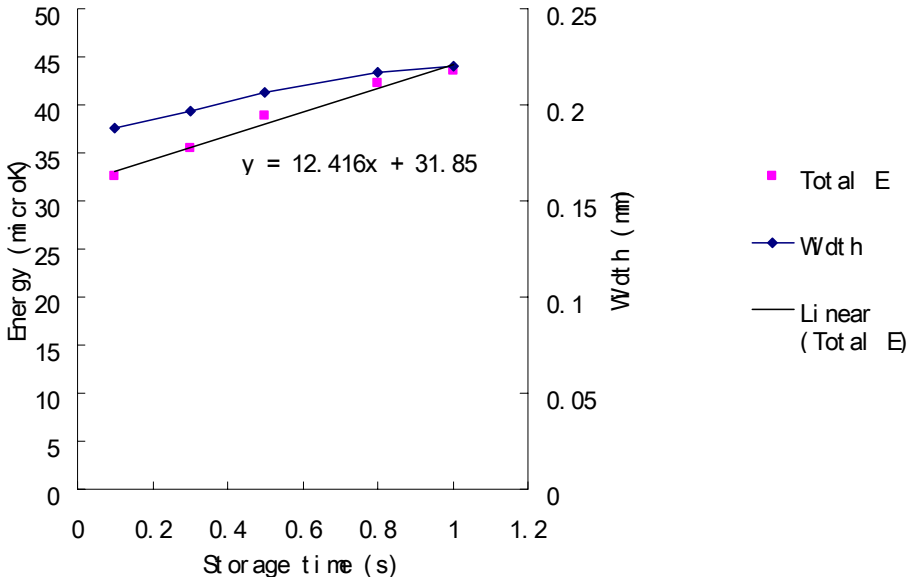

Fig. **5-18**: Atoms heating in the lattices

The data are taken with a trapping potential of 200 μK. The heating rate is about 12 μK/s. If the energy increases as $E \sim E_0 \exp(t/\tau)$, the energy e-folding time is 2.6 s.

5.4. Multiple loading atoms to the interaction region

We can reload the MOT while atoms are in transit to the upper region, starting 15 ms after each launch. By varying when the up molasses is turned on, we can stop atoms at different positions along the 1D lattice, making the effective volume of the trap in the

up region quite large.

5.4.1. Multiple launching

The vertical cooling beam has a small angle relative to the 1D lattice, so that it overlaps with the lattice for a long distance. When one group of launched atoms reach the center region and needs to be stopped and trapped, the next group of launched atoms should be far enough away that they are not illuminated by the cooling beam as shown in Figure **5-19.**

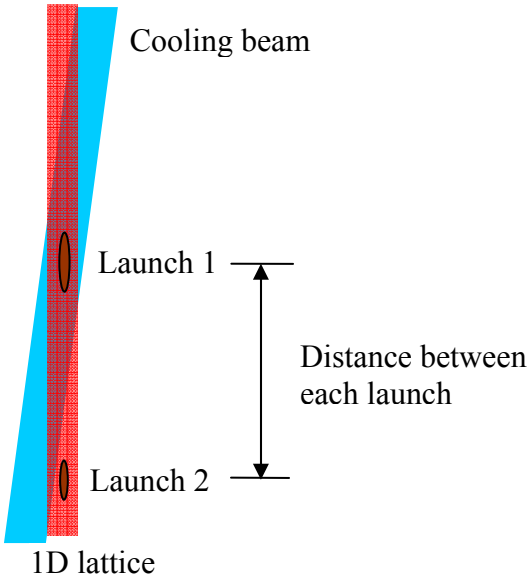

Fig. **5-19**: Multiple launchings

The maximum re-launching rate is decided by the overlap of the 1D lattice beam and the cooling beam. The atomic signals launched to the top are measured, and vertical

cooling beams are turned on for 2 ms at different times during the atoms launch. The results are shown in Figure **5-20**:

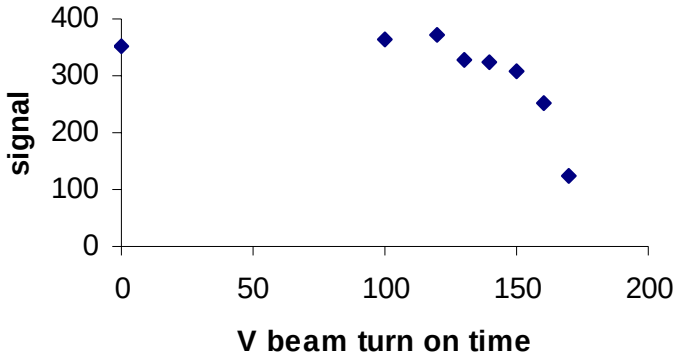

Fig. **5-20**: Vertical beam effects at different time.

The time in Figure **5-20** is between the launch and when the vertical molasses beams are turned on. Before 120 ms, atoms have not reached the overlapped area where they can be pushed away by vertical optical molasses beams, but for longer times, the signal decreases dramatically. It takes 330 ms for the atoms to reach the measurement region, so the minimum repeat period is 210 ms.

5.4.2. Multiple loading to one place

By repeatedly running the same sequence, the atoms can be loaded into the same place. The maximum number that can be loaded into the lattice trap is then determined by the loss and loading rate. The loss includes vacuum loss and photo-associative collision loss.

a. Loss coefficient

The lifetime is measured independently, is about 1 second (vacuum is worse than before). By 160 ms MOT load each time, 10 loads to the measurement region data are shown in Figure **5-21**. The theoretical calculation of the number of atoms loaded into the measurement chamber can be found by assuming that the vacuum loss is the only loss. That result is also shown in Figure **5-21** for comparison.

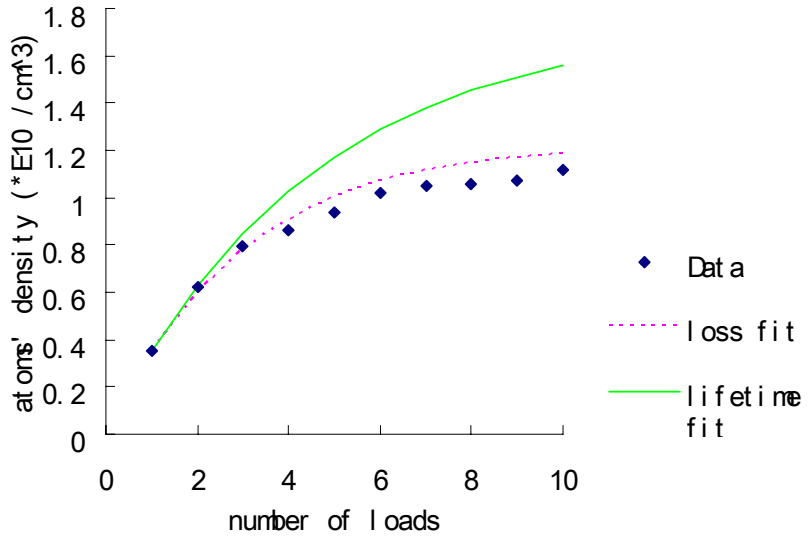

Fig. **5-21**: The atom's peak density for 10 launches. The blue dots are the data. The green line is the numerical result for just including the loss due to the lifetime. The pink dashed line is the result including both lifetime loss and photo-associative loss.

The disagreement between the experimental data and the lifetime fit data suggests that there are some other loss mechanisms. In this procedure, the only possible loss is due to photo-associative collisions, which happens while cooling. It is a two body effect. The loss rate is expressed as follow:

$$\frac{dn}{dt} = -\Gamma n - \beta n^2 \qquad (5.12)$$

where Γ is the one body loss coefficient (vacuum loss), β is the two body loss coefficient. To get β, we load different numbers of atoms into the lattice and then turn on the cooling procedure 5 times in 160 ms. We then measure the number of atoms left in the lattice. With the approximation, equation 5.12 can be expressed as:

$$\frac{n_f - n_0}{T} = -\Gamma \frac{n_0 + n_f}{2} - \beta \frac{n_0^2 + n_f^2}{2}$$

$$\rightarrow \frac{2 \cdot (n_f - n_0)}{T \cdot (n_0 + n_f)} = -\Gamma - \beta \frac{n_0^2 + n_f^2}{n_0 + n_f}, \qquad (5.13)$$

where n_0 is the initial atom's density, n_f is the final atom's density, T is the total time 0.16 ms. The data are shown in Figure **5-22.**

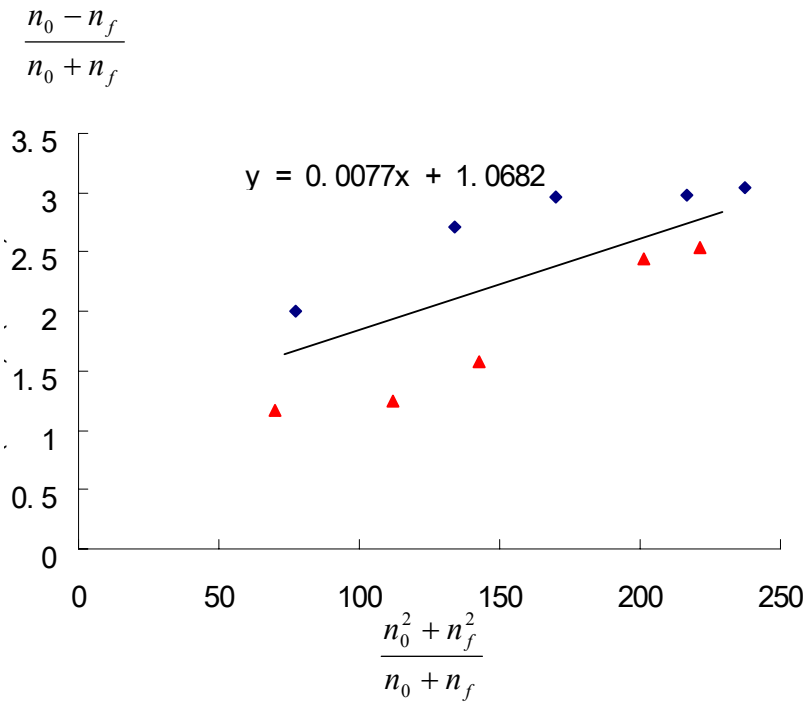

Fig. **5-22**: The atoms density after 5 cooling procedures with different initial density. The two data sets are two independent initial density measurements. The blue one is the initial density measured directly, and the red one was gotten by trapping atoms for 200 ms, and using the average lifetime to calculate the initial density.

The n_0 and n_f are densities with a unit of (data reading from CCD camera/ one pixel). To convert it into the atoms/cm^3, we calibrate that 175 unit = 7×10^9 atoms/cm^3. The density is obtained by: $n = \frac{2\sqrt{2}\cdot N}{\pi\sqrt{\pi}w_0^2\cdot w_l}$, where N is the total number of atoms, w_0, w_l are the width and the length of the atoms cloud respectively. From Figure **5-22**, we can get that $\Gamma \sim 0.93$ s^{-1}, which is close to the independent lifetime measurement of 1 s. With 5 cooling procedures in 0.16 seconds, we get $\beta_{pc} = 0.71\times10^{-11}$ (atoms/cm^3)$^{-1}$ per cooling. With this β_{pc} and Γ_{pc} per cooling fit to the 10 loads data, we can get the atoms density for 10 loads. The result is also in Figure **5-21** as pink dotted line. It is very close to the real data.

b. Total number of atoms can be loaded into the glass chamber

The maximum number of atoms that can be loaded into the lattice depends on the loading rate. At low MOT size and density, the transport to the measurement chamber efficiency is about 50%. Increasing the MOT loading rate not only increases the density, but also the size of the MOT. Figure **5-23** shows the atom number and density changing as the MOT loading time is increased.

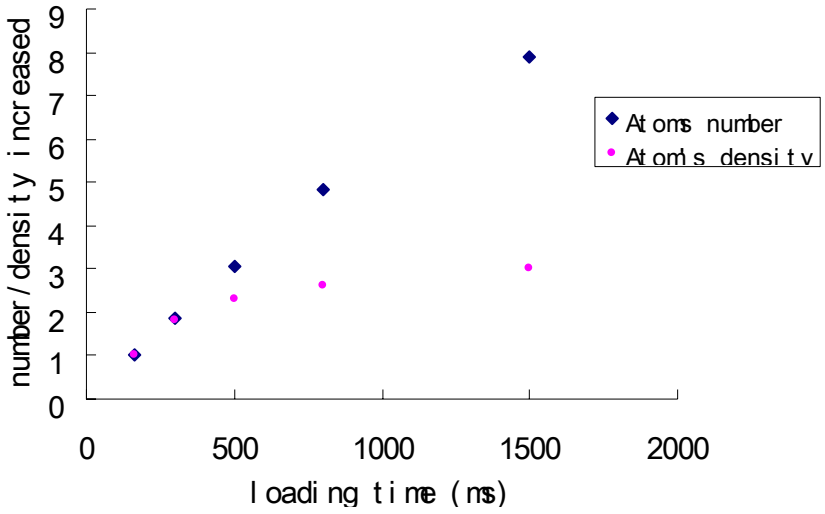

Fig. **5-23**: The atom's number and density increased vs. the loading time.

We can see that when the total number of atoms is linearly increased by a factor of 8 in 1.5 seconds MOT loading, the density is almost saturated, only increasing by a factor of 3. The densities of the atoms transported to the measurement chamber are also measured, and the result is shown in Figure **5-24**.

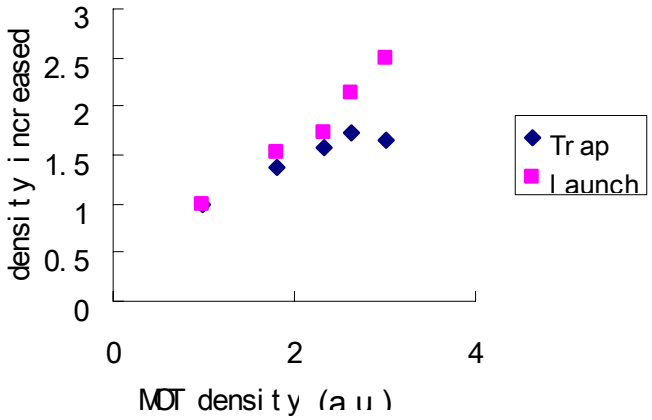

Fig. **5-24**: The density of the atom cloud near the measurement region compared with the density of atoms trapped by the lattice directly without launching as a function of

MOT density.

While the MOT density increased by a factor of 3 (of 160 ms load) by increasing the loading time, the transported atom's density increased 2.5 times, almost linearly, while the atoms trapped by the lattice near the MOT is only increased by less than a factor of two. The MOT density is so high that when MOT is off, the atoms are trapped in the lattice, and the two-body loss is large. When atoms are launched up, they spread in the vertical direction, so the density decreases and the two-body loss becomes negligible. Therefore the transported atom density increased proportional to the MOT density.

From the above results, we can see that the peak density starts to saturate after 500 ms. The total number of atoms at 1.5 second loading time is 0.8×10^8 atoms. The number of atoms that can be transported to the top is: $0.8\times10^8\times50\%\times\frac{2.4}{7.9}=0.12\times10^8$ atoms. The factor 2.4/7.9 results because when the MOT number is increased 7.9 times, the total number transported to the measurement chamber is only increased 2.4 times. That is, the transport efficiency is decreased by a factor of 7.9/2.4 compared to the low density launching (160 ms MOT loading time, 50% efficiency).

The atom density per launch near the measurement region is:

$$\frac{N}{\frac{\pi\sqrt{\pi}}{2\sqrt{2}}w_0^2\cdot w_l}=\frac{0.12\times10^8}{0.0018cm^{-3}}=0.67\times10^{10}\,atoms/cm^3 \qquad (5.\ 14)$$

The maximum density (n) that can be reached in the measurement region can be found by setting the loss rate equal to the loading rate, which depends on MOT loading

rate (A), MOT loading time ($t_{m,}$), transport efficiency (η), the atoms lifetime (τ) in the lattice and photo associative two body loss (β) during the stop and cooling time. We have:

$$At_m \cdot \eta = \left[(1 - ne^{-\frac{t}{\tau}}) + At_m \cdot \eta \right]^2 \cdot \beta \qquad (5.\ 15)$$

By improving the vacuum, the atoms' lifetime in the lattice trap should be able to improved by a factor of 10. The maximum density that can be loaded into the measurement region at equilibrium is about 3×10^{10} atoms/cm^3. For the staggered cooling, atoms can be spread out over 10 cm in an attentive of the volume about 10 mm^3 with a total number of 3×10^8 atoms, which would meet our goal for Cs atoms.

5.4.3. Multiple loading to a different place

By varying where the cooling beams are turned on, the atoms can be trapped in different positions and so can be spread out over a large distance. The maximum spread out size depends on the horizontal cooling beam size and the detector size. Figure **5-25** shows 3 launches with staggered stop time (325 ms, 337 ms, 355 ms). The atoms are spread out over 50 mm in the vertical direction. The signal is obtained with a photodiode array.

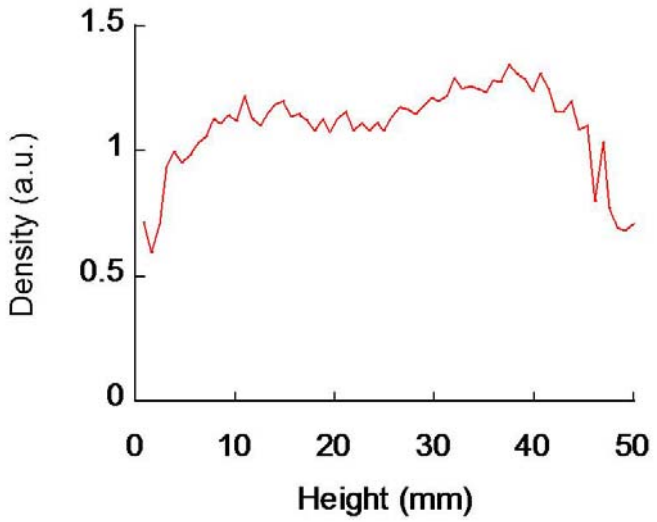

Fig. **5-25**: An example vertical atom distribution after 3 launches with staggered stop times. The 3 launches top molasses cooling beams were on at 355 ms, 337 ms, and 325 ms respectively.

In conclusion, we have demonstrated a 90 cm launch of Cs atoms guided by a one-dimensional optical lattice. The 1064 nm wavelength optical lattice is made in a 2 m long build-up cavity of light, and provides a transverse guide depth of up to 200 μK. Before they reach the top of their trajectory, the atoms are stopped and cooled by optical molasses, becoming trapped in the 1D lattice, which can be loaded with multiple launches. With 10 launches, we can transport 3.5×10^7 atoms to the measurement region in 2 seconds. The atoms can be stretched out over 5 cm by staggering the stop time.

Chapter 6

Summaries and Future work

6.1. Summaries

We have proposed an experiment to search for the electric dipole moment (edm) of the electron using cooled Cs and Rb atoms in 1D optical lattice traps. Our projected sensitivity is 3×10^{-30} e-cm, a 500-fold improvement over the current limit with a coherent time of 3 seconds and integration time of 12 hours. The atoms will be trapped in 2 identical far off resonance 1D optical lattices separated by 10 mm in the horizontal direction, spread out over 10 cm in the vertical direction. We tested the leakage current through the spacer between the copper plates and small ITO coated E field plates in a test vacuum chamber. In steady state, 150 kV/mm electric field can be applied with the leakage current of only about 10 pA. During the high voltage switching, the leakage current drops down to several hundred pA after 1 second charging time, which meets the Cs atoms shot noise limit requirement. A four-layer magnetic shielding system was designed with a shielding factor of 7×10^{7} for the bias field and 7×10^{8} for the gradient field in the ideal case. The B field coils which provide the magnetic field inside the shielding were designed too to cancel the residue field and provide the scan field to get whole Ramsey fringe. We analyzed the statistical noise and systematic errors due to the B fields, E fields and laser-atoms interactions. Both vector light shrift and tensor light shrift are common modes. Tensor light shrift is proportional to the m^2, which will not cause the energy difference in the 2 stretched states. Vector light shrift requires that the trapping

laser beam is linear polarized. Higher order laser atom interactions are proportional to E field and m, it is a systematic error and needs to be controlled.

The system setup is described in detail in chapter 4 including the Zeeman slower, laser and laser locking systems, resonator enhanced 1D optical lattice and the computer controlled system. A 2 meter long FP cavity with enhancement factor about 50 is used as 1D lattice trap to provide the trap depth up to 250 μK. The Cs and Rb atoms were trapped in a Zeeman slower loaded MOT. An optical lattice guided atomic fountain was realized based on launching a cold cloud of atoms using the technique of moving molasses frame. Cs atoms cloud has been shown to be launched up 90 cm from MOT to the center of the measurement chamber while guided by the resonator enhanced 1D optical lattice trap with transport efficiency up to 50%. Before they reach the top of their trajectory, the atoms are stopped and cooled by optical molasses, becoming trapped in the 1D lattice. The loss mechanism during the launch and re-trap the atoms has been tested. We found that the maximum density we could get for the atoms cloud near MOT is about 4×10^{10} atoms/cm^3, increase load more atoms into the MOT only increase the atom cloud size instead of the density. The maximum number of atoms can be transported into the upper chamber and trapped in the lattice is determined by the loss, the loading rate and the cloud size. With 10 launches, we demonstrated transported 3.3×10^7 atoms to the measurement region in 2 seconds. We also show in 3 launches, the atoms stretched out over 5 cm by staggered stop time. For an ideal case, which the loss mechanism is dominated by the photon associative collisions, with atoms spread out 10 cm, 2×10^8 Cs

atoms should be able to transport to the measurement region, which is an important step to prepare atoms for the final EDM measurement.

6.2. Two identical 1D optical lattices traps

We implemented one resonator enhanced 1D optical lattice. For the EDM measurement, the atoms need to be trapped in two identical lattices between E filed plates. The input YAG laser beam will split into 2 beams separated by 10 mm. The beam splitter is an etalon with a certain thickness and special coatings on two surfaces as shown in Figure **6-1**.

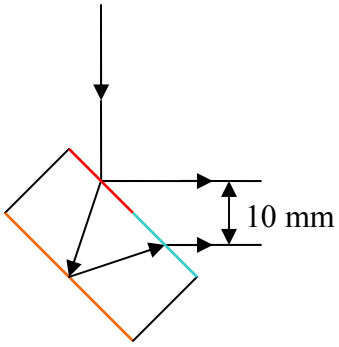

Fig. **6-1**: Etalon beam splitter. Two coatings on the top surface, half is 50% transmission partial reflection coating, half is AR coating. Bottom surface is the HR coating.

The index of refraction for the fused silica at 1064 nm n=1.4496. To get the two beams separation 10 mm, the etalon thickness t is:

$$\left.\begin{aligned} \frac{10/\sqrt{2}}{t} &= \tan\theta \\ n \cdot \sin\theta &= \sin 45^{\circ} \end{aligned}\right\} \rightarrow t = 12.654mm \qquad (6.\ 16)$$

The 4 cavity mirrors are specially cut (we have these mirrors). The lock system for two lattices is shown in Figure **6-2**.

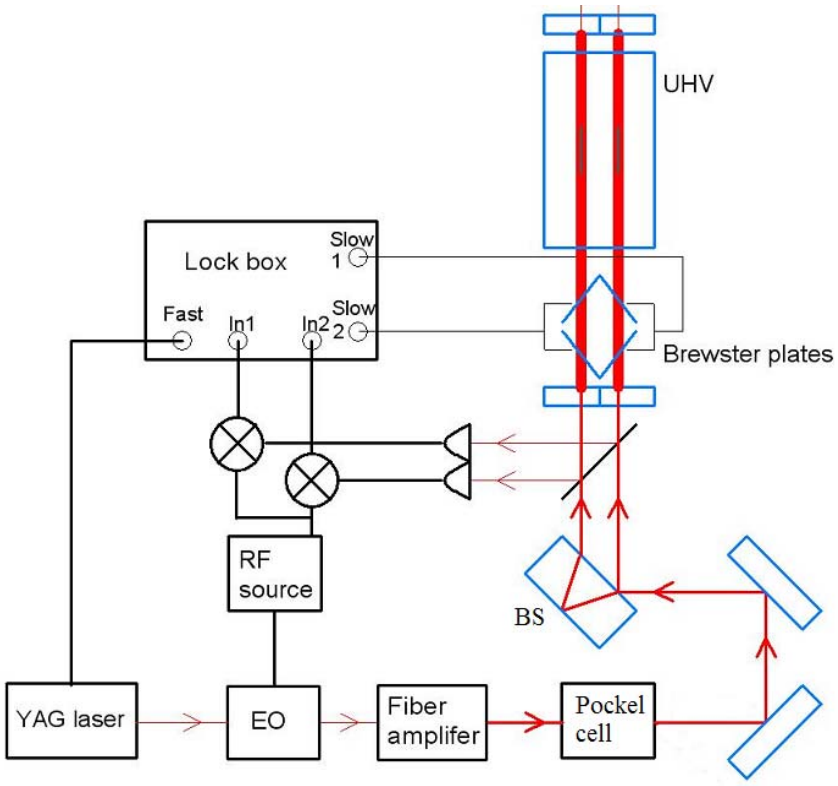

Fig. **6-2**: Diagram of two lattices locking. The YAG laser beam is split into 2 beams by an etalon beam splitter. Two reflection signals from lattices are detected separately and error signals sent to the lock servo circuit. The fast feedback signal is sent to the YAG to lock the laser frequency to the cavity resonance. Two slow feedback signals are sent to 2 pairs of Brewster plates.

The YAG laser beam is split into 2 beams by an etalon beam splitter. Two reflection signals from lattices are detected separately and error signals sent to the lock

servo circuit. Two slow feedback signals are sent to 2 pairs of Brewster plates to lock the cavity resonances to the laser frequency. The fast feedback signal is sent to the YAG laser to lock the laser frequency to the cavity resonance. This locking system requires that the high frequency noises of the two cavities be the same. By mounting 2 cavity mirrors on the same mirror mounts, and fine tune one cavity alignment first. The other cavity alignment can only be tuned by screw. Without using the springs for individual mirrors, the high frequency noise spectrum of these two cavities should be same.

6.3. States preparation

After the Cs atoms are prepared in the lattices, they are evenly distributed in the different F = 4 Zeeman sublevels, and need to be optically pumped to the $|F = 4, m_F = 4\rangle$ state by an optical pumping beam. This can be done by applying a magnetic field along the circularly polarized optical pumping beam. The magnitude of this B field needs to be larger than the pump laser beam AC Starks shift to define the quantization axis. If the incoming laser light is circularly polarized, quantum-mechanical selection rules require that transitions must satisfy $\Delta m = \pm 1$, depending on the circularity of the light (σ^+ for +1 and σ^- for -1). For the optical pumping beam which is σ^+ polarized red detuning to the F=4 → F'=4 transition for Cs atoms, $|F = 4, m_F = 4\rangle$ is a dark state and the atoms will be accumulated in this state by scattering several photons.

The optical pumping light AC Starks shift is:

$$\Delta E_g = \frac{\hbar\delta \cdot s_0 C_{ge}^2}{1 + (2\delta/\gamma)^2}, \qquad (6.\ 17)$$

where δ is the detuning and can be set to 10 MHz, C_{ge}^2 is different for different Zeeman sublevels, the maximum is 7/48. To scatter 10 photons in 2 ms, the saturation parameter needs to be about 1/1000,

$$\Delta E_g = \frac{\hbar\delta \cdot s_0 C_{ge}^2}{1 + (2\delta/\gamma)^2} \sim \frac{2}{17} \cdot \frac{1}{1000} \cdot \frac{7}{48} \hbar\gamma \sim 0.09kHz, \qquad (6.\ 18)$$

The energy difference between Zeeman sublevel $|F = 4, m_F = 0\rangle$ and $|F = 4, m_F = 4\rangle$ at 1 mGauss B field is 1.4 kHz. A few mGauss magnetic field is large enough for an efficient optical pumping.

The optical pumping beam is close to the vertical direction. To rotate the quantization axis along the Z direction, the magnetic field direction needs to rotate to the y direction slowly so the atoms quantization direction will adiabatically follow to the z direction, and then the magnetic field is turned off while the electric field is switched on to define the quantization axis. The time for rotating the magnetic field needs to be much longer than the atomic procession time along magnetic field. The procession period under B field for $|F = 4, m_F = 4\rangle$ state is [1]:

$$T = \frac{L_{am} \sin\theta}{2\pi\tau_{torq}} = \frac{\sqrt{F} \cdot h}{2\pi \cdot g\mu_B \cdot m \cdot B} = \frac{\sqrt{4}}{2\pi \cdot 1.4 \times 10^{-3}} = 0.22ms, \qquad (6.\ 19)$$

where L_{am} is the total angular momentum and τ_{torq} is the torque under the 1 mGauss magnetic field, θ is the angle between total angular momentum and the B field direction.

After the atoms are prepared in the $|F=4, m_F=4\rangle$ state, they will be transferred to $|F=4, m_F=0\rangle$state by 4 different frequency π pulse microwave ($\Omega \cdot t=\pi$, states: $|F=4, m_F=4\rangle \rightarrow |F=3, m_F=3\rangle \rightarrow |F=4, m_F=2\rangle \rightarrow |F=3, m_F=1\rangle \rightarrow |F=4, m_F=0\rangle$). Assuming each π-pulse duration time t is about 5 ms, the RF pulse line width is about 32 Hz, much less than the Zeeman level energy splitting under 1 mGauss magnetic field. The Rabi frequency of the π-pulse $\Omega = \frac{\mu B}{\hbar} = 3.14 kHz$. The magnetic field needed to generate these π-pulses is about 0.25 mGauss.

The electric magnetic field intensity of these RF pulses is:

$$S = E \times H = \frac{B^2}{\mu_0 \sqrt{\mu_0 \varepsilon}} \sim 0.6 W/m^2, \qquad \mu_0 = 4\pi \times 10^{-7} \tag{6. 20}$$

Our microwave horn will be put 30 cm away from the atom cloud. Under the electric dipole fields and radiation approximation, the angular distribution is [2]:

$$\frac{dP}{d\Omega} = \frac{Z_0 I_0^2}{128\pi^2} (kd)^2 \sin^2 \theta \tag{6. 21}$$

And the total RF power is:

$$P = \frac{Z_o I_0^2 (kd)^2}{48\pi}, \tag{6. 22}$$

where $Z_0 = \sqrt{\mu_0 / \varepsilon_0}$, $I_0^2/2$ is the radiation resistance of the antenna. For the short center feed antenna ~$5(kd)^2$ ohms. From equation 6.5 and 6.6 , we have,

$$S = \frac{dP}{ds} = \frac{dP}{R^2 d\Omega} = \frac{Z_0 I_0^2}{128\pi^2 \cdot R^2} (kd)^2 \sin^2 \theta = \frac{48}{128\pi \cdot R^2} \cdot P \sin \theta \tag{6. 23}$$

The power radiated by the antenna P must be 0.5 Watts.

Atoms will be spread out 10 cm in the vertical direction, it is very important for the atoms feel roughly same RF power, so that undergo a full transition. The electrical magnetic field intensity 5 cm away from the center of the atom's cloud is 0.97 of the cloud center RF intensity.

$$\theta = \tan^{-1}\frac{5cm}{30cm} = 9.5^\circ \rightarrow \quad \sin^2(90 - 9.5) = 0.972 \qquad (6.\ 24)$$

6.4. EDM measurement

The EDM signal will be measured under the electric field. To get down to the projected sensitivity, the number of atoms that can be loaded into the measurement chamber should be increased by an order magnitude from the current 3.3×10^7 Cs atoms to $(2\sim3)\times10^8$ Cs atoms. Improving the Zeeman slower rate by a transverse cooling before slower, improving the vacuum pressure by fixing the leak first, adding another TSP and bake the system, increasing the maximum launching density by playing parameters of optical molasses beams cloud will help to meet this requirement. The slow charging time constant for the ITO coated plates is relatively high; a better coating could possibly reduce it.

There are still some open questions. First is the magnetic field stability. The outside magnetic field fluctuations could be monitored by magnetic sensors. The data can be used to feedback the 3 pairs of the cancellation coils to stabilize it. The detailed information about how the field changes in space in the atom cloud could be obtained by the atom's Zeeman spectroscopy, particularly about dBz/dz and dBx/dz=dBz/dx.

Measured Zeeman shifts can be used to cancel gradients using simple coils just inside the inner magnetic shield.

The second is the lD lattice beam balance. Because the space is limited, the Brewster plates are put on the top of the vacuum chamber, which induces 0.4% imbalance of the lattice beams, the vacuum chamber also adds another 0.2% imbalance. If this systematic error limits by the higher order laser atom interaction, this has to be improved.

1. 2004 [cited; Available from: http://www.physicsforums.com/archive/index.php/t-19095.html.
2. Roald K. Wangseness, Electromagnetic fields, John Wiley & Sons, 1979.

Appendix

A. 'V' shape 3 levels transition

3-level system: $\sigma_x = \begin{pmatrix} 0 & 1 & 0 \\ 1 & 0 & 1 \\ 0 & 1 & 0 \end{pmatrix}$, $\sigma_y = \begin{pmatrix} 0 & -i & 0 \\ i & 0 & -i \\ 0 & i & 0 \end{pmatrix}$, $\sigma_x = \begin{pmatrix} 1 & 0 & 0 \\ 0 & 0 & 0 \\ 0 & 0 & -1 \end{pmatrix}$.

At t = 0, atom is in the superposition state: $\frac{1}{\sqrt{2}} \begin{pmatrix} e^{\frac{-i(\eta_B \mu g B + \eta_E E d)\tau}{\hbar}} \\ 0 \\ e^{\frac{+i(\eta_B \mu g B + \eta_E E d)\tau}{\hbar}} \end{pmatrix}$, and then

Apply electromagnetic pulse $B_x = b\cos\omega t$, the perturbation Hamiltonian is:

$$H' = \begin{pmatrix} 0 & b\cos\omega t & 0 \\ b\cos\omega t & 0 & b\cos\omega t \\ 0 & b\cos\omega t & 0 \end{pmatrix}, \text{ and } H_0 = \begin{pmatrix} \omega_1 & 0 & 0 \\ 0 & 0 & 0 \\ 0 & 0 & -\omega_1 \end{pmatrix}.$$

$$\left.\begin{aligned} H|\psi\rangle &= i\hbar \frac{d|\psi\rangle}{dt} \\ |\psi\rangle &= a_1|\phi_1\rangle + a_0|\phi_0\rangle + a_{-1}|\phi_{-1}\rangle \end{aligned}\right\} \Rightarrow i\hbar \frac{da_m(t)}{dt} = \sum_n a_n(t) H'_{mn} e^{i\omega_{mn}t}$$

And we have:

$$\begin{cases} i\hbar\dot{a}_0 = a_1 b\cos\omega t \cdot e^{i\omega t} + a_{-1} b\cos\omega t \cdot e^{i\omega t} \\ i\hbar\dot{a}_1 = a_0 b\cos\omega t \cdot e^{-i\omega t} \\ i\hbar\dot{a}_{-1} = a_0 b\cos\omega t \cdot e^{i\omega t} \end{cases}.$$

If the applied electromagnetic pulse is a π pulse and coherent pump atoms to the m=0 state. After this pulse, the state is:

$$\begin{pmatrix} \frac{-i}{\sqrt{2}}\sin(\frac{\eta_B\mu_B g_F m_F B+\eta_E E d_a}{\hbar}\cdot\tau) \\ \cos(\frac{\eta_B\mu_B g_F m_F B+\eta_E E d_a}{\hbar}\cdot\tau) \\ \frac{i}{\sqrt{2}}\sin(\frac{\eta_B\mu_B g_F m_F B+\eta_E E d_a}{\hbar}\cdot\tau) \end{pmatrix}.$$

B. Computer controlled diode laser locking

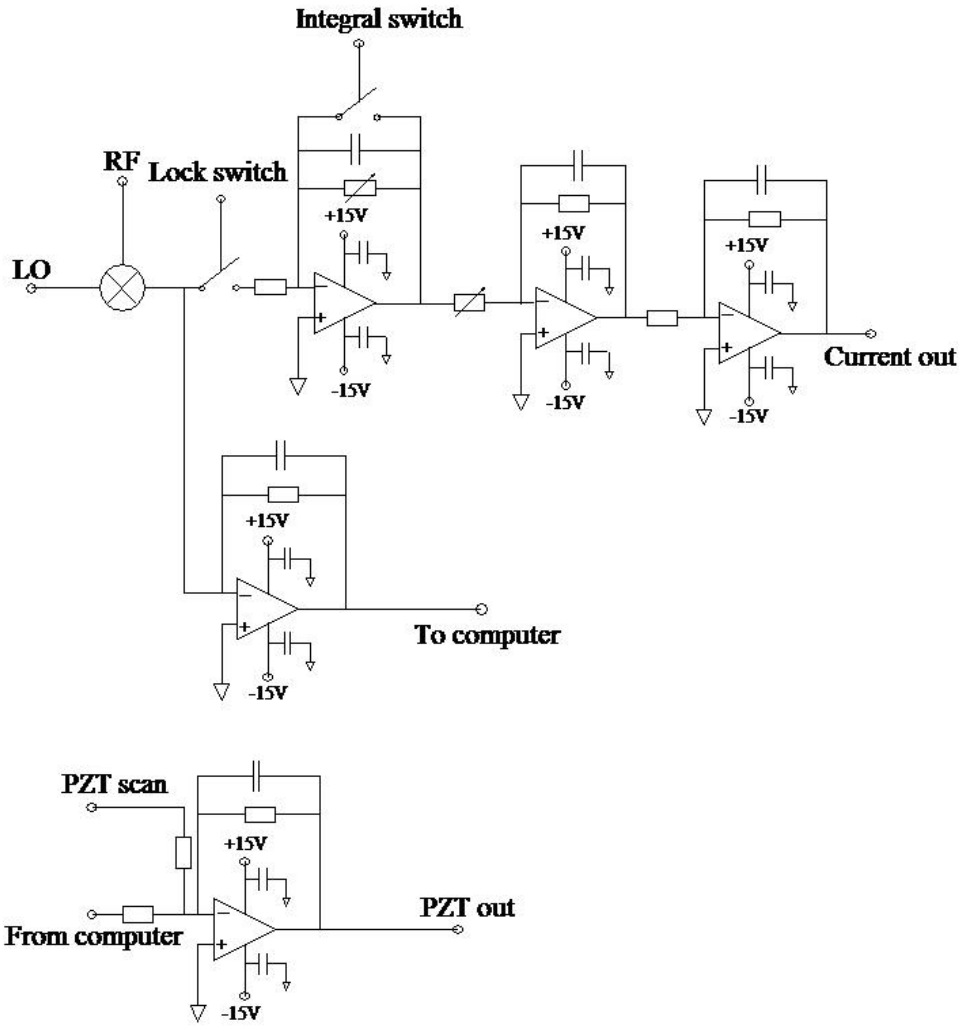

Fig. B1 Circuit diagram for the computer laser lock system

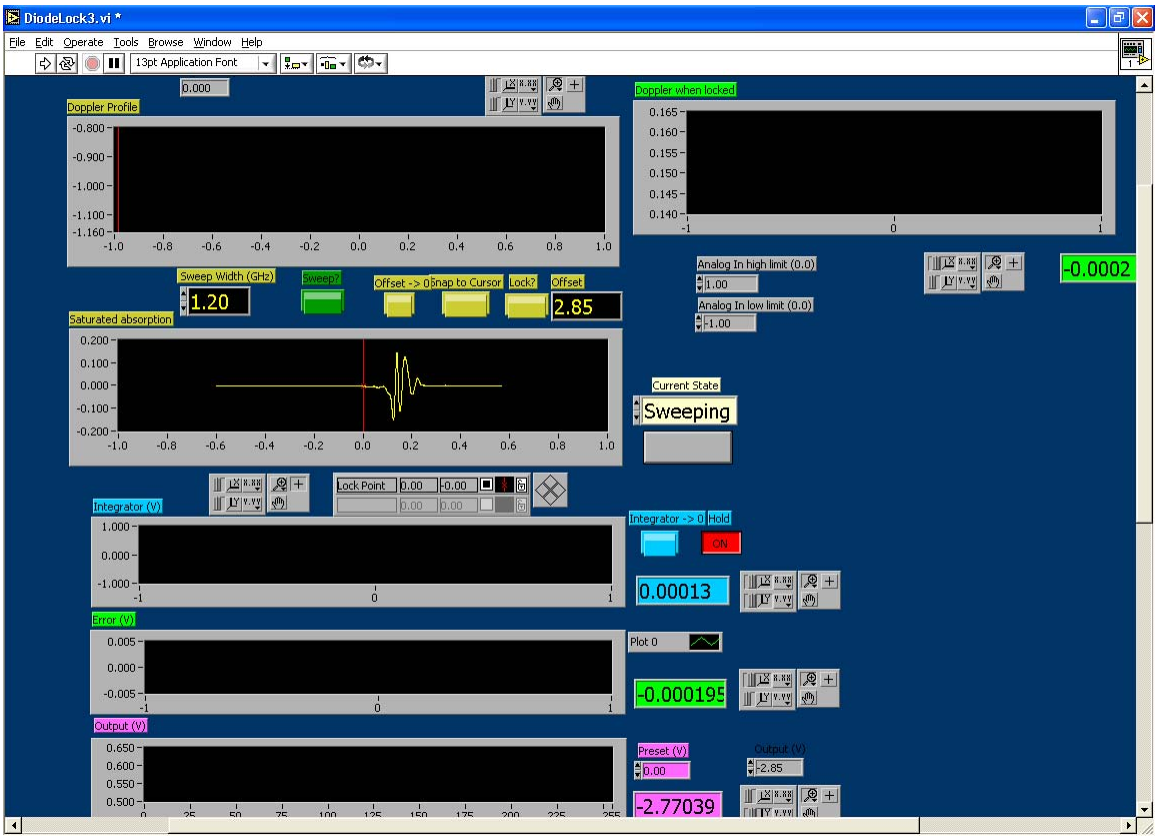

Fig. B2 Front panel of Labview program to lock the laser

The card for the computer locking is NI PCI 6036E data acquisition card. The signal from the photodiode is sent to both the computer Doppler profile input to monitor the signal and to the lock servo circuit RF input. The error signal from the mixer is sent to the computer to do the integral in the low frequency range. Feedback signal from the computer is sent PZT through the servo circuit. The high frequency feedback signal from the circuit is sent to the laser current control. The Doppler profile is the signal read in direction from the photodiode. After locking, the offset of the signal can be used to check whether the frequency is locked on the right position. The saturation absorption is the signal after the mixer.

C. Cavity locking servo circuit diagram

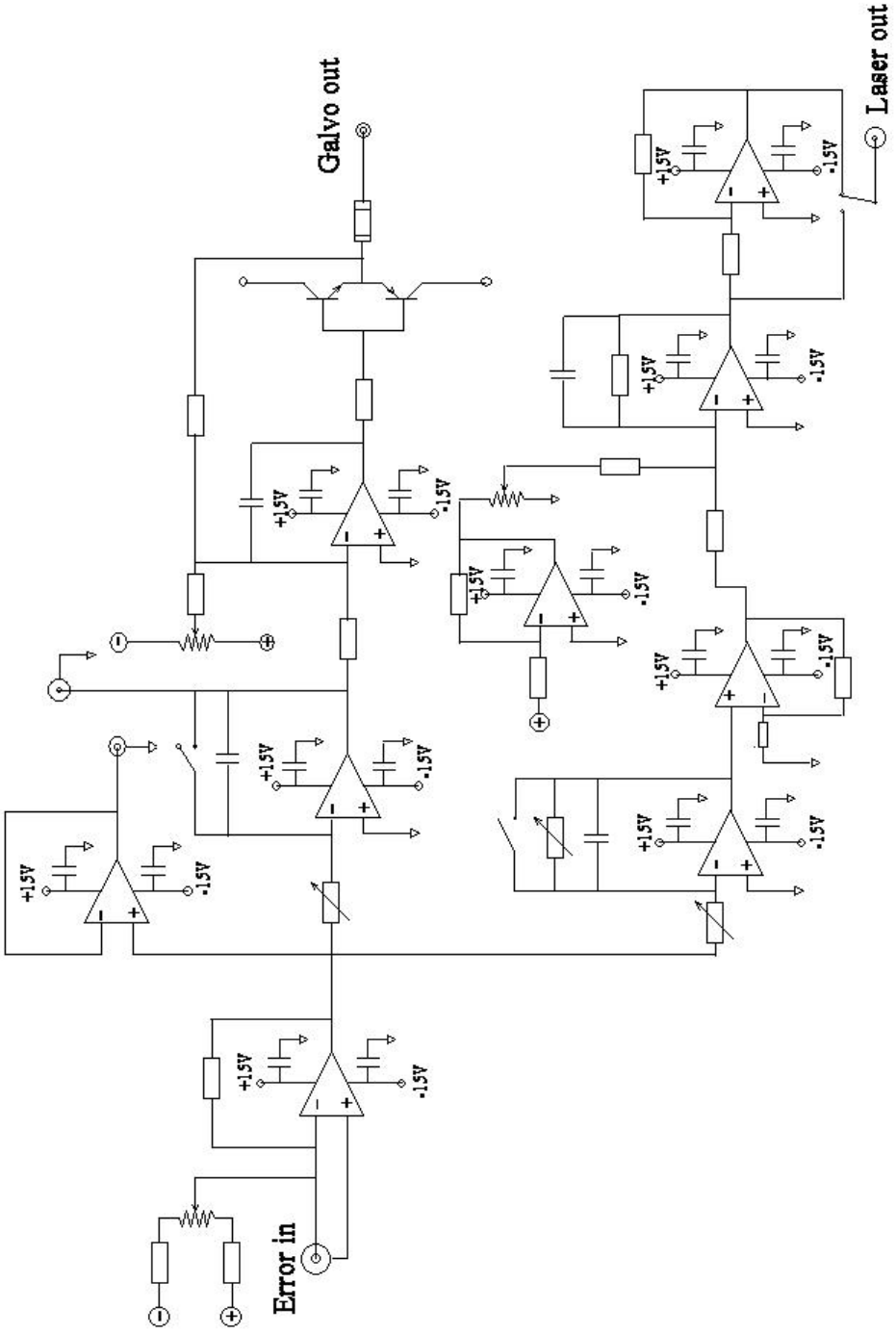

Fig. C. Cavity lock box diagram

D. Photodiode array

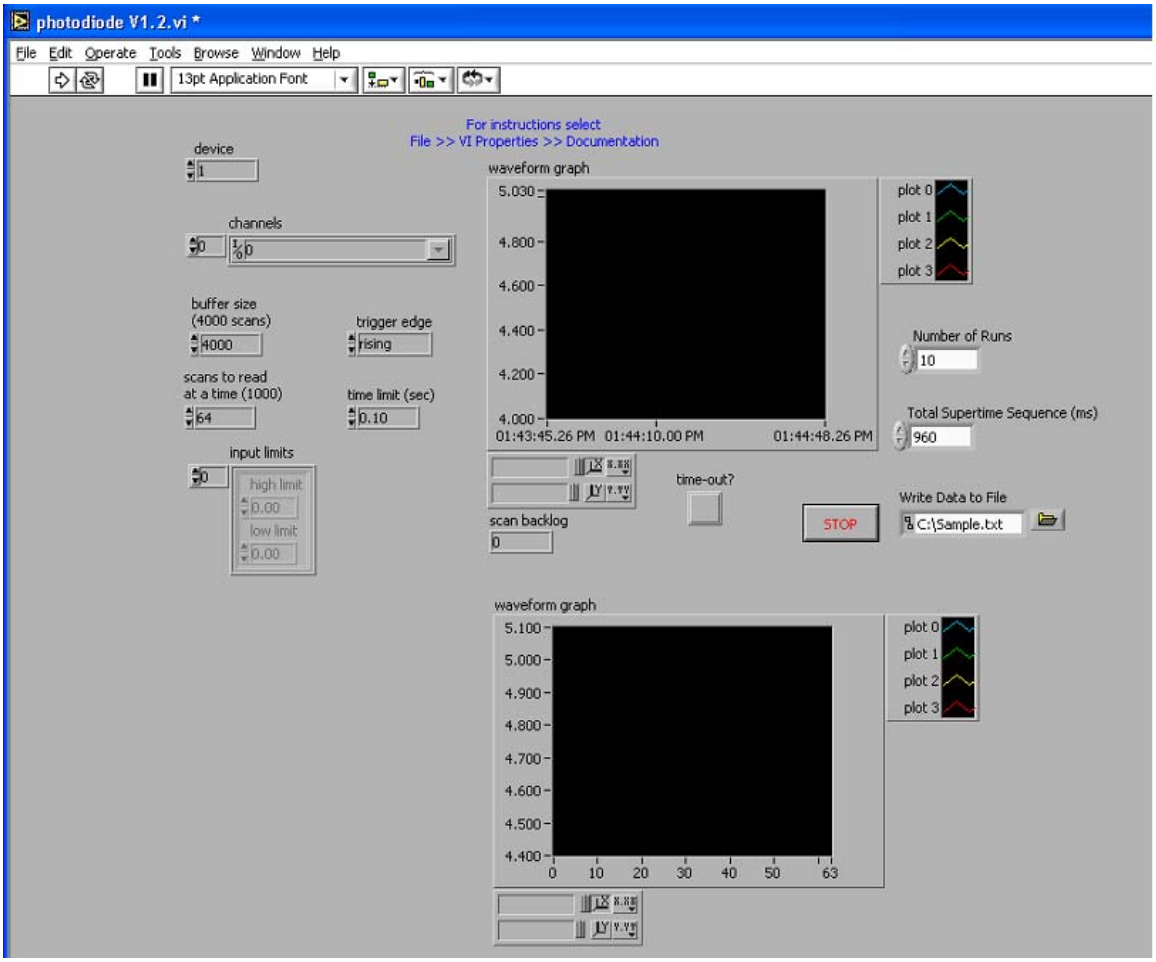

Figure D1. The front panel of program to read in the data from the photodiode array.

The card to read in the photodiode array data is PCI 6071. The photodiode array has 64 pixels. The scan to read at a time is set to 64. The number of runs can be set to any number larger than 1 (The first scan is always missed). The total suppertime sequence should set a number close to the real timing period from the timing board. The program repeated to read to be triggered to read in data with period set by this number.

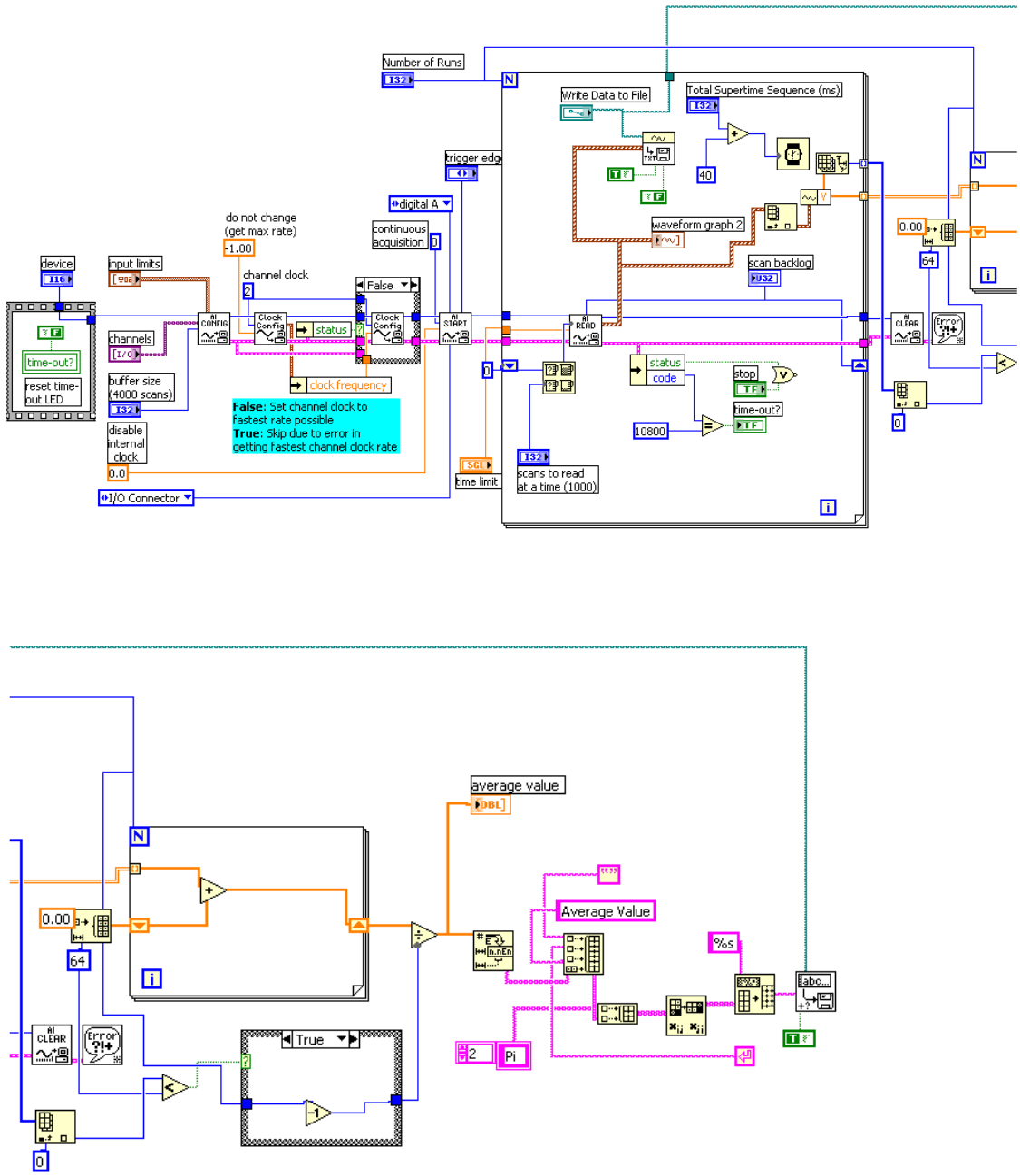

This is the diagram for the main vi. All of the extra stuff to the right of the big for loop averages all of the runs and appends the result to the text file. This was made with 64 pixels in mind, but can be easily changed for any number of pixels. Just replace the number 64 above with the correct number of pixels. For the string array constant above, just change it to the right number of pixels (or make a more efficient array). Do the same in the Export Waveforms to Spreadsheat File New(1D).vi

Figure D2. Photodiode array data acquisition program

Sequence might be missed if the time set is far off the real sequence total time and the number of runs is set a large number. The top waveform graph shows the real time data from the photodiode array. The bottom one shows the average data for the (n-1) runs.

The photodiode signal is calibrated by launching atoms up and stopping them at different time from 285 ms to 315 ms. At this time difference, atoms will spread out in the vertical direction differently which will make the signal size different by 10%. The most important intensity difference is due to the imaging system. The image size is 5 cm, And the lens we are using is a pair of plane convex lens with the focus length is 60 mm. The imaging numerical aperture is very large and induces large imaging distortion. Figure D3 shows the RMS spot size for this imaging system by the software Oslo. When the image point spread spot size on the axial is the minimum, at the full height the size is about 7 times larger. Trade off the on axial image quality will improve the overall imaging as shown in figure D3. The object to lens is 70 mm, lens to image is 51 mm, and the aperture to 12 mm.

The atoms' signals were recorded by the photodiode array. At about 298 ms after launch, atoms reach the center of the photodiode array, the signal is the largest. Before and after this time, the signal becomes smaller and smaller while actual signal size did not change much as shown in figure D4a (The dark signal is 5 volts). The peak signal size at different position on the photodiode array is shown in b and the calibration factor for this imaging system is gotten by setting the peak is same at different position.

E. Lens design

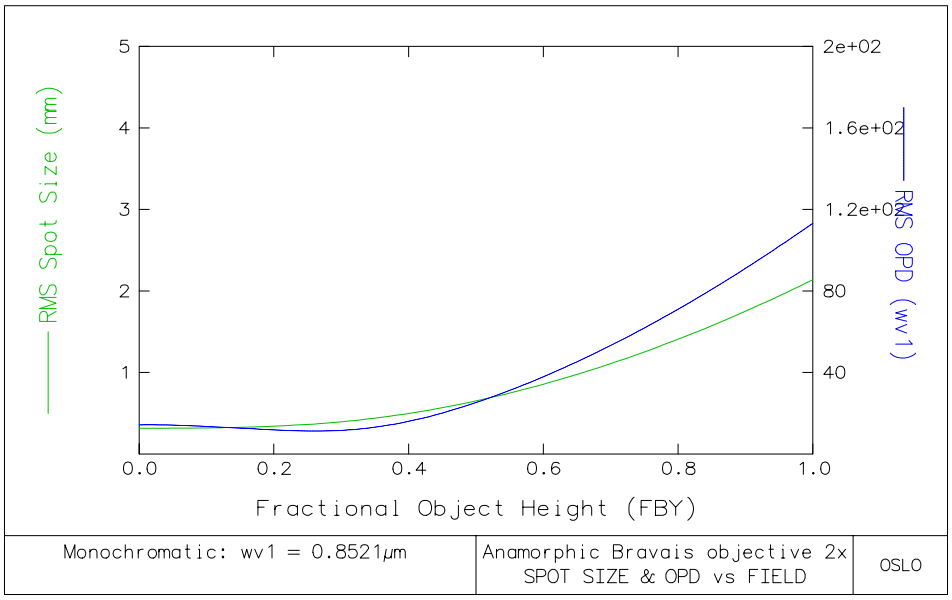

(a)

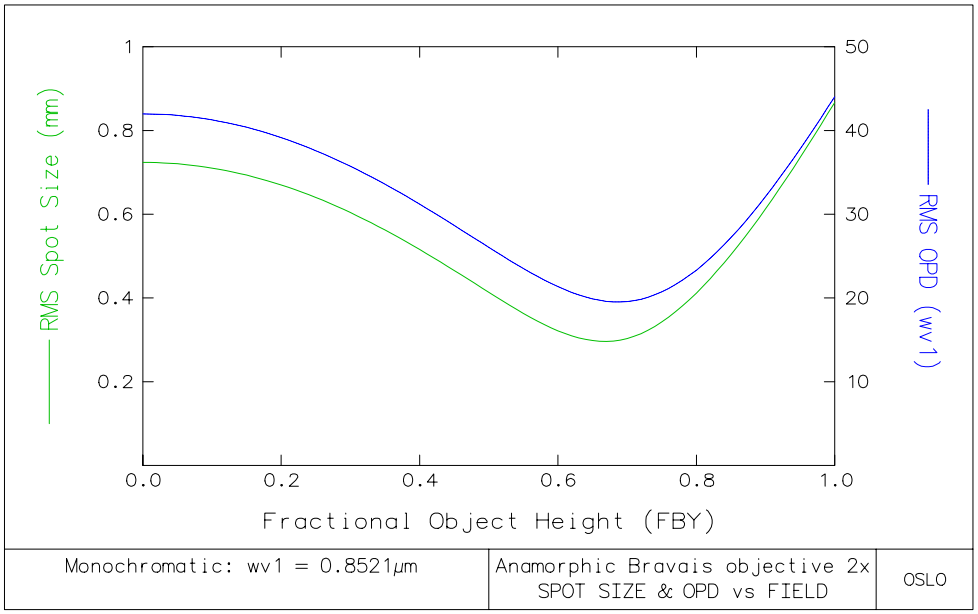

(b)

Figure D3. The RMS spot size gotten by Oslo software at different object height.

(a) Optimized on axis. (b) Optimized overall field of view

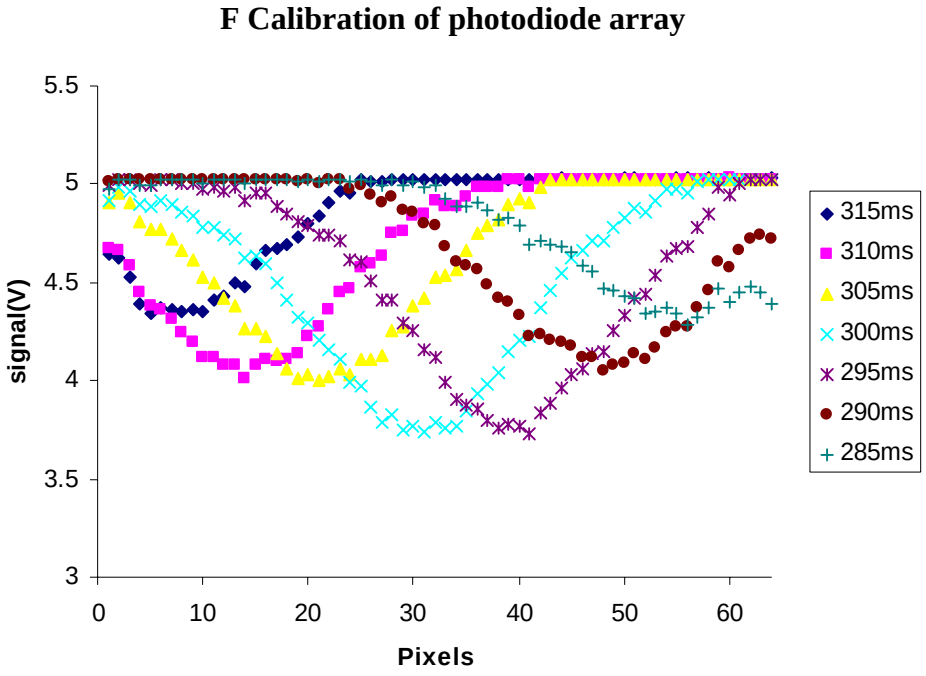
F Calibration of photodiode array
signal(V)
Pixels
315ms
310ms
305ms
300ms
295ms
290ms
285ms

(a)

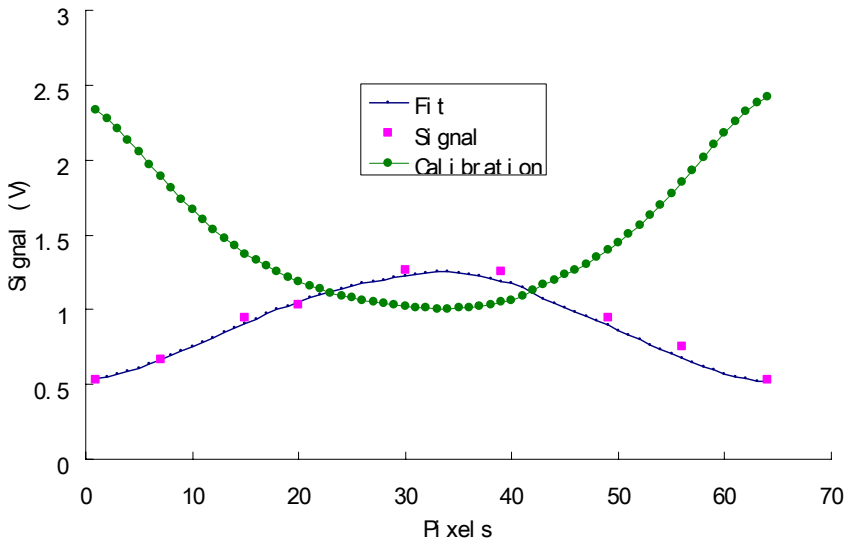
Fit
Signal
Calibration
Signal (V)
Pixels

(b)

Figure D4. Calibration of the photodiode array imaging system. (a) Atoms signal with different launch time, (b) Atom's peak signal size and calibration at different position.

Table D1: Calibration factors of the photodiode array at different pixels.

1	2	3	4	5	6	7	8
2.133457	2.275836	2.206708	2.130703	2.050882	1.969767	1.889329	1.811036
9	10	11	12	13	14	15	16
1.735922	1.664669	1.597684	1.535165	1.47716	1.423611	1.374391	1.329328
17	18	19	20	21	22	23	24
1.288226	1.25088	1.217082	1.186634	1.159346	1.135042	1.113563	1.094766
25	26	27	28	29	30	31	32
1.078522	1.064721	1.053268	1.044085	1.028807	1.020408	1.01626	1.008065
33	34	35	36	37	38	39	40
1	1	1.008065	1.01626	1.020408	1.033058	1.05042	1.06383
41	42	43	44	45	46	47	48
1.086957	1.126126	1.162791	1.200108	1.232142	1.267645	1.306828	1.349908
49	50	51	52	53	54	55	56
1.3971	1.448604	1.504591	1.565183	1.630418	1.700216	1.774324	1.852256
57	58	59	60	61	62	63	64
1.933217	2.016022	2.09901	2.179979	2.256144	2.324177	2.380324	2.420657

G. Photodiode array circuit

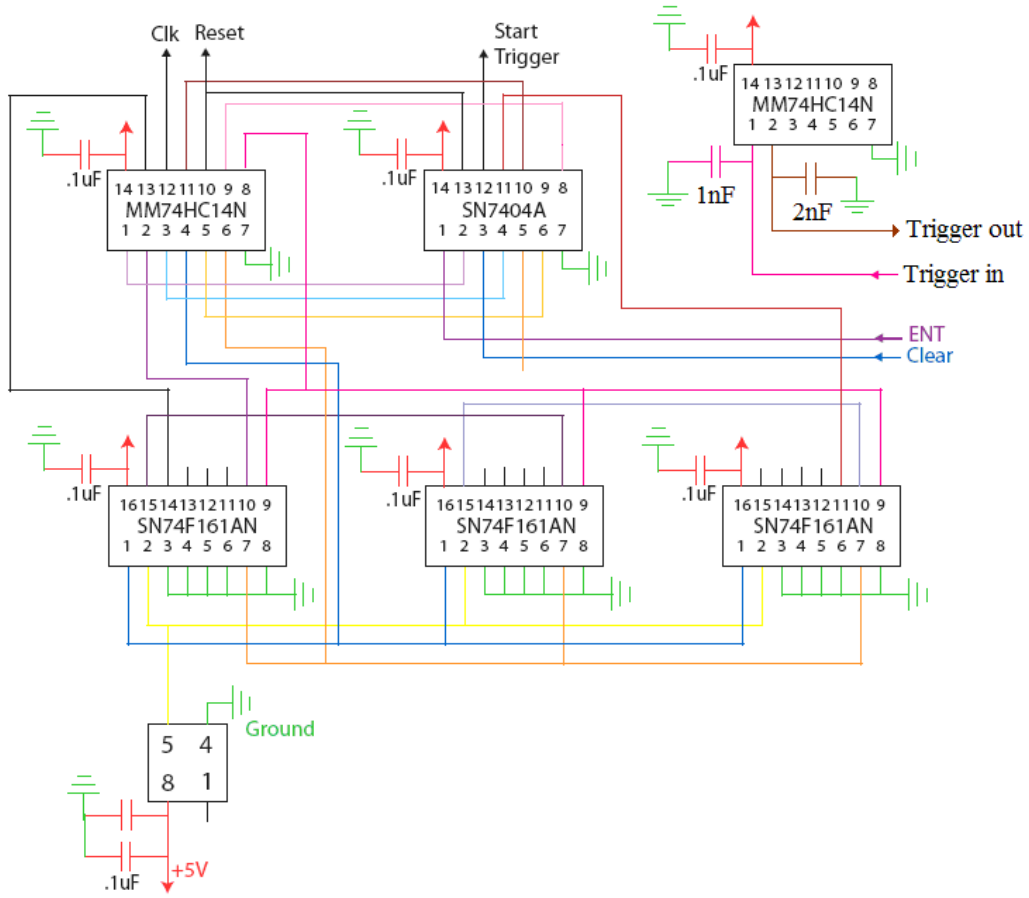

Figure D5. Photodiode array pulse control circuit diagram

Capacitor at the trigger in moves trigger signal relative to the video signal, Capacitor at the trigger out smooth the edge and reduce the ripple, but it is not totally get rid of. The oscillator generates square wave at rate of 1 MHz and is sent to the counter. The CLK signal and reset signal periods are twice and 2048 times of the clock signal

respectively. ENT and clear signal come from computer timing board control the CLK and reset starting time.

H. Timing board circuit diagram

The output of the 6534 board must be spliced together to create the actual timing signal that updates the analog output boards. This is done by a homemade digital circuit box located beside the timing computer and voltage output lines.

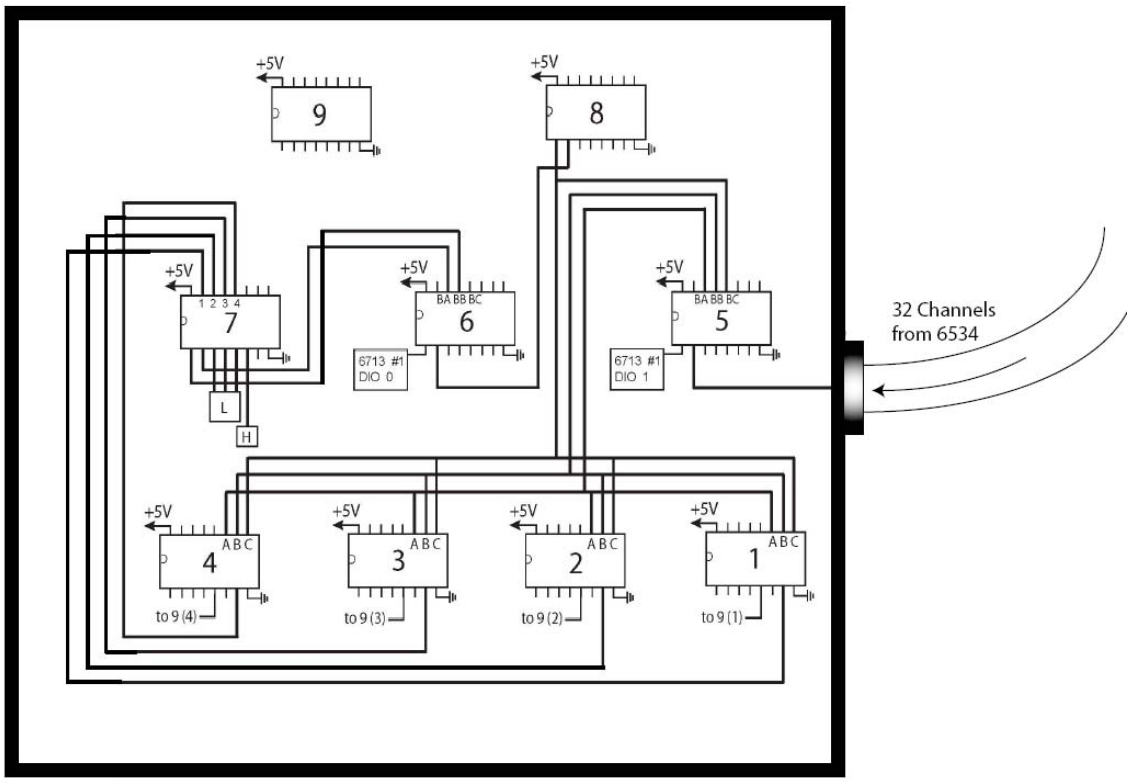

Figure E1. Timing board circuit diagram

The supertimev3.1 vi's data is outputted via seven national instruments boards. One PCI 6534 generates the timing signal which in turn updates the analog output boards. The other PCI 6534 card is used as digital analog output card. Five PCI – 6713 cards are used as analog output boards. These boards are 12 bit digital to analog converters with an output voltage range of -12V to +12V giving an output voltage resolution of about 5mV. They each have eight analog output channels.

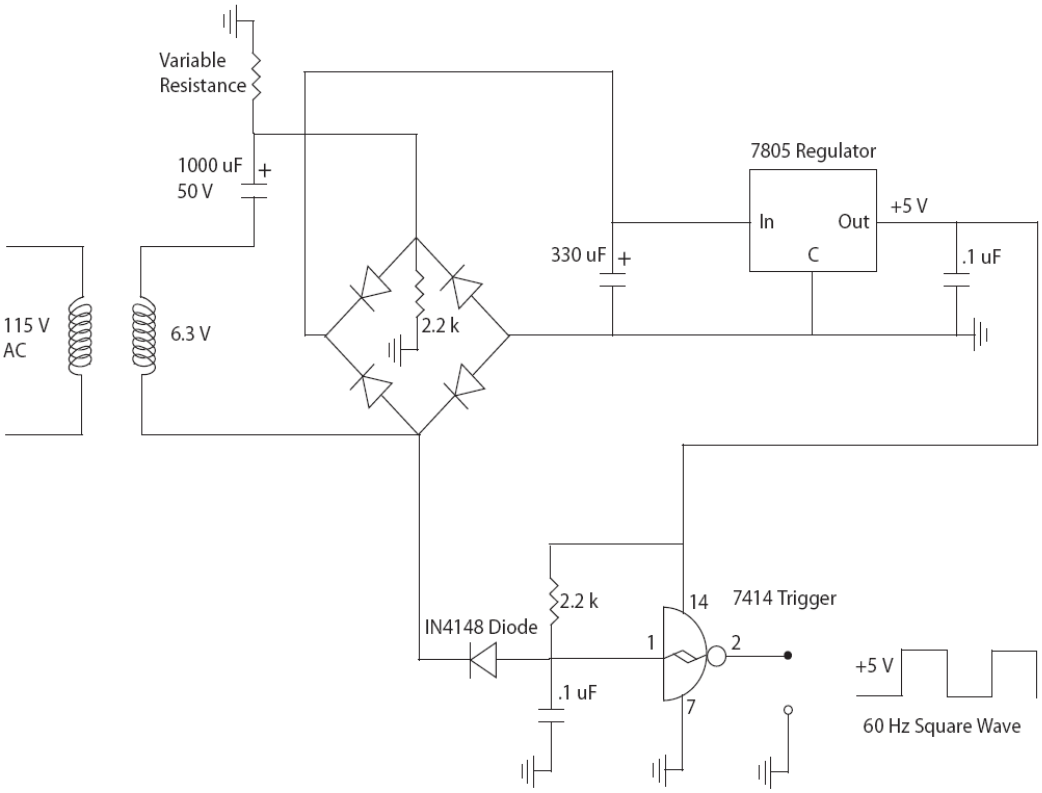

Figure E2. AC line trigger diagram for the timing board.

I. Power supply circuit for the coils inside the magnetic shielding

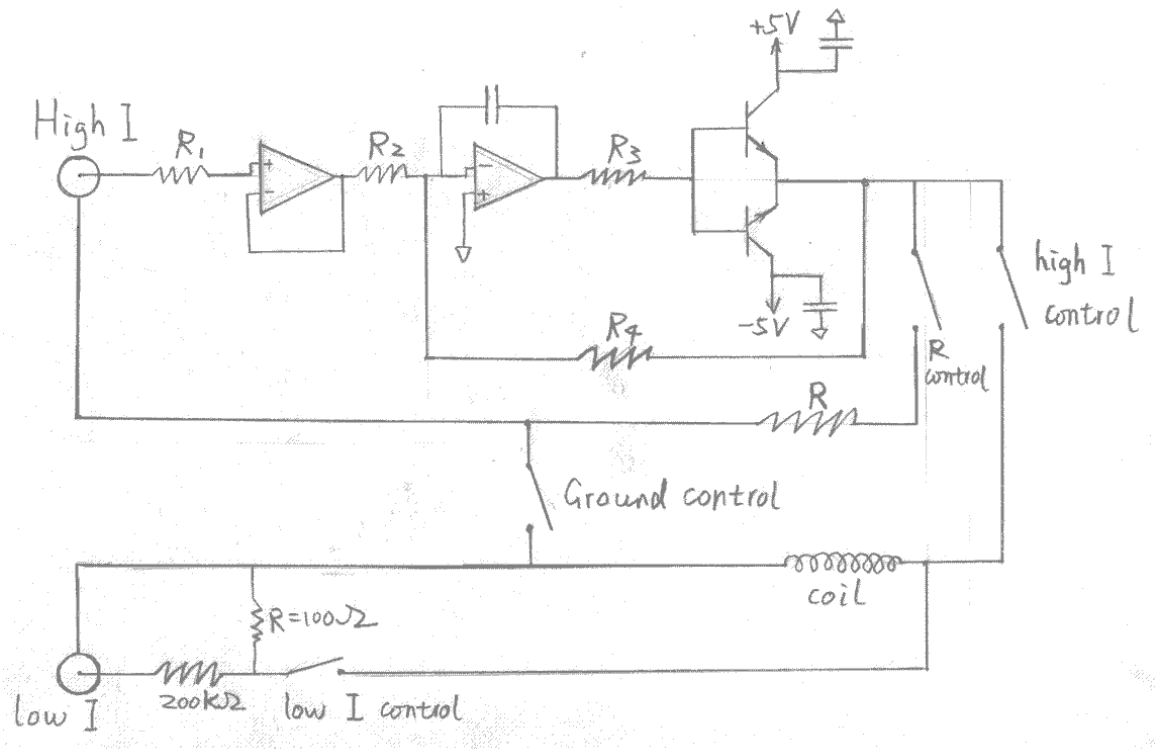

Figure F1. Power supply circuit for the coils inside the magnetic shielding.

The coils inside magnetic shielding will provide magnetic field for about a few mGauss during the optical pumping to provide the quantization axis which need high current power supply. During the coherent time, these coils provide the scan and bias magnetic field which only require very low and stable magnetic field, and require different power supply. The two power supply system are separated.

J. Total number of atoms in 1D lattices

a. Gaussian shape atoms density

Atoms peak density is n_0, total number is N, Gaussian shape in all directions, w_0 is the $1/e^2$ radius in the radial direction, w_y is the $1/e^2$ radius in y direction.

$$N = \iiint n_0 e^{-\frac{2l^2}{w_y^2}} e^{-\frac{2r^2}{w_0^2}} r dr d\vartheta dl = n_0 \left(\frac{\pi}{2}\right)^{\frac{3}{2}} w_0^2 w_y$$

If in y direction, the density is uniform and the length is l_y (Multiple loading). The total number is:

$$N = n_0 \frac{\pi w_0^2}{2} l_y$$

VITA

Fang Fang was born in Tianjin, China. She entered Nankai University in 1989 to study in the physics department and graduated with a Master of Science degree in Physics from Nankai University in July 1996 and became a professor in Nankai university after that. She began her graduate study at the Penn State University in August 2001.